

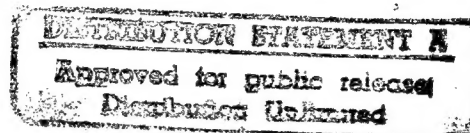
JPRS-JST-90-025

14 MAY 1990



**FOREIGN  
BROADCAST  
INFORMATION  
SERVICE**

# ***JPRS Report***



# **Science & Technology**

***Japan***

**19980130 059**

TRDI TECHNICAL REPORTS

REPRODUCED BY  
U.S. DEPARTMENT OF COMMERCE  
NATIONAL TECHNICAL INFORMATION SERVICE  
SPRINGFIELD, VA. 22161

[DTIC QUALITY INSPECTED 3]

JPRS-JST-90-025  
14 MAY 1990

SCIENCE & TECHNOLOGY  
JAPAN

TRDI TECHNICAL REPORTS

906C3824 Tokyo BOEICHO GIJUTSU KENKYUHONBU GIHO in Japanese Jun, Jul 89

[Selected Japan Defense Agency Technical Research & Development Institute)  
(TRDI) Technical Reports published in June and July 1989]

CONTENTS

Characteristics of Double-Base Rocket Propellants [Jun'ichi Kimura, Akira Yamazaki].....	1
Performance of Argon-Xenon Laser [Takao Komi, Masakatsu Sugii, et al.].....	19
Burn Rate of Rocket Motors Reduced [Kousei Miyata, Naminosuke Kubota].....	26
Transonic Wind Tunnel Test To Evaluate Wing Flutter [Yukio Yoshitake, Etsuroh Sentoh, et al.].....	42
Research on Lithium-Thionyl Chloride Batteries [Masaaki Maekawa, Kaoru Sohkura, et al.].....	56
Characteristics of New Lens Antenna [Osamu Hoshimoto, Masanori Shinriki, et al.].....	74
Two-Pulse Technique for New Rocket Motor [Kouichi Fukuda, Chikahiro Iwasaki, et al.].....	84

## Characteristics of Double-Base Rocket Propellants

906C3824A Tokyo BOEICHO GIJUTSU KENKYUHONBU GIHO (Japan Defense Agency Technical Research & Development Institute) in Japanese Jun 89 Technical Reports, No 5529 pp 1-14

[Article by Jun'ichi Kimura, assistant director general of the Third Research Laboratory of the Second Prime Mover Department of TDRI's Third Research Center, and Akira Yamazaki, assistant director general of the Second Research Laboratory of the Second Prime Mover Department of TDRI's Third Research Center: "Application of Thermal Analysis to the Evaluation of LOVA Characteristics of Propellants"]

### [Text] Summary

The aim of this study is to examine the applicability of thermal analysis to characterize ignitability of rocket propellants and their ingredients. Double-base propellants, consisting mainly of nitrocellulose (NC) and nitroglycerine (NG), were used as a sample because there is no general agreement in reported thermograms of double-base propellants by others. We have revealed the occurrence of two distinctively different ignitions triggered by exothermic decomposition of NC and NG: as heating rate was increased, transition occurs from NC-triggered ignition to NG-triggered ignition. We have also demonstrated that both heating rate and sample weight predominate the onset of ignition; at a constant sample weight, ignition occurs at a higher temperature as heating rate is raised along with the NG or NC decomposition peaks; at a constant heating rate, transition occurs from NC-triggered ignition to NG-triggered ignition as sample weight is added. We also confirmed that the ignition of the double-base propellants originates in the condensed-phase under the experimental conditions tested. The thermonanalytical method has been proven to be a promising diagnostic technique to characterize heat-resistant properties of propellants and explosives by virtue of simplicity of data acquisition and analysis.

### 1. Introduction

The importance of creating rocket propellants and explosives that are not sensitive to heat and impact has been a common subject in the field of guided weapons, firearms, and ammunition. The double-base propellant (main

components: nitrocellulose and nitroglycerine) is commonly used as a smokeless rocket propellant or as a gun propellant powder, and it appears that the performance of the double-base propellant can be enhanced without degrading its characteristic smokelessness. Therefore, in order to improve the heat resistance of this kind of propellant, i.e., to develop low vulnerability (LOVA) propellants, it is absolutely necessary to obtain basic data on the ignition characteristics and behavior of double-base propellants when subjected to heat.

The purpose of this research work was to use a thermal analyzer to evaluate the ignition characteristics and to clarify the relationship between the ignition characteristics and the exothermic physicochemical characteristics that accompany thermal decomposition. Also, this thermal analyzer is used to measure changes in the mass of the samples and the input and output of heat caused by raising the temperature of these samples at a constant heating rate. Thermal analyzer has been applied to the evaluation of the safety of hazardous materials, and there are some research reports on this application, but there is no example of a study where ignition characteristics have been subjected to a quantitative evaluation. We have studied the possibility of using a thermal analyzer to clarify ignition mechanisms and to evaluate ignition characteristics, thereby taking advantage of the fact that it is easy for a thermal analyzer to change variables that affect ignition, such as ambient gas, pressure, etc., in sample rooms.

Many researchers have long been engaged in research on the thermal decomposition characteristics of the primary components of double-base propellants; nevertheless, they continue to disagree with each other on some important points.<sup>1</sup> In our research laboratory, we have carried out research on double-base propellants and the thermal decomposition speed and decomposition mechanism of nitrates, which are the principal components of these double-base propellants. Our goal has been to resolve a number of unsolved problems. We have determined that an autocatalyzed reaction is generated at a rate-determining step of thermal decomposition in comparatively high temperature regions and that this autocatalyzed reaction is an oxidative reaction produced by the nitric oxide generated by thermal decomposition.<sup>2,3</sup> This report describes the results of our efforts to develop simple methods for evaluating the thermal ignition characteristics necessary for improving LOVA characteristics against heat in light of the results of the basic research work that has been carried out up to now.

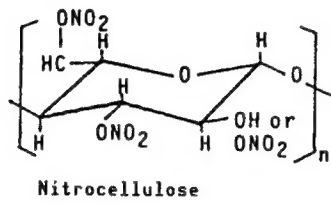
## 2. Experiment

### 2.1 Sample

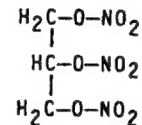
Three kinds of double-base propellants were used in this experiment; the ratio of their main components, i.e., nitrocellulose (NC) to nitroglycerine (NG) range from about 1.4:1~5:1. The samples were formed into cylinders with a diameter of 1 mm and a height of 1 mm. Table 1 shows the composition of the samples. These samples are all so-called, "Non-Plateau Double-Base Propellant," which means they do not contain any combustion catalysts such as lead salt, etc.

Table 1. Composition of Propellant Samples

Components	Propellant 1	Propellant 2	Propellant 3
Nitrocellulose (NC)	51.8	71.2	79.3
Nitroglycerin (NG)	36.5	24.1	16.0
DEP (Diethyl phthalate)	9.6	2.4	2.4
2-NDPA (2-nitro diphenyl amine)	2.1	2.1	2.1
NC/NG	1.4	3.0	5.0



Nitrocellulose



Nitroglycerin

## 2.2 Devices

A differential scanning calorimeter (DSC-20B) and a thermal balance (TGA-20B) with an analog differentiator were used as thermal analyzers. A sample was put in an aluminum sample-receiving dish with a diameter of 5.8 mm and a height of 1.8 mm in a releasing state, and the influence was investigated while changing the weight of the sample across a range of about 0.2-10 mg. The thermal balance is of the vertical hanging type and is structured so that a sample receiving dish is put under a platinum hanging wire. Temperatures were calibrated by measuring the magnetic transition point (Curie point: 353°C) of nickel.

Figure 1 shows the structure and principle of operation of the thermal balance (TGA-20B) and of the differential scanning calorimeter (DSC-20B). Both devices are DT-20 series devices made by Shimadzu Corp. and are so-called "Micro-Thermal Analyzers."<sup>4</sup> They can be used to measure the weight of samples as small as several milligrams. A preliminary test was conducted by using a mixture of nitrogen and air as the atmosphere for the measurement. As a result, it was ascertained that the thermal ignition of double-base propellants is not affected by any partial pressure of oxygen (Figure 14). Accordingly, the measurement was carried out in untreated air without any use of inactive gas.

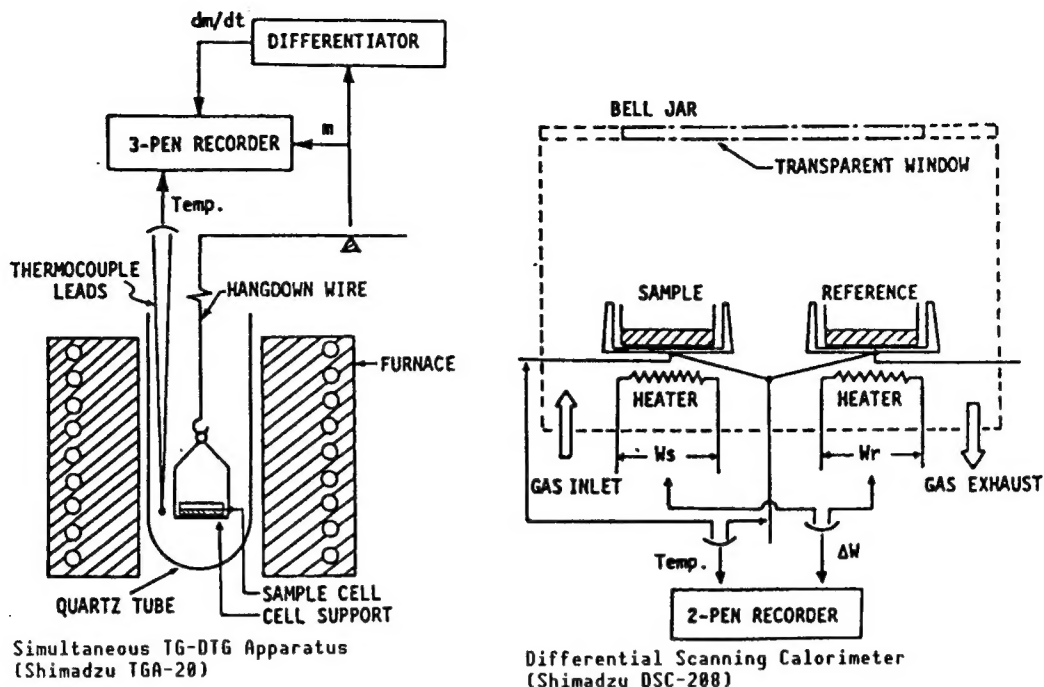


Figure 1. Block Diagrams of DSC and TG-DTG<sup>4</sup> Used in This Research

### 3. Result and Discussion

#### 3.1 Relationship Between Thermal Decomposition Characteristics and Thermal Firing Properties

There have been many reports on thermal analyses of double-base propellants. However, the decomposition peaks of NG and NC, which are the principal components of double-base propellants, have not been separated from each other by thermal measurement using differential thermal analysis (DTA) or a differential scanning calorimeter (DSC), nor have they undergone weight reducing measurement based on thermal weight analysis (TG).<sup>5-8</sup> It is believed that this is due to the following factors: 1) both thermal decomposition temperatures are very close to each other; 2) both thermal decomposition speed characteristics are similar to each other; and 3) the decomposition peaks cannot be separated because the thermal analyzer does not have sufficient thermal response. However, it is difficult to believe that the third factor is the principal problem, because the two peaks cannot be separated from each other even by the DSC, which has a very high thermal response. Another possible cause is that there exists a number of small approaching exothermic peaks that are hidden because another heating value is large.

In this research work, then, a weight loss speed curve was found by using a highly sensitive Kern-type (vertical system) thermo-balance. This was compared with a heat generation speed curve determined by using the DSC. In addition, as shown in Table 1, samples with NC/NG ratios of about 3:1 and 5:1, as well as a standard propellant with a ratio of almost 1:1 were used to ensure the separation. As a result, in a typical example, as shown in Figure 2, it was

possible to clearly distinguish two peaks by a differential thermal weight analysis (DTG) curve. Reproducibility is low, but an exothermic shoulder may be recognized at the low temperature side in the DSC curve.

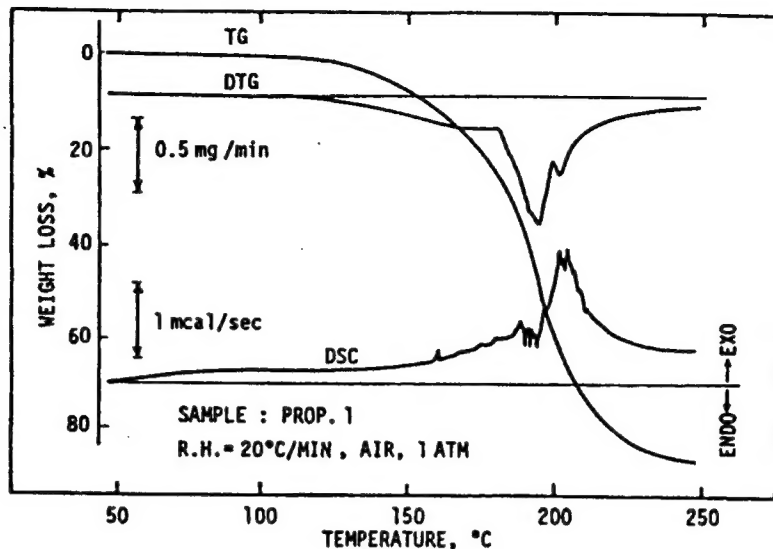


Figure 2. Result of Thermochemical Analysis of Double-Base Propellant (TG-DTG: DSC)

Further, because samples with different NC/NG ratios were used, it was possible to identify the first peak and the second peak. That is, it has been determined that the first peak is due to the decomposition of NG while the second peak is due to that of NC. This is because the height of the first peak is inversely proportional to the NC/NG ratio (Figure 3).

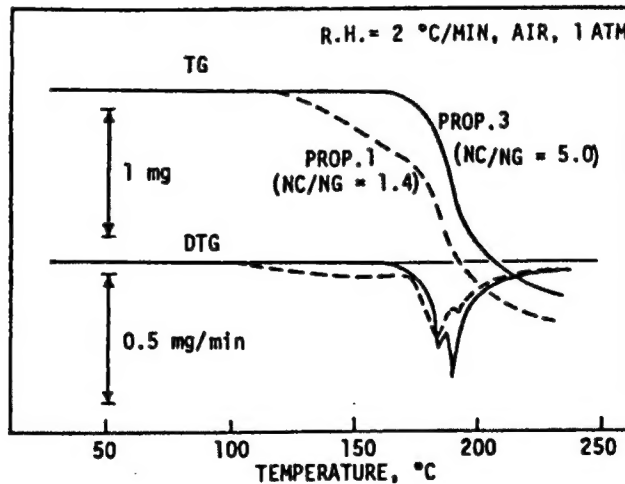


Figure 3. Comparison of TG-DTG Curves for Double-Base Propellants With Different NC/NG Ratios

This figure shows that the first peak (low temperature side) and the second peak are caused by the thermal decomposition of NG and of NC, respectively.

The relationship between a propellant's thermal decomposition characteristics and its thermal ignition properties was clarified by changing the weight of the samples and the rate at which they were heated. It is possible to clearly distinguish the occurrence of ignition, because the weight apparently increases momentarily at the time of ignition, i.e., this increase appears as an upward spike on the DTG. As shown in Figure 4, ignition is generated qualitatively in the vicinity of temperature close to the two thermal decomposition peaks, and when the weight increases at a constant heating rate, the ignition will transit from the first peak to the second peak. This transition phenomenon was not previously known.

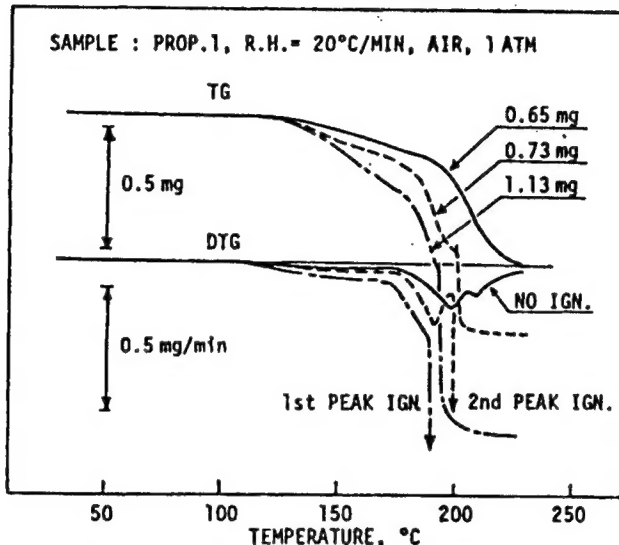


Figure 4. TG-DTG Curve for Double-Base Propellant  
When the Weight of the Samples Is Changed

Figure 5 shows the correlation between the rate of weight reduction at firing time and ignition temperature for three kinds of samples. The ignition temperature does not depend on the NC/NG ratio, but the rate of weight reduction at the time of ignition greatly depends on the NC/NG ratio. It was learned that the ignition transited at a weight reducing rate equivalent to the sum of the plasticizer (DEP) and the NG, which is an almost liquid component, present in the propellant.

In this way, when the number of samples was small at a constant heating rate, only decomposition occurred, while thermal ignition at the second stage was separated and measured together with increase in the weight of the samples. It seems that this can be explained by a fortuitous set of experimental conditions. Next, we will discuss the conditions necessary for two-stage ignition and the influence of heating rate on thermal ignition.

The weight of typical double-base propellants (characterized by propellant 1) as samples is selected properly under atmospheric pressure. Figure 6 shows the result of the selection. As shown in this figure, thermal decomposition is represented by two straight lines such that when the logarithm of the heating rate is taken on the x-axis and the reciprocal number of the decomposition

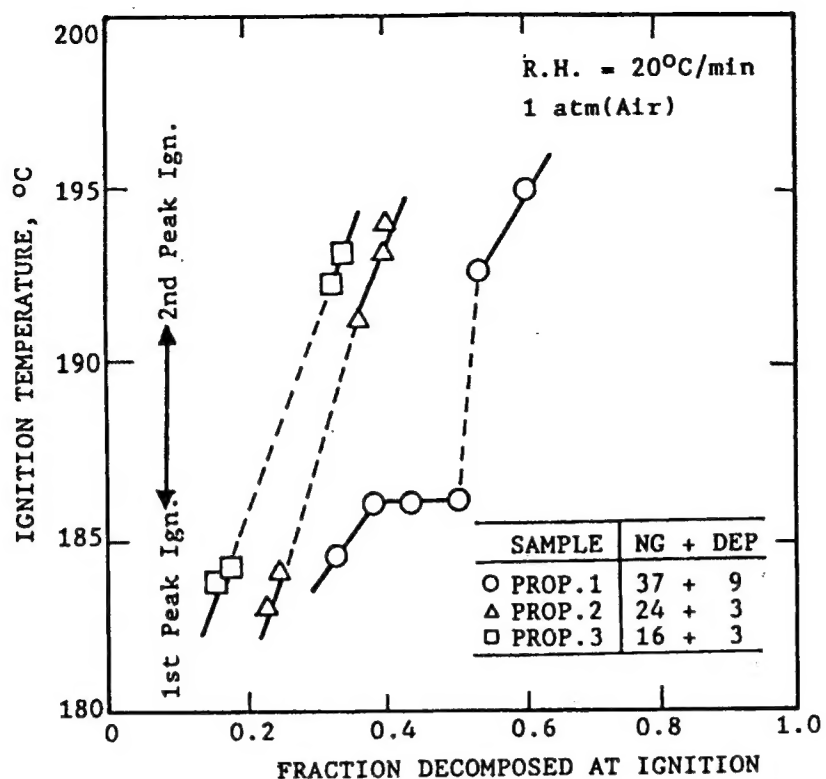


Figure 5. Influence of NC/NG Ratio on Second-Stage Ignition

This figure shows that the first ignition peak is generated at a value close to the total sum of the content of NG and DEP, and is caused by the exothermic decomposition of NG.

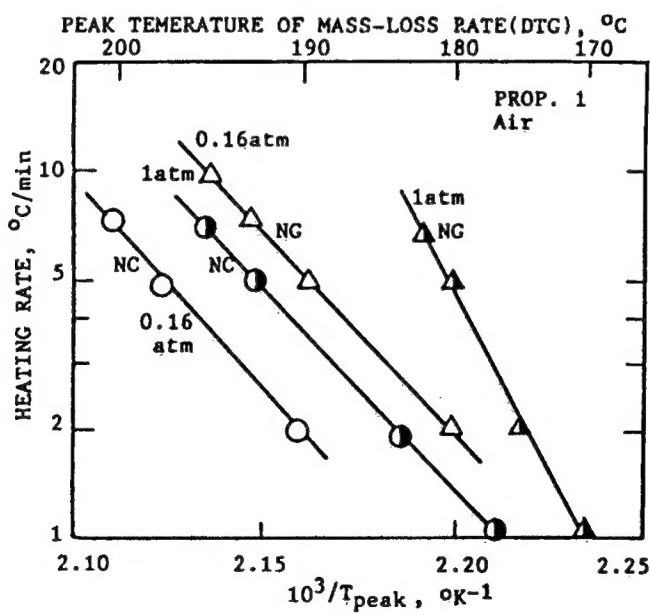


Figure 6. Characteristics of Thermal Decomposition Ratios for NC and NG, the Primary Components of Double-Base Propellants, and Influence of Pressure on NC and NG

peak temperature is taken on the transverse axis, the gradients (activation energy) of the two straight lines will differ from each other.<sup>9</sup> The straight line on the low temperature side is due to the thermal decomposition of NG, and the apparent activation energy is abnormally high, reaching about 60 Kcal/mol. Meanwhile, the straight line at the high temperature side is due to the thermal decomposition of NC, and the activation energy is about 47 Kcal/mol. Variations can be seen in ignition temperatures, but thermal ignition is arranged on a straight line that almost equals thermal decomposition and transits from the second peak ignition (NC firing) to the first peak ignition (NC firing) in accordance with an increase in the heating rate (Figure 7).

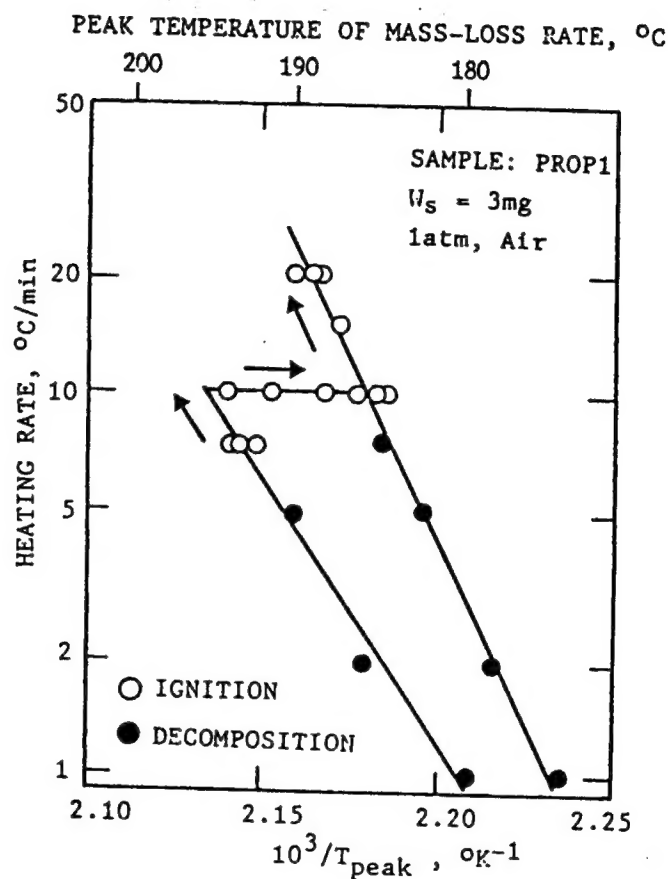


Figure 7. Relation Between Thermal Decomposition Characteristics and Transition Phenomena of the Second Stage Ignition of Double-Base Propellant

Many values for the activation energies of the thermal decomposition of double-base propellants have been reported. These can be broadly classified into two values, i.e., about 35 Kcal/mol and about 45-50 Kcal/mol. It has been considered up to now that the former value is due to an autocatalyzed reaction while the latter value is due to homolysis.<sup>1</sup> In our research laboratory, however, we recently reached a conclusion quite the reverse of the conventionally established theory. This is based on the results of our

research on the thermal decomposition of double-base propellants at comparatively low temperatures (150°C or less), and we have reported on this conclusion. In other words, a logical analysis of the reaction rate has demonstrated that a value of about 35 Kcal/mol is due to the homolysis of the combination of N-O, while the activation energy close to 50 Kcal/mol is due to the autocatalyzed reaction.<sup>2,3</sup> It was also anticipated that the main reaction (rate-determining step) in high temperature regions would be autocatalyzed reaction with high activation energies. As shown in Figure 7, a value of 47 Kcal/mol is the activation energy for the thermal decomposition of NC contained in a double-base propellant in air at 1 atmosphere of pressure. This value is consistent with the expected value.

Meanwhile, the value of the activation energy for the decomposition of NG at 1 atmosphere of pressure was abnormally high, reaching about 60 Kcal/mol. As shown in Figure 6, that of NG at low pressure (0.16 atmosphere) was as low as 46 Kcal/mol. Likewise, in the same way as at 1 atmosphere, that of NC was 47 Kcal/mol. It was unknown before now that the activation energy for the thermal decomposition of nitrate is dependent on pressure to such an extent. It is not clear why only the NG contained in double-base propellants is affected by pressure. This must be determined by future research.

The introduction to this section indicates that there has been no reporting up to now on the fact that the thermal analyzer curve of double-base propellants was divided into two peaks. It was believed that this was because one heating value was larger than the other and concealed the second. In order to confirm this hypothesis, the heating values of NG and NC were determined based on a comparison of the weight reducing speed (DSC) curves obtained from this research work on the assumption that the heating value is a proportional constant of the heat generation speed and weight reducing speed. That is, as shown in equation (1), the heating value ( $\Delta H_r$ ) at an arbitrary temperature is a proportional constant of the height of the DSC curve and that of the DTG curve.

$$\Delta H_r = (\partial_q)_T / (\partial_w)_T = \frac{\text{Height of DSC curve (mcal/sec)}}{\text{Height of DTG curve (mg/sec)}} \quad (1)$$

The advantage of this equation (differential equation) is that the heating value can be found as a function of temperatures. Figure 8 shows examples of the results of the calculations and the DTG and DSC curves of a standard double-base propellants (propellant 1). The heating value of NG and NC were found to be about 50-60 and about 200 cal/g, while that of double-base propellants is about 70~80 cal/g.<sup>10</sup> These values are almost identical to those measured in this research work.

The measured value for the decomposition heating value of NC is equivalent to 20 percent of its explosive heating value (about 1,000 cal/g),<sup>11</sup> while that of NG is equivalent only to about 3 percent of its explosive heating value (1,500 cal/g).<sup>11</sup>

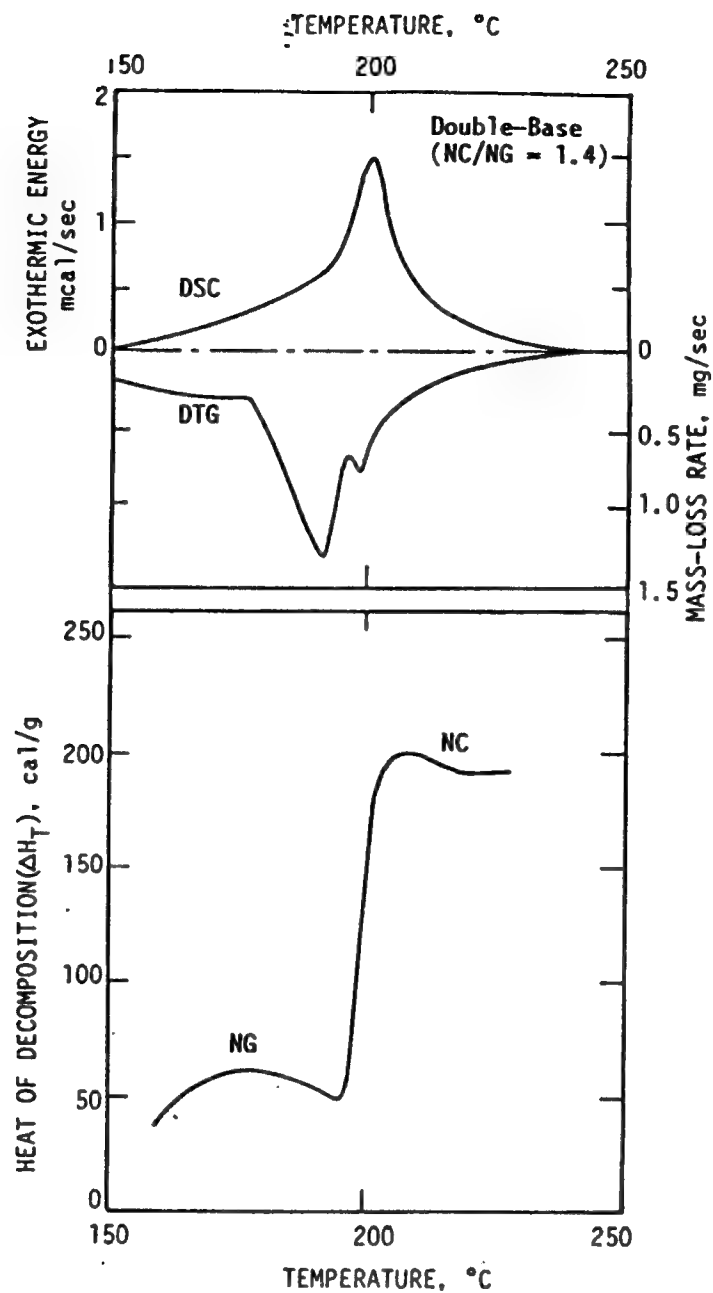


Figure 8. Thermal Dependence of Value of Heat Generated by Thermal Decomposition of Double-Base Propellant

The values of heat generated from NG to NC were measured to be 50~60 cal/g and about 200 cal/g, respectively.

The relationship between explosive heating value and heating value is not proportional. It is believed that this fact may provide some clues about the decomposition mechanism. The value obtained by measuring the decomposition heating value of NG includes errors, because an endothermic reaction is caused by evaporation at the same time as that of exothermic decomposition.

Therefore, it is necessary to pay attention to the fact that the measured value is lower than the actual value.

As a result of the study described in section 3.3, it was determined that the exothermic influence in gaseous phases can be ignored. Therefore, it can be considered that the values obtained by measuring these decomposition heating values are almost purely heating values in condensation phases.

We will now move on to discuss the difference between the heating value of NC and that of NG. The difference between the two chemical structures is as follows: the former is a high molecular compound with a repeating unit in a pyranose ring (grape sugar structure) where oxygen atoms are contained in six member rings, while the latter is a nitrate with a low molecular weight where glycerin, which is a trivalent alcohol, is nitrated.

In the case of NG, it is believed that aldehydes (for example, formaldehyde: HCHO) with a low molecular weight are produced and are separated readily from reaction systems following the release of nitrogen dioxide due to homolysis of the weakest bonding of oxygen and nitrogen. Therefore, it is felt that nitrogen dioxide is not a sufficient cause for any oxide reaction at low pressures, such as atmospheric pressure. We will quantitatively discuss this point in the next item and, as a conclusion, we have determined that oxidation due to  $\text{NO}_2$  cannot occur within the conditions of this experiment. On the other hand, in the case of NC, it is known that homolysis of nitrate group ( $-\text{O}-\text{NO}_2$ ) side chains, homolysis of the pyranose ring, and cleavage of the principal chain occur simultaneously and that complex metathetical reactions occur in the viscous condensation phases until the NC turns to a fragment with a molecular weight sufficient for evaporation.<sup>1</sup> Consequently, it can be said that oxidation is induced by  $\text{NO}_2$  and increases in the heating value. Actually, the results we obtained indicate that the thermal decomposition peak temperature of NC is about  $10^\circ\text{C}$  higher than that of NG (Figures 3 and 6). It has also been demonstrated that the thermal decomposition peak temperature of NC decreases along with a decrease in pressure. Thus, as shown in Figure 6, the thermal decomposition peak temperature of NC is about  $3\text{--}4^\circ\text{C}$  lower than the peak value at 0.16 atmosphere.

It was found in this research work that the double-base propellant can cause a two-stage ignition depending on the heating rate and the number of samples. According to one thermal ignition theory, this phenomenon can be explained as follows:

It is believed that when the pace of heat generation surpasses that of heat loss, thermal ignition will occur. Now, considering the temperature differences and the temperatures on the ordinate and transverse axes, respectively, as shown in Figure 9, in general, the rate of heat loss can be expressed by a straight line that passes through the origin. The inclination of this straight line is peculiar to thermal analyzers. In the case of double-base propellants, the rate of heat generation can be expressed with a curve that has two peaks (see the DSC curve shown in Figure 2). With respect to the conditions governing the occurrence of two-stage ignition, the following three cases can be considered depending on whether or not the straight line representing heat loss and the heat generating curve intersect.

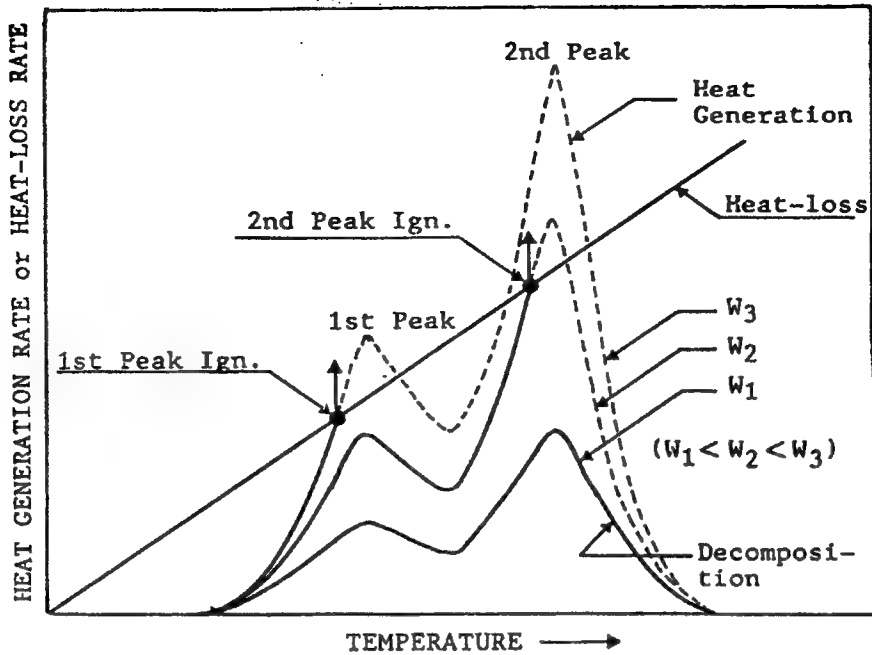


Figure 9. Characteristic Representation of How Conditions Governing Second Stage Ignition Are Explained by Theories of Thermal Ignition

As can be seen from this figure, second stage ignition occurs when the first peak (low temperature side) is lower than the second (high temperature side), and the ignition temperature transits from the second peak to the first one. The result predicted by this figure accords with the experimental results we obtained.

In the first case shown in Figure 9, thermal ignition does not occur, because the heat loss straight line is higher than the heat generation curve. In the second case shown in the figure, there is a possibility that thermal ignition could occur at temperatures higher than the temperature of the intersection point, because the heat loss straight line intersects the second peak of the heat generation curve. Finally, in the third case shown in the figure, there is a possibility that thermal ignition could occur in the vicinity of the first peak, because the heat loss straight line intersects the first peak.

Assuming that the former represents first peak ignition and the latter second peak ignition, the first and second peak ignitions are based on the exothermic decomposition of NG and NC, respectively. A comparison of cases 2 and 3 clearly indicates a condition for generating two-stage ignition. That is, the first exothermic peak on the low temperature side is lower than the second peak on the high temperature side.

### 3.2 Influence of Weight of Samples

The previous section outlined the influence of the weight of samples in the ignition characteristics of double-base propellants (Figure 4). This influence will now be studied in greater detail. Figure 10 shows the result of an investigation of the effect of the weight reducing rate at ignition by

changing the weight of sample 2 (NG content = about 24.1 percent) from about 2~8 mg. Second peak ignition was generated in a range of sample weights up to about 4 mg, while first peak ignition was generated at weights of about 4 mg or more. The weight loss is about 24 percent during a transition from second peak ignition to first peak ignition. This values accords with NG content. This experimental result has demonstrated that first peak ignition is caused by NG.

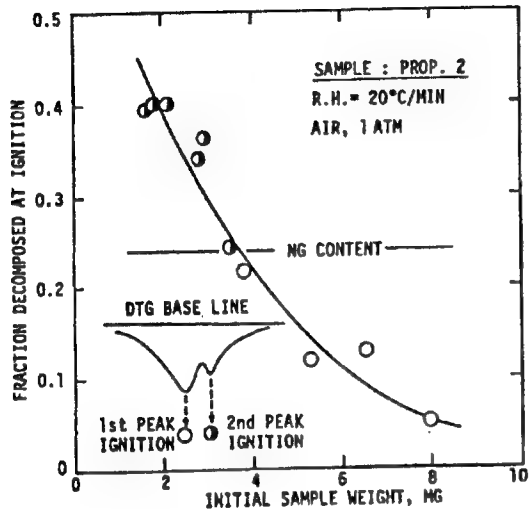


Figure 10. Influence of Sample Weights on Second-Stage Ignition (Constant heating rate)

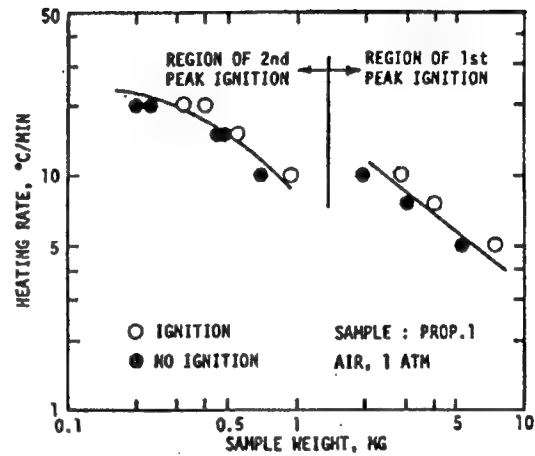


Figure 11. Influence of Weight of Samples and Heating Rate on Ignitability Limit

Figure 11 shows the result of plotting logarithms of the weights of samples and heating rate in order to clarify the extent of the influence of the weight of these samples and the heating rate on two-stage ignition. It shows that ignition-generating critical areas have an inclination of about minus one-half, that the weight of the samples and the heating rate affect ignition almost simultaneously, and that weight and heating rate are in inverse proportion to each other. In other words, when the thermal ignition characteristics of explosives are assessed by using a thermal analyzer, it is necessary to control the weight of the samples and the heating rate exactly.

### 3.3 Influence of Pressure and Oxygen

Earlier studies have shown that the thermal ignition of double-base propellants is caused by exothermic reactions of the main components in condensation phases. An experiment on the influence of pressure was conducted to verify that ignition is in fact generated during such condensation phases. This section will describe the design and results of this experiment.

In order to study the influence of pressure theoretically, it is necessary to understand the reaction mechanism for the thermal decomposition of nitrate. However, many aspects of this reaction mechanism are unclear, and we are

currently working to clarify the reaction mechanism in our research laboratory. So far, we have demonstrated by using a chemiluminescence method and an infrared spectral method that the above reaction mechanism is an oxygen reaction in which peroxides and hydrogen peroxides are intermediate products. We will not attempt to describe the decomposition mechanism in detail, but will carry out macroscopic studies based on the measurement of the heating values of NG and NC described in the previous section.

There is a substantial body of research on the combustion of double-base propellants, and it has been learned that the structure of the combustion waves and main reactions are like those shown in Figure 12. Reaction 1 is a homolysis of the bonding of oxygen and nitrogen in a nitrate ( $\text{RONO}_2$ ); it occurs in the condensation phases. Reaction 2 is an exothermic reaction of nitrogen dioxide ( $\text{NO}_2$ ) and aldehydes; it occurs in the condensation phases or in phases very close to these condensation phases. Reaction 3 is an oxygen reaction in which flames are generated by the produced nitric oxide; it does not occur in any inactive gases at atmosphere pressure and is called "Fitz Burning." The heating value in the case of reaction 3 is almost half (about 500 cal/g) of the explosion heating value. Therefore, it is believed that all that is necessary is to consider reaction 2 in experimental conditions at pressures lower than atmospheric pressure and at atmospheric pressures in nitrogen atmospheres used in this research work.

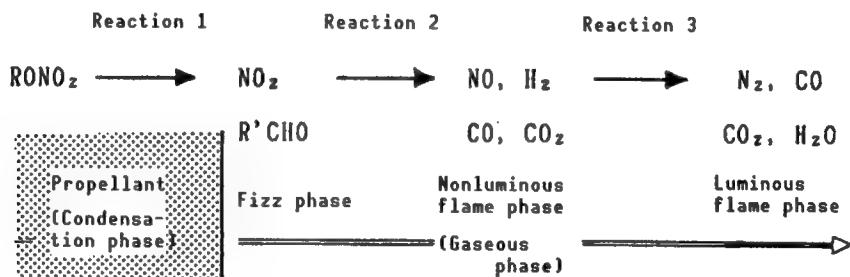


Figure 12. Principal Reactions<sup>1</sup> and Structure of Combustion Waves of Double-Base Propellant

The chemical structural formula of NG is represented by  $(\text{CH}_2\text{ONO}_2)_2$  ( $\text{CHONO}_2$ ). Now, let us suppose that 3 mols of formaldehyde ( $\text{HCHO}$ ) and 3 mols of nitrogen dioxide are produced from 1 mol of NG, respectively, in order to simplify this formula. There has been considerable research on the vapor phase reactions of formaldehyde and nitrogen dioxide, and it is known that reaction rate parameters (activation energy and pre-exponential factor) change at temperatures around  $160^\circ\text{C}$  in the secondary reaction.<sup>12</sup>

The following provides a comparison of the diffusion rate of atmospheric gas and the reaction rate under the conditions of this experiment carried out by taking the characteristic time ( $\tau_{ch}$ ) as a parameter.<sup>13</sup> Assuming that the characteristic reaction time is ( $\tau_{ch}$ ), the half-life is ( $\tau_{1/2}$ ), the reaction rate constant is  $k$  ( $1 \text{ mol}^{-1}\text{second}^{-1}$ ), and the initial concentration is  $a$  ( $\text{mol } 1^{-1}$ ). From this, the following equation can be obtained:

$$\tau_{ch} = \tau_{1/2} = 1/k \cdot a \quad (2)$$

Now, when  $k = 10^{10} e^{-19,000/RT}$  ( $T > 160^\circ\text{C}$ ), it is estimated that a value of  $k = 1.2$  ( $1 \text{ mol}^{-1} \text{ second}^{-1}$ ) can be obtained at a temperature of  $200^\circ\text{C}$  and that a value of  $a = 10^{-2} (\text{mol l}^{-1})$  can be obtained at atmospheric pressures. Therefore,  $\tau_{ch}$  is about 10 seconds. Meanwhile, the characteristic time ( $\tau_D$ ) for molecular diffusion can be represented by the equation:

$$\tau_D = d^2 / 8D \quad (3)$$

Where,  $d$  (centimeter) = width of samples, and  
 $D$  (square centimeters per second) = a diffusion constant

a decrease in pressure will cause a decrease in  $a$  and an increase in the value of  $\tau_{ch}$  in equation (2). However, a decrease in pressure will increase the value of  $D$  and will decrease the value of  $\tau_D$  in equation (3). Therefore, the value of  $\tau_{ch}/\tau_D$  is proportional to the second power of pressure, and with further decreases of this pressure, the possibility of ignition of gaseous phases is further reduced.

Now, substituting the diameter ( $d = 0.1 \text{ cm}$ ) of the samples used in this experiment and the diffusion constant ( $D = 0.5 \text{ cm}^2/\text{s}$ ) for equation (3), we have  $\tau_D = 10^{-3}$  seconds. Therefore, the characteristic time of vapor phase reaction at atmospheric pressures is about  $10^4$  times longer than that of diffusion, the exothermic oxidizing reaction (reaction 2 shown in Figure 13) can be ignored in gaseous phases of aldehyde due to the  $\text{NO}_2$ , and the possibility of ignition in the gaseous phases can be denied.

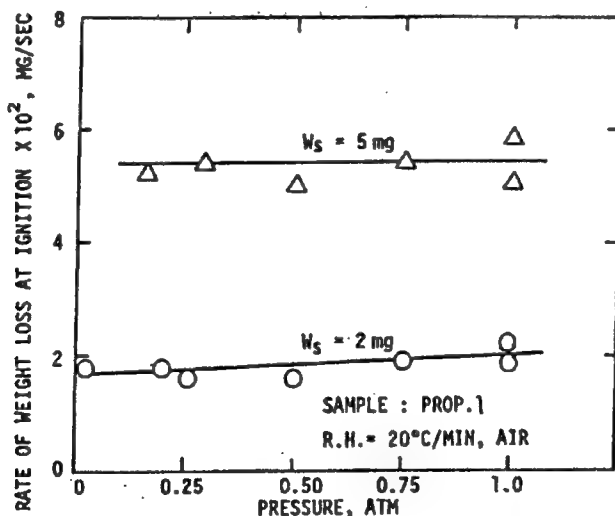


Figure 13. Influence of Pressure on Ignition  
The absence of pressure suggests  
ignition of the condensation phase.

For example, when the diameter of the samples is 10 times that of the above and the pressure is 150 atmospheres both characteristic times for the systems used in this experiment will be equalized. From the results obtained by comparing and studying the characteristic times, we concluded that ignition does not depend on any pressure and partial pressure of oxygen. This conclusion is supported by the measurement results we obtained (Figures 13 and 14).

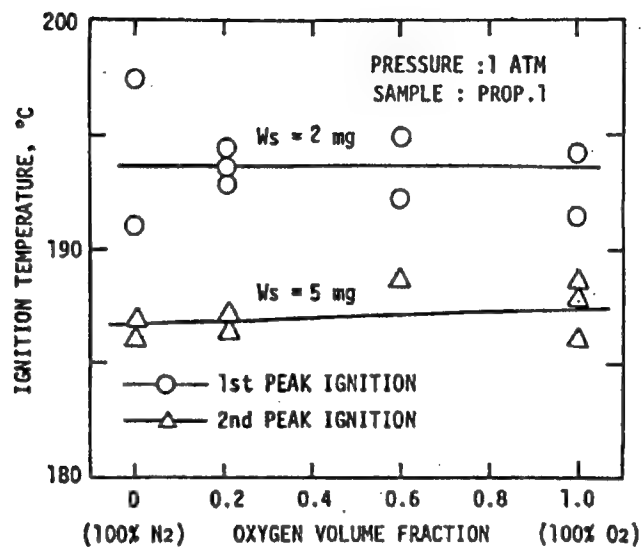


Figure 14. Influence of Oxygen Concentration on Ignition

Ignition is not affected by any amount of oxygen; this suggests ignition at the condensation phase.

#### 4. Conclusion

We have carried out research on the possibility of using thermal analyzers to evaluate LOVA characteristics during low-speed heating together with the thermal ignition characteristics of explosives. We have confirmed that these thermal analyzers are very effective for quantitatively describing the thermal decomposition characteristics of explosives. Double-base propellants are widely used as rocket propellants and propelling charges. We have discovered the following new facts by using such double-base propellants as samples in this research work.

1. The principal components, NG and NC, can be distinguished by analyzing their thermal weights (TG and ?); they appear as exothermic decomposition peaks adjacent to each other.
2. The ignition of double-base propellants during low-speed heating (1~20°C/minute) occurs in the condensation phases. The ignition temperature depends on the heating rate and the weight of the samples, and is close to the exothermic decomposition peak temperature of the main components, NG and NC.

3. When the weight of the samples is constant and the heating rate is raised, ignition due to NC will transit to that due to NG, which is about 10°C lower than the temperature of the ignition due to NC.

Considering the results that have been described above, and the advantage whereby important thermochemical parameters such as heating values, etc., can be ascertained from thermal analyzing measurements, it can be stated as a conclusion that the thermal analyzer is useful for evaluating complex ignition characteristics and for clarifying ignition phenomena.

Also, it is absolutely necessary to clarify the conditions governing ignition (runaway chemical reaction) in order to clarify pure thermal decomposition reactions of propellants that are easy to ignite, explosives, and detonating explosives by using a thermal analyzer.

#### References

1. Fifer, R.A., Chapter 4 "Chemistry of Nitrate Ester and Nitramine Propellant," "Fundamentals of Solid Propellant Combustion," edited by K.K. Kuo and M. Summerfield, AIAA, New York, 1984.
2. Kimura, "Thermal Decomposition and Decomposition Mechanism of Double-Base Propellants in Low Temperature Regions,"  
(a) Japan Defense Agency, TDRI, TECHNICAL REPORT, 1985, p 925;  
(b) DEFENSE TECHNOLOGY, Vol 7, pp 14-28;  
(c) Kimura, J., "Kinetic Mechanism on Thermal Degradation of a Nitrate Ester," PROPELLANT EXPLOSIVES AND PYROTECHNICS, Vol 13, 1988, pp 8-12.
3. Kimura, "Research on Thermal Decomposition (the Second Report) of Nitrate, Thermal Decomposition of PETN, and Self-Oxidizing Reaction," Japan Defense Agency, TRDI, TECHNICAL REPORT, 1988, p 1030.
4. Kimura and Kubota, "Research on Reaction Rate and Thermal Decomposition Reacting Mechanism of HMX,"  
(a) Japan Defense Agency TRDI, TECHNICAL REPORT, 1979, p 784;  
(b) Kimura, J. and Kubota, N., "Thermal Decomposition Process of HMX," PROPELLANT AND EXPLOSIVES, No 5, 1980, pp 1-8.
5. Kirby, C.E. and Suh, N.P., "Reactions Near the Burning Surface of Double-Base Propellants," AIAA J. 9, 1971, pp 317-320.
6. Morrow, S.I., "Thermal and Microscopic Study on the Condensed Phase Behavior of Nitrocellulose and Double-Base Materials," ANALYTICAL CHEMISTRY, Vol 3, edited by R.S. Pomer and J.F. Johnson, Plenum Press, New York, 1974.
7. Vernekker, V.R. Pai and Kishore, K., "Mechanism of Thermal Decomposition of Double-Base Propellants," PROPELLANT AND EXPLOSIVES, Vol 8, 1983, pp 77-79.

8. Musso, R.C. and Grigor, A.F., "Decomposition of Propellant Ingredients and Ingredients Combinations," AIAA Paper 68, 1968, p 495.
9. Ozawa, T., J. THERM. ANAL., Vol 2, 1970, pp 301-324 and Vol 7, 1975, pp 601-617.
10. Adams, G.K., "The Chemistry of Solid Propellant Combustion: Nitrate Ester or Double-Base Systems," in "Mechanisms and Chemistry of Solid Propellants," Edited by A.C. Eringen et al., Pergamon Press, New York, 1967, pp 117-147.
11. Urbanski, T., CHEMISTRY AND TECHNOLOGY OF EXPLOSIVES, Vol 2, pp 52 and 314-315, PWN-Polish Scientific Publishers, Warszawa, 1965.
12. Pollard, H. and Wyatt, R.M.H., "Reactions Between Formaldehyde and NO<sub>2</sub>," Trans Faraday Soc., 1949, pp 760-767.
13. Kimura and Kubota, "Measurement of Explosive Heating Value of Solid Propellants," Japan Defense Agency TRDI, TECHNICAL REPORT, 1976, p 689.

## Performance of Argon-Xenon Laser

906C3824B Tokyo BOEICHO GIJUTSU KENKYUHONBU GIHO (Japan Defense Agency Technical Research & Development Institute) in Japanese Jun 89 Technical Reports, No 5532 pp 1-5

[Article by Takao Komi, Masakatsu Sugii, and Hiroshi Hara, assistant directors general of the Second Research Laboratory of the Third Optical Wave Department of TDRI's Second Research Center: "TDRI Technical Report on Ar-Xe Laser"]

### [Text] Summary

This paper presents the laser performance of Ar-Xe TE laser with UV-preionizers. We obtained a maximum output power of 1.4 mJ at a gas composition of Ar:Xe = 100:1, total pressure of 1 atmosphere with a charged voltage of 25 kV, a main condenser capacity of 60 nF, and a peaking condenser capacity of 54 nF.

### 1. Introduction

The Ar-Xe laser employs photons that are discharged when electrons transit from the 5d orbit to the 6p orbit of an excited Xe atom. These photons have a wide oscillation wavelength of 1-3  $\mu\text{m}^{1,2}$  in the near infrared region. As for this wavelength, a wavelength of 1.73  $\mu\text{m}$  is said to have a comparatively high intensity. A laser with this wavelength<sup>3</sup> possesses the following characteristics: 1) its ability to penetrate the atmosphere is comparatively good; and 2) it is safe for the eyes. Also, this laser theoretically should have a long life, because it employs only inert gases.

Experimental research on such a laser has been conducted since around 1970 and various excitation methods<sup>1-9</sup> have been devised, but the laser is liable to experience arc discharge and it becomes difficult to obtain uniform glow discharge, accompanied by high atmospheric pressure, because the ionization potential of the service gas is comparatively low. At present, high output and high efficiency<sup>9</sup> can be obtained from electric discharge using electron beams, because it is possible to carry out such electric discharge uniformly at 3.5 atmospheres of pressure. However, the electric discharge can never be said to be practical. This is because the operating cost is high and a larger device must be used for the electric discharge. Accordingly, the authors have

begun conducting experiments for the purpose of obtaining greater efficiency, higher output, and high repetition by using a more practical ultraviolet [UV] preionization system, with an eye toward industrial and military applications.

This report, as an interim report, describes output characteristics in the case where the total pressure in a laser tube, the composition ratio expressed in terms of a partial pressure ratio of the laser gas, the reflectivity of the output mirror, and the charging voltage  $C_1$  are changed, respectively, because we have obtained uniform electric discharge in the atmosphere and have succeeded in obtaining oscillation.

## 2. Research Method

Figure 1 shows schematic drawing of an experimental device. The laser tube is made of transparent acrylic resin and is sealed off. It has a preionization pin (cap interval: 2.8 mm) used for arc discharge and a main electrode made from two aluminum bars 420 mm long and 20 mm wide. The electrode interval, discharge length, and discharge width are 20, 390, and 5 mm, respectively.

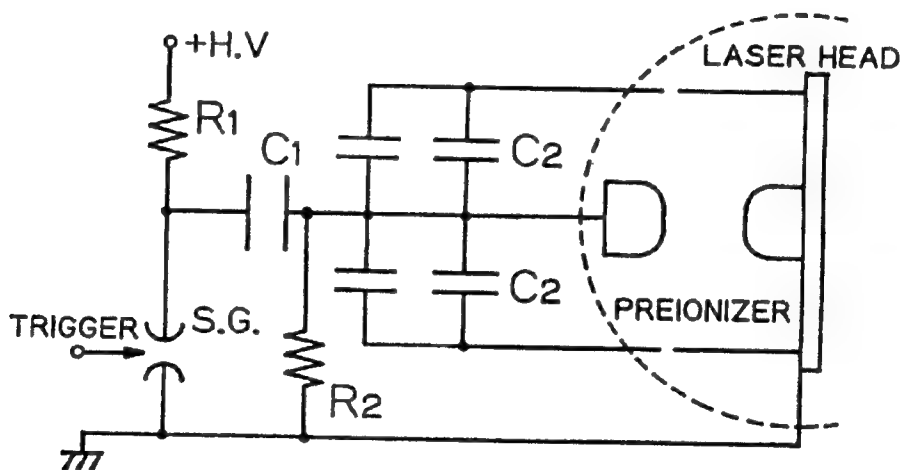


Figure 1. Schematic Drawing of Experimental Device  
+H.V.: High voltage (charging voltage)  
SG: High voltage switch  $R_1 = 5M\Omega$ ,  $R_2 = 10k\Omega$   
 $C_1 = 60 \text{ nF}$ : Main condenser  
 $C_2 = 1,700 \text{ pF} \times 32$ : Peaking condenser

This device has a capacity transfer-type excitation circuit. The operation of this circuit is as follows. First, the main condenser ( $C_1$ —60 nanofarads (nF)) is charged from a high voltage power source through a current limiting resistance  $R_1$ .  $R_2$  is a charging resistance. Next, when the spark gap (SG) is switched in accordance with trigger signals given from a trigger circuit, the electric charge from  $C_1$  will charge the peaking condenser ( $C_2$ ) of 1,700 picofarads (pF)  $\times$  32 (8  $\times$  2 rows  $\times$  2 stages) = 54 nF through the preionization pin. At this time, UV rays will be emitted from the preionization pin, charged particles are produced between the main electrodes, and preionization occurs.

Simultaneously, the main electrodes begin to discharge, energies are supplied from  $C_1$  and  $C_2$ , and laser active media are obtained.

The resonator is stable. A gold mirror made of Be-Cu, with a curvature of 10 m, was used as a totally reflective mirror, while a plane mirror made of fused quartz, with a thickness of 10 mm, was used as the output mirror. The diameter for both mirrors was 50 mm.

The GENTEC ED-100A was used as a highly sensitive-joule meter. Laser beams 20 x 5 mm were focused with a  $\text{CaF}_2$  lens, and measurements were carried out, because the laser output is comparatively small. The total pressure in the laser tube, the composition ratio expressed in terms of the partial pressure ratio of the laser gas, the reflectivity of the output mirror, and the charging voltage of  $C_1$  were all changed in this experiment. The laser output change in the respective cases was measured in each instance.

### 3. Results

The experimental results are shown in Figures 2 to 5. Figure 2 shows the laser output for the case where the charging voltage is changed, using total pressure in the laser tube as a parameter. Figure 3 shows the efficiency for the case. Both laser output and efficiency increase as total pressure increases. The laser output has the maximum value for the charging voltage, except for a total pressure of 200 Torr, and efficiency has its maximum value in the same way. When the total pressure is 200 Torr, even if the charging voltage increases, the laser output will not increase but in fact decreases, and efficiency also decreases. However, it is possible to reduce input energies and to obtain an efficiency that exceeds a maximum value of 400 Torr, because the initial discharge voltage is low. This result demonstrates that if input energies are identical, in order to obtain a high level of output and a high degree of efficiency, it is better to enhance the total pressure. Further, it is possible to obtain the charging voltage that maximizes laser output by means of this total pressure.

Figure 4 shows the effects of changing the composition ratio. The experiment was conducted by using two kinds of partial pressure Ar:Xe ratios—100:1 and 40:1. This experiment demonstrated that when the amount of Xe was small, the laser output was large. However, it is believed that even if the amount of Xe must be small, an optimum value exists, because when there is no Xe there will be no laser output.

Figure 5 shows the result of changing the reflectivity of the output mirror. In this case the charging voltage was used as a parameter. It was learned that an optimum value exists between 20~50 percent in both cases.

Figure 6 shows an example of oscillation and wavelength. The pulse width was about 1.2  $\mu\text{s}$ . The excimer laser has a pulse width of several tens of ns,<sup>10</sup> while this laser output has a comparatively long oscillation.

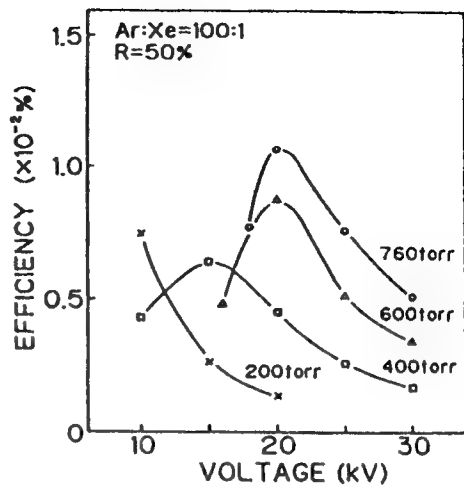
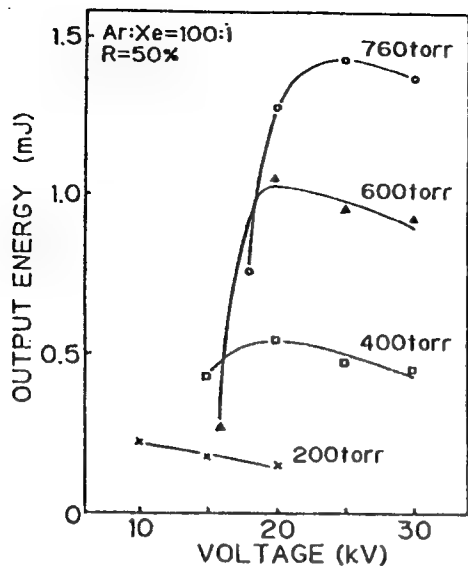


Figure 2. Laser Output According to Charging Voltage When Total Pressure Is Regarded as a Parameter

Figure 3. Efficiency According to Charging Voltage When Total Pressure Is Regarded as a Parameter

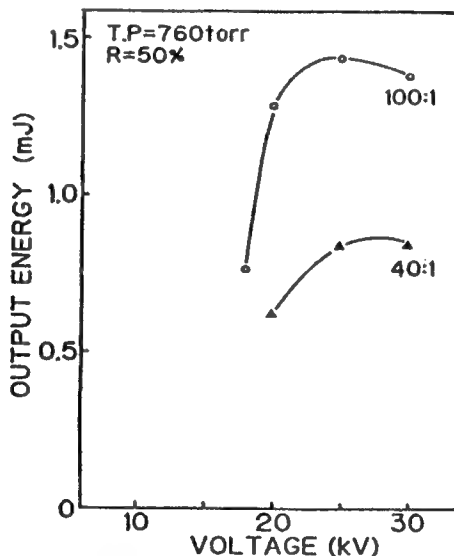


Figure 4. Laser Output According to Charging Voltage When Gas Composition Ratio Is Regarded as a Parameter

Gas composition ratio Ar:Xe  
 Total pressure (TP) = 760 Torr  
 Reflectivity of output mirror R = 50 percent (plane mirror)  
 Curvature of total reflection mirror = 10 m (gold mirror)

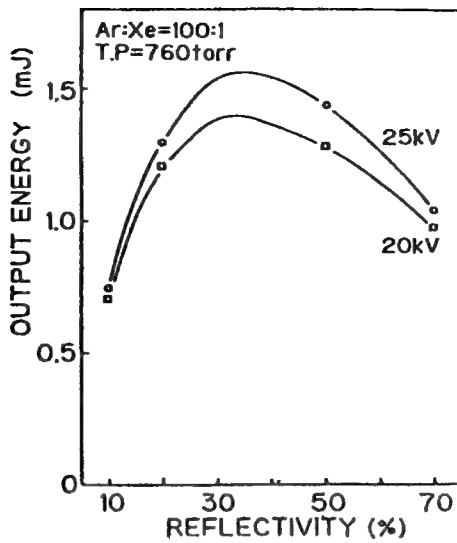


Figure 5. Laser Output According to Reflectivity of Output Mirror When Charging Voltage Is Regarded as a Parameter  
 Gas composition ratio Ar:Xe = 100:1  
 Total pressure (TP) = 760 Torr  
 Curvature of total reflection mirror = 10 m (gold mirror)

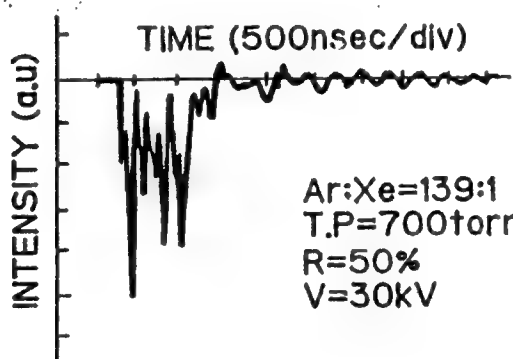


Figure 6. Example of Laser Output Waveform  
 Gas composition ratio Ar:Xe = 139:1  
 Total pressure TP = 700 Torr  
 Reflectivity of output mirror R = 50 percent (plane mirror)  
 Curvature of total reflection mirror = 10 m (gold mirror)  
 Charging voltage V = 30 kV

#### 4. Discussion and Conclusion

The results of these experiments show that it is necessary to increase atmospheric pressure in order to obtain a high level of output and a high degree of efficiency. Also, the results of the composition ratio experiment show that it is desirable to increase the amount of Ar dramatically rather than that of Xe. This means that the collision of Ar atoms is directly related to the formation of the laser upper order and that it is difficult to form such a laser upper order when Xe atoms collide with each other.<sup>9</sup> That is, it

is desirable to increase the number of Xe atoms in a state where only Ar atoms exist around Xe atoms. In order to form this state, it is necessary to increase not only the pressure, but also the composition ratio in conjunction with the increased pressure. However, when the pressure in the laser tube is increased, main discharge will not readily occur, while discharge between the cathode electrode and the pin electrode for preionization will be facilitated. For this reason, it is necessary to study the conditions under which this discharge occurs and the shape of the electrodes during preionization, and to improve the laser tube to prevent this discharge from readily occurring.

Also, it was learned from the experiment that the accumulated energies (input energies) are comparatively large,<sup>6,8</sup> because the capacity of the main condenser is 60 nF. These energies are consumed to accelerate ions and electrons ionized in the preionization system and to further ionize many Xe atoms and Ar atoms. It is considered, however, that surplus energies formed after these Xe and Ar atoms are ionized may cause reionization of the Xe atoms excited in the laser upper order. It is also believed that, because of this fact, the number of such Xe atoms will decrease and that efficient pumping will become impossible. Accordingly, in order to form the laser upper order efficiently, it is probably necessary to form optimum kinetic energies for electrons.

In the future, we plan to optimize the excitation circuit, improve the preionization system with a view to obtaining uniform discharge at high atmospheric pressure, and increase the laser's output and efficiency following the recommendations discussed above.

#### References

1. Schwarz, S.E., et al., "High-Pressure Pulsed Xenon Laser," APPLIED PHYS. LETT., Vol 17, 1970, p 305.
2. Targ, Russel, et al., "High-Repetition-Rate Xenon Laser With Transverse Excitation," IEEE J. QUANTUM ELECTRON., Vol QE-8, 1972, p 166.
3. Newman, L.A., et al., "High-Pressure Infrared Ar-Xe Laser System: Ionizer-Sustainer Mode of Excitation," APPL. PHYS. LETT., Vol 27, 1975, pp 678.
4. Lawton, S., et al., "The High-Pressure Neutral Infrared Xenon Laser," J. APPL. PHYS., Vol 50, 1979, p 3888.
5. Silfvast, W.T., et al., "CO<sub>2</sub>-Laser Produced Plasma-Initiated Neutral-Gas Recombination Lasers," Ibid., Vol 50, 1979, p 7921.
6. Collier, F., et al., "High Pressure Infrared Xenon Laser Excited by a UV Preionized Discharge," Ibid., Vol 52, 1981, p 6021.

7. Danilychev, V.A., et al., "Investigation of a Plasma Recombination Laser Utilizing an He-Ne Mixture Excited by  $\lambda = 10.6 \mu$  Laser Pulses," Sov. J. QUANTUM ELECTRON., Vol 12, 1982, p 58.
8. Collier, F.S., et al., "High-Efficiency Infrared Xenon Laser Excited by a UV Preionized Discharge," IEEE J. QUANTUM ELECTRON., Vol QE-19, 1983, p 1129.
9. Basov, N.G., et al., "60J Quasistationary Electroionization Laser on Xe Atomic Metastables," Ibid., Vol QE-21, 1985, p 1756.
10. Preproceedings of the 46th Applied Physics Scientific Lecture Meeting, 1985.

## Burn Rate of Rocket Motors Reduced

906C3824C Tokyo BOEICHO GIJUTSU KENKYUHONBU GIHO (Japan Defense Agency Technical Research & Development Institute) in Japanese Jun 89 Technical Reports, No 5540 pp 1-13

[Article by Kousei Miyata, assistant director general of the Third Research Laboratory of the Second Prime Mover Department of TDRI's Third Research Center, and Naminosuke Kubota, assistant director general of the Second Research Laboratory of the Second Prime Mover Department of TDRI's Third Research Center: "Burning Rate Reduction of AP Composite Propellant by  $\text{SrCO}_3$  Addition"]

### [Text] Summary

The burning rate of AP (ammonium perchlorate) composite propellants is decreased significantly by the addition of  $\text{SrCO}_3$  without increasing the pressure exponent of the propellant burning rate. Results of microthermocouple measurements show that surface temperature,  $T_s$ , is increased from 700~970 K by the addition of  $\text{SrCO}_3$ , although the heat release from the gas phase to the burning surface,  $(dT/dt)_{s+}$ , remained unchanged. DTA (differential thermal analysis) and TG (thermogravimetry) experiments were also carried out under Ar flow conditions. The AP decomposition temperature,  $T_{ds}$ , is increased from 590~620 K by the addition of  $\text{SrCO}_3$ .

### 1. Introduction

The rocket motor is a propulsion engine which passes gas generated by the combustion of propellants through nozzles, which in turn discharge the gas to the outside at supersonic speeds. Thrust is produced by the reaction generated by the discharge. A particular characteristic of the solid rocket motor is that once the propellants have been ignited, it cannot be controlled until the combustion is completed. Therefore the gas generating speed (i.e., burn rate) of the propellants is an important parameter to be taken into account when designing a rocket motor.

The burn rate of propellants depends on their physicochemical properties, and these propellants possess limited burning rate spectrum characteristics. Therefore, in order to enhance the performance of rocket motors, it is

necessary to increase the burn area of propellants, and in order to do so, it is necessary to carry out research on increasing and decreasing the burn rate of propellants.<sup>1</sup>

There are a number of ways to increase burn rate. These include increasing the energy contained in the propellants, raising the thermal conductivity of the burning surface, and chemically promoting the burning reaction by the addition of catalysts.<sup>1,12</sup> There has been considerable research on increasing burn rate, and the results obtained from this research work have been put to practical use, taking advantage of the fact that this increase can be obtained by raising the specific impulse.<sup>2-8</sup>

By contrast, little research on decreasing burn rate has been carried out, because it is very difficult to lower burn rate while minimizing decreases in the energies contained in the propellants.

To address these problems, Glaskova, et al.,<sup>9</sup> have advocated a methodology for lowering the burn rate by controlling the chemical reaction. This methodology indicates the following methods for delaying this chemical reaction by altering the decomposition of ammonium perchlorate [AP], which is an oxidizer used in propellants.

- 1) Addition of a substance that shifts the equilibrium condition of the AP decomposition reaction to the lift side.
- 2) Addition of a substance that combines with perchloric acid or its decomposition product to form a product that is less reactive than perchloric acid or AP.
- 3) Addition of a substance that inhibits the decomposition of perchloric acid.

The use of these substances will reduce the burn rate of propellants, because they inhibit the oxidizing reaction of ammonium.

In recent years, there has been a tendency for the operating time of rocket motors to become longer (in units of seconds). For this reason, it is necessary to use propellants that contain greater energies than conventional propellants and that have lower burn rates. However, there has been little research on decreasing burn rate through the use of so-called negative catalysts.<sup>9-11</sup>

LiF and SrCO<sub>3</sub> have proven to be effective negative catalysts for composite propellants based on AP. Hirata, et al.,<sup>10</sup> have carried out research on this subject, particularly on LiF, and have identified a physicochemical mechanism for reducing burn rate. However, little research on SrCO<sub>3</sub> has been carried out, and a similar mechanism has not been identified. In our research work, we have identified a number of the characteristics of SrCO<sub>3</sub> and have studied its effectiveness in reducing burn rate.

## 2. Sample Propellant

A sample propellant was made on a trial basis to investigate the influence of strontium carbonate. This work was undertaken in cooperation with the Asahi Chemical Industry Co. The composition of this propellant is shown in Table 1. Composition N is for reference and does not contain any strontium carbonate. Composition C contains 2 percent strontium carbonate; all other components are the same as in composition N.

Table 1. Composition of Sample Propellant

Propellant	HTPB	AP	Diameter ( $\mu\text{m}$ )			$\text{SrCO}_3$
			400	200	10	
N	12	88	34	33	33	0
C	12	88	34	33	33	2

## 3. Experimental Method

### 3.1 Measurement of Burn Rate

The sample propellant was formed into a long strand measuring 7 x 7 x 80 mm. It was coated with a restrictor made of silicon rubber. The burn rate was measured using a fuse wire method. The interval of the fuse wire is 20 mm. The propellant was pressurized up to a specified pressure by injecting  $\text{N}_2$  gas into a chimney-type strand combustor.

### 3.2 Measurement of Burn Rate and Temperature Sensitivity

The experiment was conducted by setting a chimney-type strand combustor in a constant temperature bath and by setting the strand temperature and the  $\text{N}_2$  gas temperature, and the environmental temperature, at 243 and 343 K, respectively. The temperature adjusting time was set at 72 hours or more. Also, the method used to measure the burn rate is the same as that described in the previous item.

### 3.3 Measurement of Combustion Waves by Microthermocouple

A strand testpiece measuring 7 x 7 x 20 mm was divided longitudinally into halves and a microthermocouple with a diameter of 12.5  $\mu\text{m}$  (Pt-Pt 10 percent Rh) was put and fixed between the cut surfaces by means of a strand. Polyvinyl alcohol [PVA] was used to bond the strand. The strand testpiece was left as it was at room temperature for 7 days until the PVA hardened completely.

It is possible to handle homogeneous propellants like double-base propellants, because their flame structures are homogeneous and can be regarded as one-dimensional structures. If very thin thermocouples are used in such propellants, the measurement results obtained from time areas can easily be

converted into those obtained from spatial areas. However, the flame structure of composite propellants is two-dimensional, and such conversion cannot be done readily. This is because these composite propellants are characterized by a diffusion flame generated by the oxidizers and fuel components. Also, the spatial resolution capability is insufficient, because both the particles of the oxidizers and the thermocouple junctions have limited sizes. A qualitative assessment was made on the basis of the averaged results in terms of time and space by using a thermocouple with a slightly large wire diameter.

### 3.4 Thermal Analyzing Experiment

Differential thermal analysis [DTA] and thermogravimetry [TG] were carried out simultaneously as thermal analyzing experiments in this research work. The rate at which temperature rose in the Ar gas atmosphere (40 ml/min) was 20 K/min, and the temperature range was from 293~773 K. The Al sealing cell was used as a sample cell.

## 4. Experimental Results and Discussion

### 4.1 Burn Rate Characteristics

Figure 1 shows temperature sensitivity characteristics and burn rate characteristics of base propellants and propellants to which negative catalysts were added.

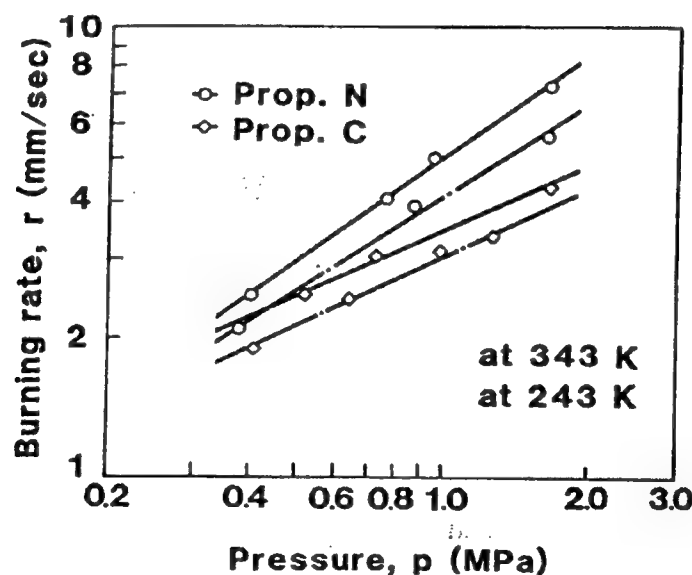


Figure 1. Burn Rate Characteristics

In the case of the base propellants, logarithms of the burn rate were changed almost linearly against logarithms of pressure. The addition of  $\text{SrCO}_3$  to these base propellants will lower the burn rate.

Empirically, the burn rate of propellants is represented by the following equation:

$$r = a \cdot p^n \quad (1)$$

Where,

r: Burn rate  
a: Constant  
p: Pressure  
n: Pressure exponent of propellant burn rate

Paying attention to the effectiveness of catalysts, it can be recognized that the effectiveness of a decrease in burn rate is remarkable on the higher pressure side. That is, the pressure exponent n of the burn rate of base propellants is lowered from 0.77 to 0.50 at a temperature of 343 K and from 0.70 to 0.55 at 243 K, respectively.

LiF has proven to be effective as a negative catalyst affecting the burn rate of composite propellants based on AP. It is known that the addition of LiF to such propellants is unfavorable in practical terms because adding it dramatically increases<sup>10</sup> the pressure exponent, n.

SrCO<sub>3</sub> has the same negative catalyst effectiveness as LiF. SrCO<sub>3</sub> is believed to be more superior as a negative catalyst than LiF in terms of decreasing the pressure exponent, n.

#### 4.2 Temperature Sensitivity Characteristics

Temperature sensitivity,  $\sigma_p$  of the burn rate of propellants is defined by the following equations:

$$\sigma_p = d(\ln r)/dT_0 \quad (2)$$

Substituting equation (1) for equation (2),

$$\sigma_p = 1/a \cdot (da/dT_0)_p \quad (3)$$

Where,

$\sigma_p$ : Temperature sensitivity of burn rate  
 $T_0$ : Initial temperature of the propellant

When no catalyst is added to a propellant, there is a tendency for the temperature sensitivity to rise slightly together with an increase in pressure, but when negative catalysts are added to propellants, these propellants will lose the pressure dependency of the temperature sensitivity,  $\sigma_p$ , and, as shown below, the temperature sensitivity will become almost constant, as shown by the equation  $\sigma_p = 1.33 \times 10^{-3} (1/K)$ .

#### 4.3 Study of Burn Rate Equation

Analyzing the combustion of propellants using a coordinate system based on the burning surface reveals that the following temperature distribution (combustion wave structure) is formed.<sup>1,12,13</sup> Figure 2(1) is an example of a measurement of the combustion wave structure of sample propellants, while Figure 2(b) shows a typical pattern.

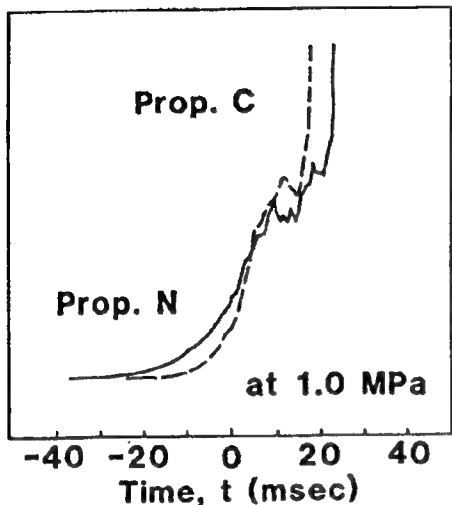


Figure 2(a). Sample Measurement of Combustion Waves Using a Thermocouple

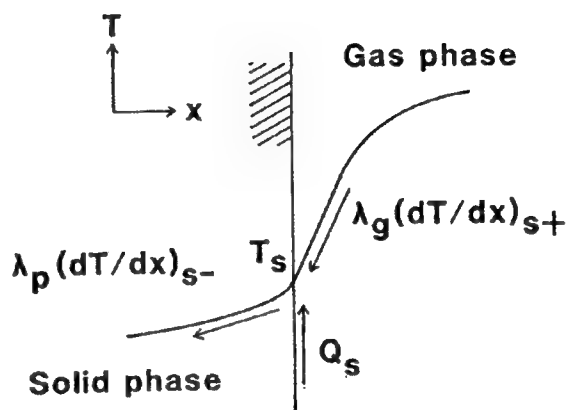


Figure 2(b). Structural Model of Combustion Wave

The initial temperature,  $T_0$ , of the propellant rises sharply in the vicinity of the burning surface, and reaches  $T_s$  at the burning surface. Decomposition gases generated from the burning surface cause an exothermic reaction while flowing downstream at a certain speed. Therefore, a sharp temperature gradient is formed in the gas phase, and the temperature reaches the final flame temperature,  $T_f$ . When part of the heat generated from the gas phase is fed back to the burning surface, and when a stable combustion wave structure is formed, propellants will burn at a steady rate. The thermal equilibrium at that time is represented by the following equation:

$$\lambda_p (dT/dx)_{s-} = \lambda_g (dT/dx)_{s+} + \rho_p \cdot r \cdot Q_s + I_f \quad (4)$$

Where,

T: Temperature

x: Distance

r: Burn rate

$Q_s$ : Heat of reaction at the burning surface

$I_f$ : Heat feedback from the luminous flame zone to the burning surface by radiation

$\lambda$ : Density  
 $\rho$ : Thermal conductivity  
 $p$ : Propellant  
 $g$ : Gas phase  
 $s-$ : Propellant at the burning surface  
 $s+$ : Gas phase at the burning surface

The left side of equation (4) shows the thermal movement from the burning surface to the solid phase. The first term of the right side shows the thermal movement from the gas phase to the burning surface. The second term shows the exotherm or the endotherm on the burning surface, and the third term shows the thermal movement by radiation from the final flame to the burning surface. It is generally believed that the third term of the right side can be ignored. The combustion wave shown on the left side is two-dimensional, and, in the case of steady-state combustion, the following equation can be obtained from the law of the conservation of energy:

$$d(\lambda_p \cdot dT/dx)/dx - \rho_p \cdot r \cdot dT/dx = 0 \quad (5)$$

Integrating equation (5) in boundary conditions ( $x = 0$ ,  $T = T_s$ , and  $x = -\infty$ ,  $T = T_0$ ), the following equation can be obtained:

$$\lambda_p (dT/dx)_{s-} = \lambda_p \cdot r \cdot c_p (T_s - T_0) \quad (6)$$

Where,

$c$ : Specific heat

As shown in the following equation, the burn rate can be represented by combining equations (4) and (6):

$$r = \frac{\lambda_p (dT/dx)_{s+}}{\rho_p \cdot C_p (T_s - T_0 - Q_s/C_p)} \quad (7)$$

Rewriting this equation, the following equation can be obtained:

$$r = \alpha_s \cdot \Phi/\psi \quad (8)$$

Where,

$$\Phi = (dT/dx)_{s+} \quad (9)$$

$$\psi = (T_s - T_0 - Q_s/C_p) \quad (10)$$

$$\alpha_s = \lambda_g/C_p \cdot \rho_p \quad (11)$$

That is, the causes of reduced burn rates in propellants can be found in increases in the temperature gradient,  $(dT/dx)_{s+}$ ; in increases in surface temperature,  $T_s$  of the solid phase; or in decreases in the exotherm,  $Q_s$ , on the solid surface.

#### 4.4 Change of Surface Temperature

The surface temperature,  $T_s$ , of the propellants was determined on the basis of the results of the strand combustion test conducted by using a microthermocouple. Figure 3 shows these results.

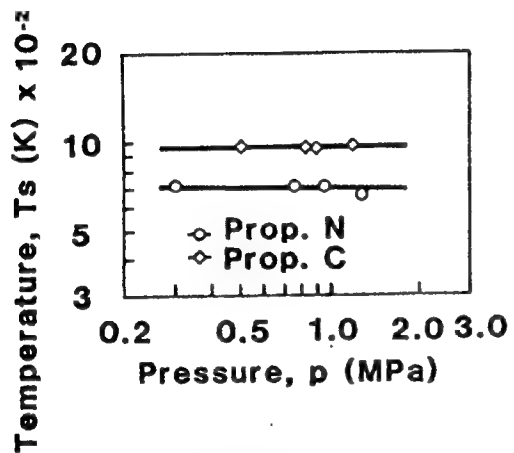


Figure 3. Combustion Surface Temperature

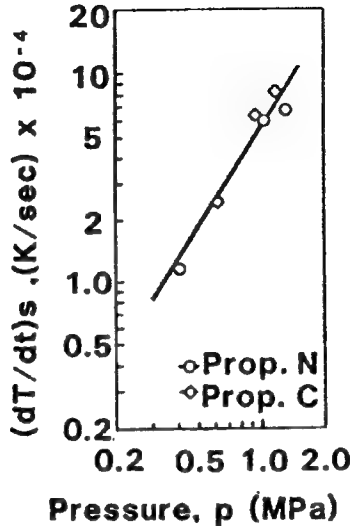


Figure 4. Temperature Change Rate in Gaseous Phase

$T_s$  of base propellants does not depend on pressure but is constant, being about 700 K. By contrast, it was ascertained that there was no pressure dependence in propellants to which negative catalysts were added, but that the  $T_s$  of these propellants was increased up to about 970 K. It is believed that the surface temperature of the sample propellants rises and lowers the burn rate.

#### 4.5 Change of $(dT/dt)_{s+}$ by Addition of Negative Catalyst, $\text{SrCO}_3$

As shown in the following equation, the temperature gradient  $(dT/dx)_{s+}$  in the gas phase can be represented from equation (9):

$$dT/dx = dT/dt \cdot dt/dx = r^{-1} \cdot dT/dt \quad (12)$$

Therefore, the change of gas phase reactions can be studied by using the rising temperature rate,  $(dT/dt)_{s+}$ , of the gas phase adjacent to the burning surface as a parameter.  $(dT/dt)_{s+}$  can be determined on the basis of the experimental results obtained by using a microthermocouple.

Figure 4 shows the result obtained by plotting the change of  $(dT/dt)_{s+}$  against pressure. No large change can be seen in spite of the decrease in burn rate. That is, it is believed that strontium carbonate does not affect the gas phase reactions of propellants.

#### 4.6 Exotherm, $Q_s$ , on Burning Surface

Substituting equation (12) for equation (7) and solving for  $Q_s$ , the following equation can be obtained:

$$Q_s = C_p \cdot (T_s - T_0) - \lambda_g / \rho_p \cdot (dT/dt) \cdot (1/r)^2 \quad (13)$$

Figure 5 shows the result of calculating  $Q_s$  on the basis of equation (13) and the measurement results that have been obtained up to now. It can be seen that the addition of  $\text{SrCO}_3$  will increase about 40 percent of  $Q_s$  on the average.

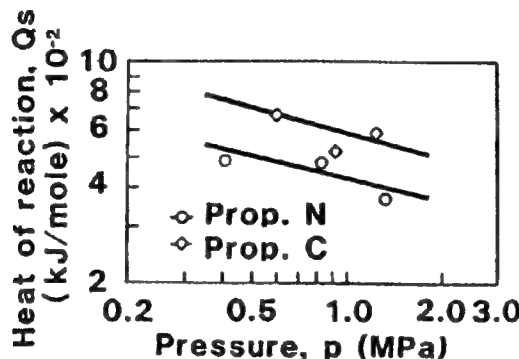


Figure 5. Heat of Reaction of Combustion Surface

#### 4.7 Discussion on Negative Catalyst Effectiveness for Burn Rate

As a result of studying the combustion wave structure adjacent to the burning surface on the basis of the experimental results that have been obtained up to now, the following conclusions can be drawn.

Assuming that the addition of catalysts will change the burn rate from  $r_n$  to  $r_c$ , the following equations can be obtained by using equation (8):

$$r_n = \alpha_{s,n} \cdot \Phi_n / \psi_n \quad (14)$$

$$r_c = \alpha_{s,c} \cdot \Phi_c / \psi_c \quad (15)$$

Where, index n means no addition of catalysts, and index c means addition of catalysts. In the same way, the temperature rising rate  $(dT/dt)_{st}$  on the burning surface can be given by the following equations on the basis of equation (12):

$$(dT/dt)_{st,n} = r_n \cdot (dT/dx)_{st,n} \quad (16)$$

$$(dT/dt)_{st,c} = r_c \cdot (dT/dx)_{st,c} \quad (17)$$

Now, assuming that the percentage of change in the burn rate obtained by the addition of catalysts is  $\Xi$ , the following equation can be obtained on the basis of the relations in equations (8) to (11) and (14) to (17):

$$\Xi = r_c/r_n$$

$$= \sqrt{\frac{(T_{s,n} - T_0 - Q_{s,n}/C_p) (dT/dt)_{s+,n}}{(T_{s,c} - T_0 - Q_{s,c}/C_p) (dT/dt)_{s+,c}}} \quad (18)$$

Let the physical property values of the propellants and their combustion gas remain unchanged even by the addition of catalysts thereto. According to the results of the thermochemical measurements carried out in this research work, it can be understood that the addition of  $\text{SrCO}_3$  will have little effect on gas phase reactions. That is, the following equation can be obtained, because the addition of catalysts will not change  $(dT/dt)_{s+}$ , which shows the reaction rate in the gas phase:

$$(dT/dt)_{s+,n} = (dT/dt)_{s+,c} \quad (19)$$

Therefore, equation (18) can be represented by the following equation:

$$\Xi = \sqrt{\frac{T_{s,n} - T_0 - Q_{s,n}/C_p}{T_{s,c} - T_0 - Q_{s,c}/C_p}} \quad (20)$$

The heat of the reaction on the burning surface can be studied by using equation (2) on the basis of the relationship between the burn rate shown in Figure 1 and the burning surface as shown in Figure 4. As shown in Figure 5, the addition of catalysts will increase  $Q_s$  by an average of about 40 percent, Figure 6, meanwhile, shows the result of calculating  $Q_s$  on the basis of equation (20).

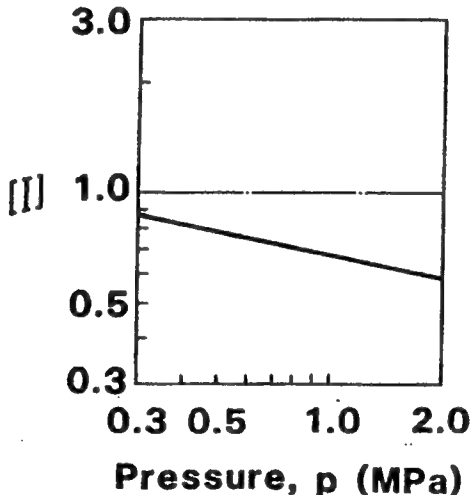


Figure 6. Change in Burn Rate

There is a tendency for an increase in the exotherm,  $Q_s$ , on the burning surface to raise the burn rate as shown in equation (8). However, when the balance of heat adjacent to the surface of the propellants is considered as a whole,  $(dT/dt)_s$  does not change, but  $T_{s,c}$  becomes sufficiently large. As a result,  $\Xi < 1$  is obtained from equation (20), and the burn rate is lowered.

On the basis of the above discussion, it can be seen that an increase in the burning surface temperatures of composite propellants based on AP will enable strontium carbonate ( $\text{SrCO}_3$ ) to reduce the burn rate.

#### 4.8 Influence of Negative Catalyst on Decomposition Reaction of Oxidizer

It is believed that the addition of strontium carbonate will affect the decomposition reaction of AP, which is an important component of propellants.<sup>5,14</sup> Therefore, these mixtures were thermally analyzed.

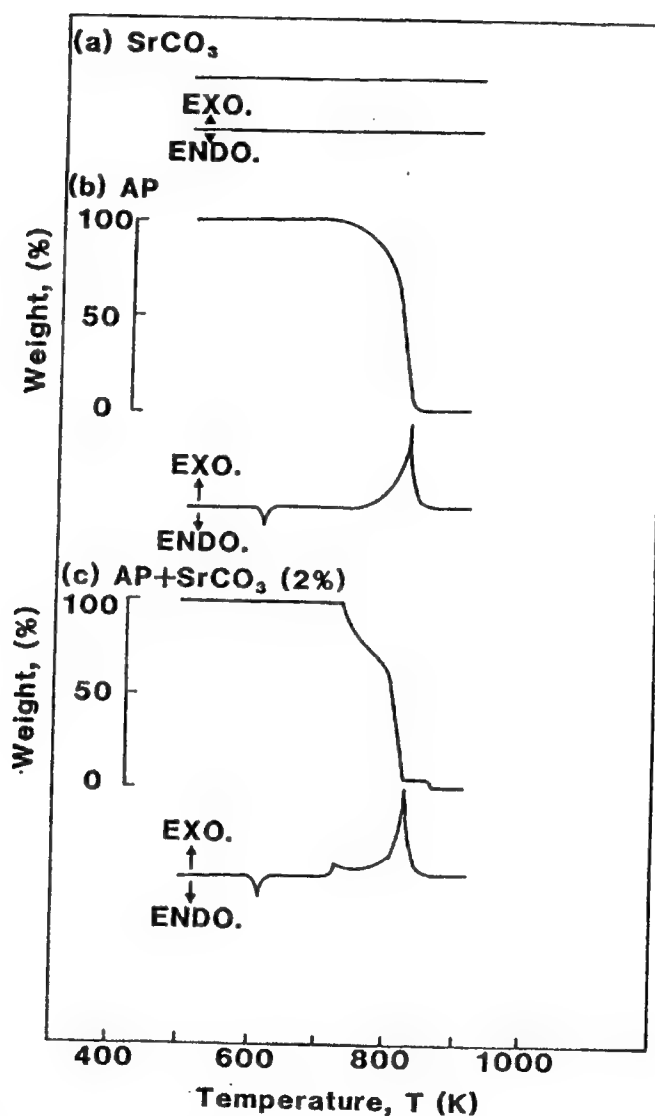


Figure 7. Result of Thermochemical Analysis

Figure 7 shows the DTA curves and TG curves of strontium carbonate, AP, and mixtures of these elements. Figure 7(a) shows the result of a thermal analysis of strontium carbonate as a simple substance. This shows that no change is

observed in either the DTA or TG curves at temperatures ranging up to 730 K. However, when the temperature is raised to 1,280 K by using an open cell made of aluminum ( $Al_2O_3$ ) as a sample cell, an endothermic decomposition reaction will occur at temperatures exceeding 1,000 K. Calculating the weight reducing rate at this point, the following equation can be obtained:



This result corresponds with the mass of  $CO_2$  in the case where such a reaction is assumed. Accordingly, it can be considered that the above reaction occurs in strontium carbonate as a simple substance at temperatures of 1,000 K or more.

Figure 7(b) shows the result of a thermal analysis of AP as a simple substance. An endothermic peak can be seen in the vicinity of 480 K in the DTA curve of AP, an exothermic reaction begins in the vicinity of 590 K, and a large exothermic peak can be seen in the vicinity of 740 K. Looking at the TG curve in this case, there is no change in weight at the endothermic peak at a temperature of 480 K. The endothermic peak at this temperature is due to the crystal transformation of AP.

In comparing the DTA and the TG curves, it can be seen that both weight reductions start simultaneously at a temperature of 590 K, which in turn, starts an exothermic reaction. The weight reduction at the exothermic peak is remarkable, and represents 99 percent or more of the initial loss of mass of the sample. Considering the level of experimental accuracy, it can be considered that the sample decomposed completely. It is known that the decomposition process of AP is a multistage reaction, and, finally, all components are gasified through a reaction shown in the following equation. For this reason, it is believed that the results shown in the TG curve were obtained.



This matter is the result of thermally analyzing strontium carbonate and AP as simple substances. The result shown in Figure 7(c) was obtained from the thermal analysis curves of mixtures made by adding 2 percent (wt) of strontium carbonate to AP. In the same way as in the case of AP, which is a simple substance, the exothermic peak shows a crystal transformation point, and the temperature in this case shows little change.

The large influence of the addition of strontium carbonate can be seen in the temperature range where an exothermic reaction occurs. A slight exothermic reaction occurs in AP when used as a simple substance, but the addition of catalysts will cause a sharply exothermic reaction. The TG curve in this case shows that the weight reduction begins in the vicinity of 520 K; when AP was used as a simple substance, this onset temperature is shifted by about 30 K to the high temperature side, and the curve inclination is large. That is, the starting time and the weight reducing reaction is delayed considerably, and the effectiveness of an increase in this reaction rate is recognized.

Also, the exothermic peak, which shows the maximum exotherm, occurs at about 730 K. Compared with AP used as a simple substance, this temperature is shifted by about 10 K to the low temperature side. Also, the exothermic research is particularly sharp in this case. Seeing the T<sub>g</sub> curve after this exothermic peak, the weight reducing rate is about 98 percent, and about 2 percent remains in some compound form. A further rise in temperatures will gasify this substance.

The total exotherm caused by reactions can be estimated by integrating the DTA curve. Then, the respective integrated values shown in Figures 7(b) and (c) were compared with each other, but little change was seen in these values. This fact indicates that the addition of strontium carbonate will not change the heat insulating flame temperature of propellants.

We have already mentioned that the weight reduction reaction starting point is dramatically shifted to the high temperature side in the TG curve. That is, it is considered that strontium carbonate delays the start of the exothermic decomposition reaction of AP. This reaction starting point temperature was taken as T<sub>ds</sub>, and was studied.

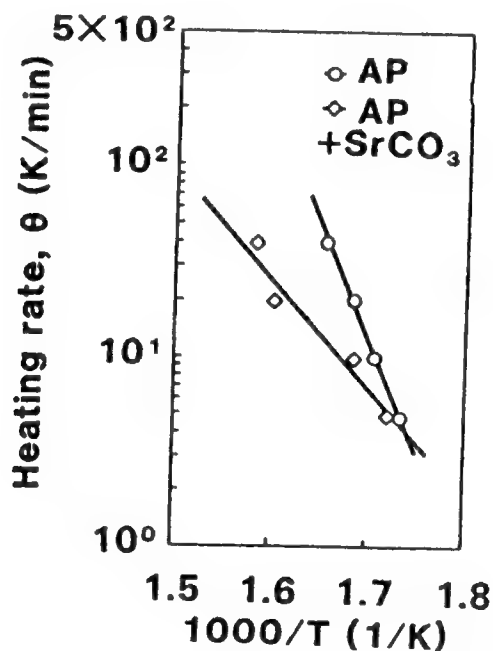


Figure 8. Change of Activation Energies

Let the reaction to be studied be an Arrhenius-type reaction. Now, the temperature rising rate,  $\theta$ , is lower than the burn rate of pellets in the thermal analyzing test. Figure 8 shows the result of studying an area with a higher temperature rising rate by using the relation ( $\theta$  vs  $1,000/T$ ) between the temperature rising rate ( $\theta$ ) and actual temperatures. The linear inclination shown in Figure 8 indicates activation energies. Therefore, the activation energy of AP at T<sub>ds</sub> is 220 kJ/mole, and when strontium carbonate is

added to AP, the figure becomes 101 kJ/mole. It can be appreciated that the addition of strontium carbonate to AP will lower the activation energy of AP at  $T_{ds}$ .

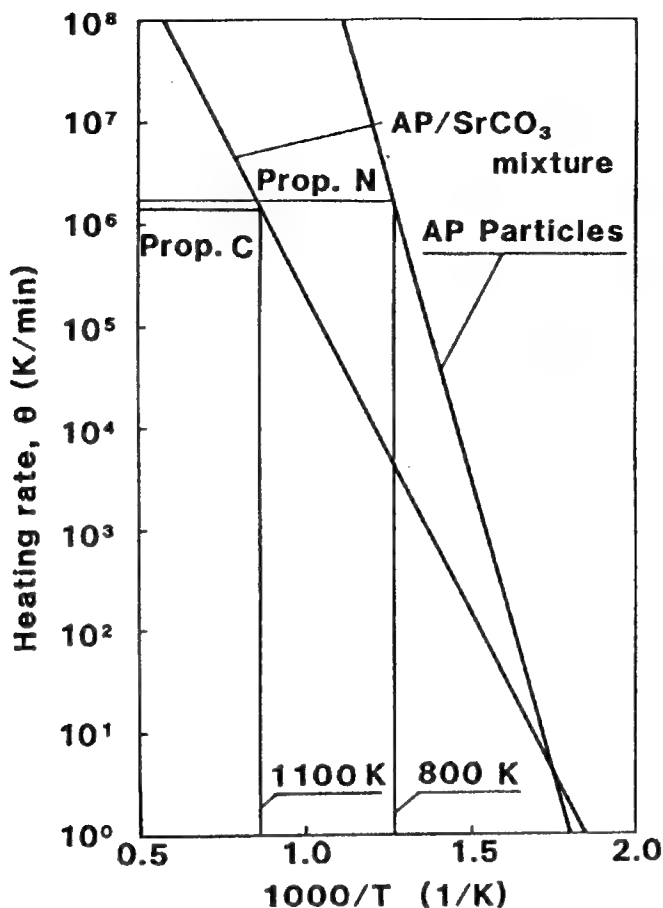


Figure 9. Expansion of Heating Rate Region

When the straight lines shown in Figure 8 are extended up to a temperature rising rate equivalent to the burn rate of propellants, the straight lines shown in Figure 9 can be obtained. Reading the temperatures in reverse order from the respective burn rates it can be seen that the temperature in the case of AP as a simple substance is about 1,100 K, and that when strontium carbonate is added the temperature becomes about 800 K. This result accords almost exactly with that obtained by measuring the surface temperature by means of a thermocouple. That is, it can be said that the process of the reactions generated by thermal analyses is left as it is, and the reaction between AP and strontium carbonate is the same as a chemical reaction of burning propellants.

That is, the addition of strontium carbonate to AP will raise the decomposition temperature,  $T_{ds}$ , of AP. As a result, the surface temperature,  $T_s$ , of propellants rises. Subsequent reaction processes are accelerated, because the activation energy at that time is lowered. As a result,  $Q_s$  will increase. The reaction of the gas phase,  $(dT/dt)_{s+}$ , is measured by using a thermocouple, but

there is no change. Therefore, it can be understood that strontium carbonate does not affect this reaction. Eventually, the change in the decomposition process of AP will change the burn rate of propellants.

### 5. Conclusion

As the result of measuring temperatures by means of a thermocouple, it was ascertained that when strontium carbonate was added to composite propellants, the heat of the reaction,  $Q_s$ , and the surface temperature,  $T_s$ , would sharply increase on the burning surface, and the temperature rising rate,  $(dT/dt)_{s+}$ , would not change on the burning surface. The reaction between AP and strontium carbonate was analyzed and studied thermally. As a result, it was determined that strontium carbonate raised the decomposition temperature,  $T_{ds}$ , of AP. It can be considered that this reaction system is the same as that in the case of burning propellants.

That is, the addition of strontium carbonate will raise the decomposition temperature of AP. The gas phase of the combustion wave structure has no exothermic change, and the change of heating the reaction on the burning surface is comparatively small. With regard to the heat balance in this case, an equilibrium condition is attained by a decrease in the backward rate on the burning surface, i.e., the burn rate of propellants.

### References

1. Kubota, N., "Outline of Rocket Engineering," Defense Technical Association, 1981.
2. Pittman, Jr., C.U., "Location of Action of Burning-Rate Catalysts in Composite Propellant Combustion," AIAA JOURNAL, Vol 7 No 2, 1969.
3. Strahle, W.C., Handley, J.C. and Milkie, T.T., "Catalytic Effects in the Combustion of AP-HTPB Sandwiches to 3200 psia," AIAA paper 72-1120, 1972.
4. Bakhman, N.N., Nikiforov, V.S., Avdyunin, V.I., Fogelzang, A.E. and Kichin, Yu. S., "Catalytic Effect of Ferrous Oxide on Burning Rate of Condensed Mixtures," COMBUSTION AND FRAME, Vol 22, 1974.
5. Sammons, G.D., "Dynamic Calorimetric Solid Propellant Combustion Studies," AIAA Paper 69-504, 1969.
6. Strahle, W.C., et al., "Catalytic Behavior in Composite Solid Propellant Combustion," AD-770 601, 1973.
7. Kuwabara, T., "Working Mechanism of Burn Rate Catalysts (nBF) Against Composite Propellants Based on AP," INDUSTRIAL EXPLOSIVES, Vol 47 No 2, 1986.

8. Rosser, W.A., Inami, S.H. and Wise, H., "Thermal Decomposition of Ammonium Perchlorate," COMBUSTION AND FLAME, Vol 12, 1968.
9. Glaskova, A.P., "Three Possible Ways To Inhibit the Ammonium Perchlorate Combustion Process," AIAA JOURNAL, Vol 13 No 4, 1974.
10. Kubota, N. and Hirata, N., "Inhibition Reaction of LiF on the Combustion of Ammonium Perchlorate Propellants," 20th Symposium (International) on Combustion, Combustion Institute, 1984.
11. Kuwabara, T. and Kubota, N., "Burning Interruption Mechanism of Solid Propellants Containing Negative Burning Catalyst LiF," INDUSTRIAL EXPLOSIVES, Vol 42 No 6, 1981.
12. Kubota, N., "Survey of Rocket Propellants and Their Combustion Characteristics," Fundamentals of Solid-Propellant Combustion, PROGRESS IN ASTRONAUTICS AND AERONAUTICS, Vol 90, AIAA, 1984.
13. Ibid., "Burning Phenomena of Solid Propellants," INDUSTRIAL EXPLOSIVES, Vol 41 No 2-No 4, 1980, Vol 42 No 1, 1981.
14. Nagaoka, T., Shirota,K., Fukuyama, D. and Okamoto, H., "Effect of Low Temperature Ammonium Perchlorate Decomposition on the Burning Rate of Composite Propellant," Proceedings of the 10th International Symposium on Space Technology and Science, 1973.
15. Steintz, J.A., Stang, P.L. and Summerfield, M., "The Burning Mechanism of Ammonium Perchlorate-Based Composite Propellants," AEROSPACE AND MECHANICAL SCIENCE REPORT, No 830, Princeton University, 1969.

## Transonic Wind Tunnel Test To Evaluate Wing Flutter

906C3824D Tokyo BOEICHO GIJUTSU KENKYUHONBU GIHO (Japan Defense Agency Technical Research & Development Institute) in Japanese Jul 89 Technical Reports, No 5567 pp 1-11

[Article by Yukio Yoshitake, assistant director general of the First Aircraft Department of TDRI's Third Research Center; Etsuroh Sentoh, assistant director general of the Third Research Laboratory of the First Aircraft Department of TDRI's Third Research Center; and Akira Kubo and Hayao Kubota, assistant directors general of the Fourth Research Laboratory of the First Aircraft Department of TDRI's Third Research Center: "TRDI Technical Report on a Transonic Wind Tunnel Test of Wing Flutter on High Maneuvering Aircraft"]

### [Text] Summary

It is of concern, with regard to the wing flutter of aircraft in flight at transonic speeds, that there is a phenomenon called "transonic dip," which suddenly reduces the flutter speed at a Mach number.

This phenomenon is known to occur primarily on the wings of transport-class aircraft, which have high aspect ratios and comparatively thick airfoils, and it appears more strongly on supercritical airfoils than on conventional ones.

A transonic wind tunnel test was conducted to investigate what characteristics of the flutter occurred on other types of wings, those of fighter-class aircraft which have small aspect ratios and thin airfoils. The results showed that this type of wing was also affected by the "transonic dip" with the same feature for the airfoil, and that the external store under the wing clearly reduced the flutter speed through no appearance of the "transonic dip" could be obviously pointed out.

### 1. Introduction

There has been extensive research on the various kinds of wing flutter experienced by aircraft, and the flutter generating mechanism has been clarified. Compressibility affects such flutters in accordance with increases in flying speed. That is, the dynamic flutter pressure (speed) sharply decreases in the vicinity of a certain Mach number. This phenomenon is the

so-called "transonic dip," which occurs in the transonic range. It is generally said that when a supercritical airfoil (hereafter "SC airfoil") is used as an airfoil on the main wing of an aircraft, the degree of this transonic dip will be greater than when conventional airfoils are used on the main wings. Research concerning transonic dip on the main wings of many transport-class aircraft has been carried out, but there have been no comparable studies on the main wings of fighter-class aircraft.

The Third Research Center has tackled this problem. It has made a model for studying the flutter of main wings having a wing planform and a wing section suitable for fighters. It has conducted a transonic wind tunnel test of the wing flutter using this model and has confirmed the flutter characteristics both at transonic speeds and in the case where a load is mounted on the lower surface of a wing.

## 2. Symbols

$\alpha$ :	Angle of attack (degree)
$V_F$ :	Flutter speed (m/s)
$V_{FEAS}$ :	Equivalent flutter speed (m/s)
$q_F$ :	Flutter dynamic pressure (kg/m <sup>2</sup> )
$q_{FEAS}$ :	Equivalent flutter dynamic pressure (kg/m <sup>2</sup> )
$EI$ :	Flexural rigidity (kgm <sup>2</sup> )
$GJ$ :	Torsional rigidity (kgm <sup>2</sup> )

## 3. Model as a Specimen

Figure 1 shows a model (hereafter called the "main wing model") used to study the flutter of main wings having a wing planform and a wing section suitable for high maneuvering aircraft.

In other words, this main wing model has the same wing planform as that of the main wings of a wind tunnel model used for research (the second kind of A research in the Research Center) on the shape of fighters carried out by the First Research Laboratory of the First Airframe Department (now the First Research Laboratory of the Aircraft Department) in FY 1983. The main wing model is a half-mounting model reduced by about 8 percent of an assumed actual aircraft with a wingspan of about 10.5 m, an aspect ratio of about 3.14, and a leading edge sweepback angle of about 32.5 degrees. Table 1 shows the degree of similarity between the model as a specimen and hypothetical actual aircraft.

As shown below, such main wing models were manufactured every fiscal year.

Five kinds of main wing models were manufactured in FY 1983. They have NACA65A004.8 Ma airfoils, as shown in Table 2 and Figure 2, and have different rigidities.

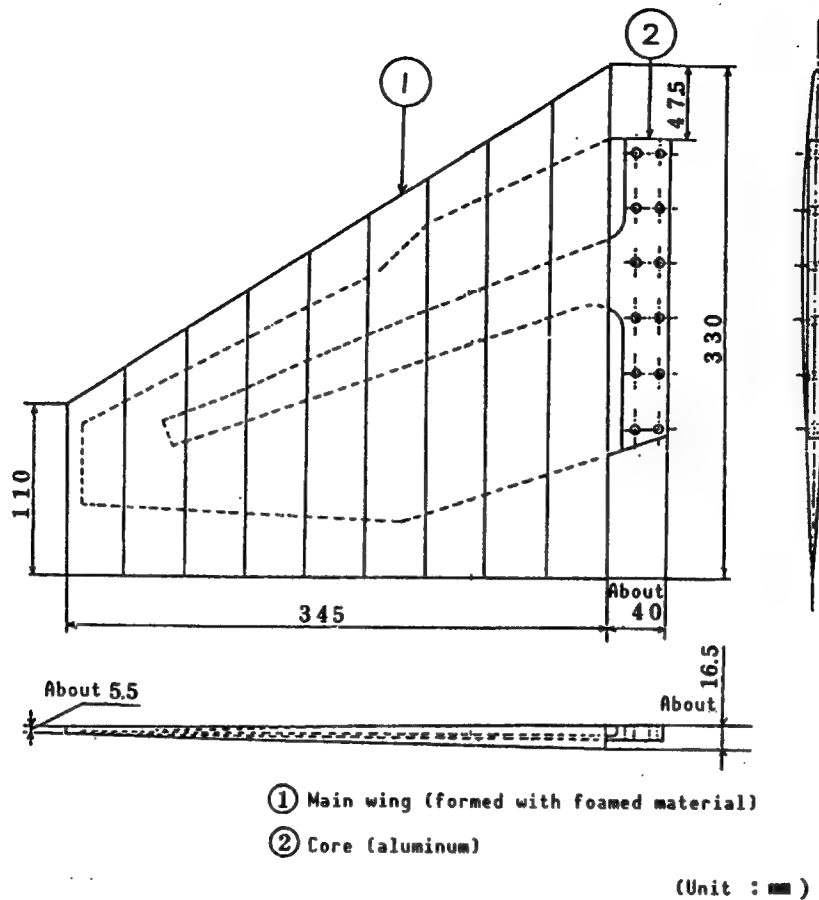


Figure 1. Model of Main Wing

Table 1. Similarity of Model as a Specimen and Hypothetical Actual Airplane

Quantity	Scale coefficient	Value by means of model as a specimen
Length	$\lambda$ ( $= 1m/la$ )	0.08
Density	$\kappa$ ( $= \rho_m/\rho_a$ )	1.01
Temperature	$\eta$ ( $= T_m/T_a$ )	0.93
Mass	$\kappa \lambda^3$	$5.17 \times 10^{-4}$
Rigidity	$\kappa \eta \lambda^4$	$3.85 \times 10^{-5}$
Vibration frequency	$\eta^{\frac{1}{2}} \lambda^{-1}$	12.05
Velocity	$\eta^{\frac{1}{2}}$	0.964
Dynamic pressure	$\kappa \eta$	0.939
Reduced frequency	1	1

The attached letter "a" represents the value for the actual airplane, and the attached letter "m" represents that for the model.

Table 2. Wind Tunnel Model Wing by Type and Coordinates

X %C	Standard airfoil		SC airfoil	
	Yu %C	Y1 %C	Yu %C	Y1 %C
0	0	0	0	0
0.25			0.4439	-0.2607
0.50	0.4999	-0.4999	0.6115	-0.3615
0.75	0.5994	-0.5994	0.7385	-0.4368
1.00			0.8442	-0.4979
1.25	0.7479	-0.7479	0.9370	-0.5498
1.50			1.0224	-0.5962
1.75			1.1019	-0.6380
2.00			1.1766	-0.6758
2.50	0.9932	-0.9932	1.3154	-0.7427
3.00			1.4418	-0.8012
3.50			1.5551	-0.8530
4.00			1.6573	-0.8996
4.50			1.7474	-0.9420
5.00	1.2869	-1.2869	1.8308	-0.9808
7.50	1.4790	-1.4790	2.1692	-1.1500
10.00	1.6425	-1.6425	2.4192	-1.2808
12.50			2.6154	-1.3846
15.00	1.8468	-1.8468	2.7769	-1.4692
17.50			2.9077	-1.5385
20.00	2.0204	-2.0204	3.0115	-1.5962
22.50			3.0962	-1.6423
25.00	2.1628	-2.1628	3.1615	-1.6769
27.50			3.2115	-1.7038
30.00	2.2764	-2.2764	3.2462	-1.7231
32.50			3.2654	-1.7346
35.00	2.3568	-2.3568	3.2692	-1.7385
37.50			3.2577	-1.7308
40.00	2.3966	-2.3966	3.2346	-1.7192
42.50			3.2000	-1.7000
45.00	2.3880	-2.3880	3.1538	-1.6731
47.50			3.0952	-1.6385
50.00	2.3308	-2.3308	3.0269	-1.5962
52.50			2.9462	-1.5423
55.00	2.2278	-2.2278	2.8538	-1.4805
57.50			2.7500	-1.4077
60.00	2.0827	-2.0827	2.6346	-1.3231
62.50			2.5115	-1.2269
65.00	1.8976	-1.8976	2.3769	-1.1192
67.50			2.2346	-1.0077
70.00	1.6771	-1.6771	2.0846	-0.8923
72.50			1.9269	-0.7769
75.00	1.4290	-1.4290	1.7615	-0.6615
77.50			1.5923	-0.5462
80.00	1.1781	-1.1781	1.4154	-0.4308
82.50			1.2346	-0.3231
85.00	0.9271	-0.9271	1.0500	-0.2269
87.50			0.8615	-0.1500
90.00	0.6762	-0.6762	0.6692	-0.1000
92.50			0.4731	-0.0808
95.00	0.4252	-0.4252	0.2692	-0.1077
97.50			0.0577	-0.1962
100.00	0.1743	-0.1743	-0.1654	-0.3615
	Leading edge radius = 0.3000		0.3300	

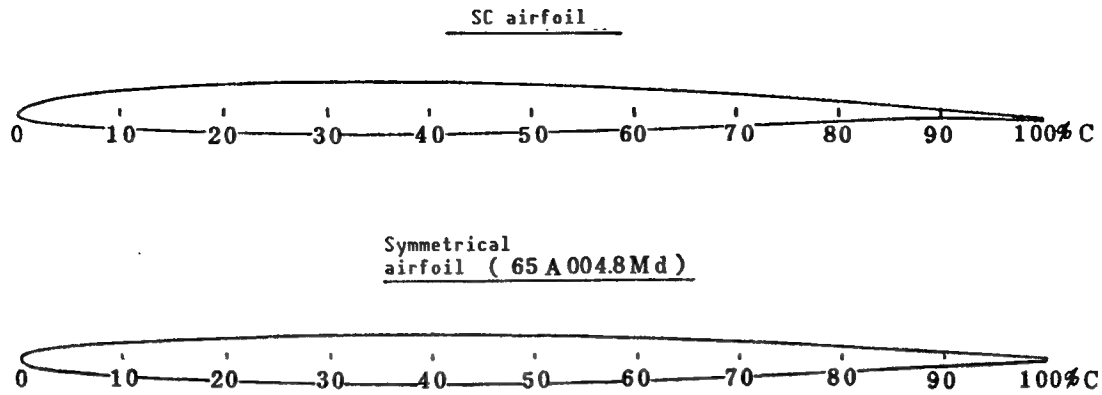


Figure 2. Airfoil of Model as a Specimen

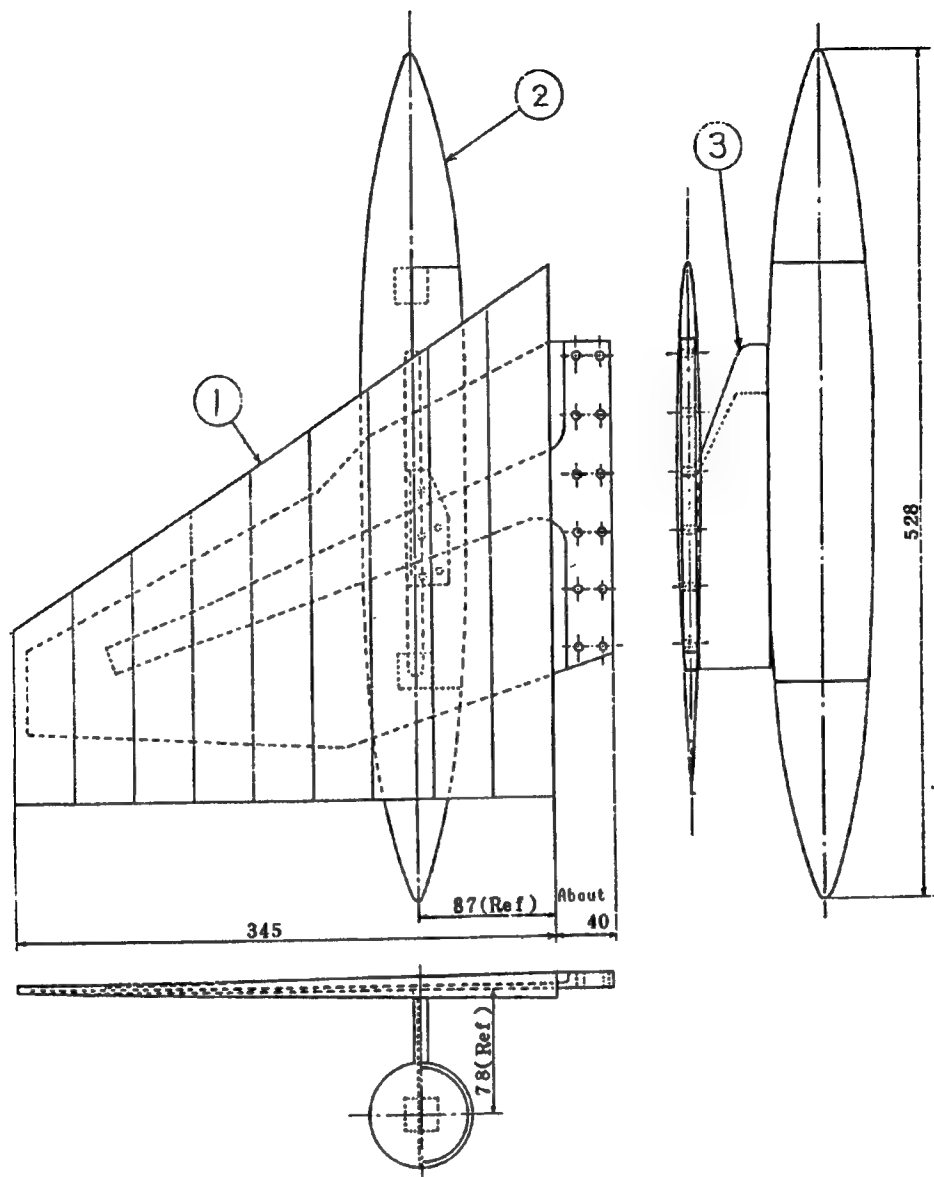
Five kinds of main wing models were manufactured in FY 1984. They have SC airfoils, as shown in Table 1 and Figure 2. Their wing thickness is almost the same as that of the main wing models manufactured in the previous fiscal year, and have different rigidities.

Three kinds of main wing models were manufactured in FY 1985. They have NACA65A004.8 Md airfoils, and have different rigidities. In addition, a similar scale model of a slip tank with a capacity of 620 gallons was made as a load mounted on the lower surface of the actual aircraft by using a pylon.

Next, an aluminum core was inserted in the center of the main wing model. The mass and rigidity distributions of the wings were represented by this aluminum core, which was wrapped and formed by a foamed material, and eight notches were made in the direction of the wing chord line of the wing span to prevent the foamed material from becoming rigid.

Also, as previously mentioned, the purpose of this test was to confirm the influence of the airfoil or the load mounted on the lower surface of the main wing or transonic flutter characteristics. Therefore, the wash-out angle and dihedral angle of the main wing model were zero degrees. This model also has an identical airfoil from the wing root and wing tip to avoid other aerodynamic influences.

In addition, Figure 3 shows a model of a slip tank as a load mounted on the lower surface of the main wing. The aluminum core was wrapped and formed with wooden materials, and the shape, distribution of mass, and moment of inertia were simulated to resemble those of an actual aircraft.



- ① Main wing
- ② Slip tank (wooden material: a heavy weight is placed inside)
- ③ Pylon (wooden material) (Unit: mm)

Figure 3. State of Slip Tank Mounted on Aircraft

#### 4. Wind Tunnel Test

The wind tunnel test was conducted in the high-speed wind tunnel facility of Fuji Heavy Industries' [FHI] Utsunomiya Manufacturing Division.

#### 4.1 Measuring Method

A strain gauge was attached to the wind tunnel wall where the aluminum core of the main wing model was attached. The output was measured with the measuring system shown in Figure 4. The power spectra of vibration were analyzed, and the vibration frequency strain and test states were investigated. This experiment made it possible to identify the generation of flutter.

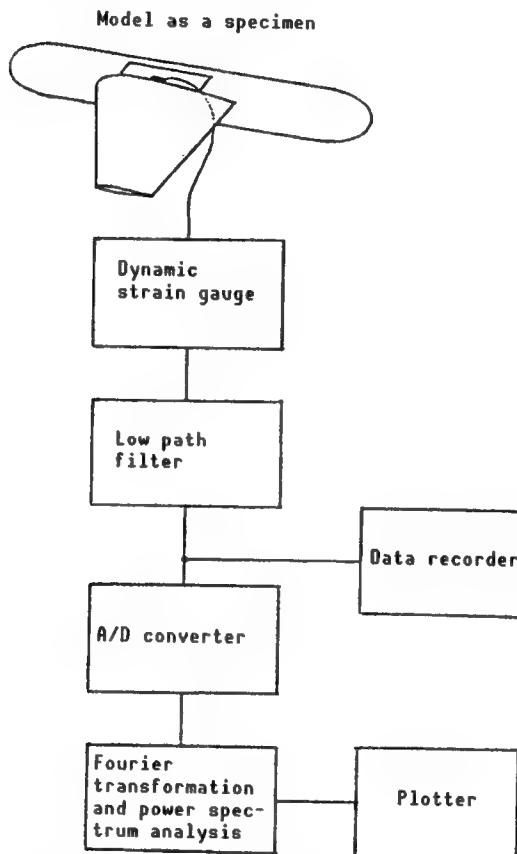


Figure 4. Block Diagram of Instrumentation System

#### 4.2 Flutter Test

The main wing model shown in Figure 3 was installed on a dummy fuselage of the wind tunnel wall, and the angle of attack was set to  $\alpha = 0^\circ$ . The flutter test was started at a Mach number lower than that at which the generation of flutter was predicted by analytical calculation, and a Mach number at which such generation began was found by gradually increasing the Mach number.

Further increases in the Mach number beyond the Mach number at which flutter appears will not generate flutter, depending on the wing shape. The flutter test was conducted at around Mach 1.0 to confirm the existence of Mach numbers for which the generation of flutter disappears by Mach 1.0. When no flutter was generated, the Mach numbers were lowered gradually to find a Mach number at which flutter appeared.

Also, the main wing model was excited by using natural disturbances in the air flow in the wind tunnel, and when the slip tank was mounted on the lower surface of the main wing, the wing tip was drawn with enamel wires.

Figure 5 [not reproduced] is a photograph of the wind tunnel test.

## 5. Results and Study

The results of the wind tunnel test are shown in Figure 6.

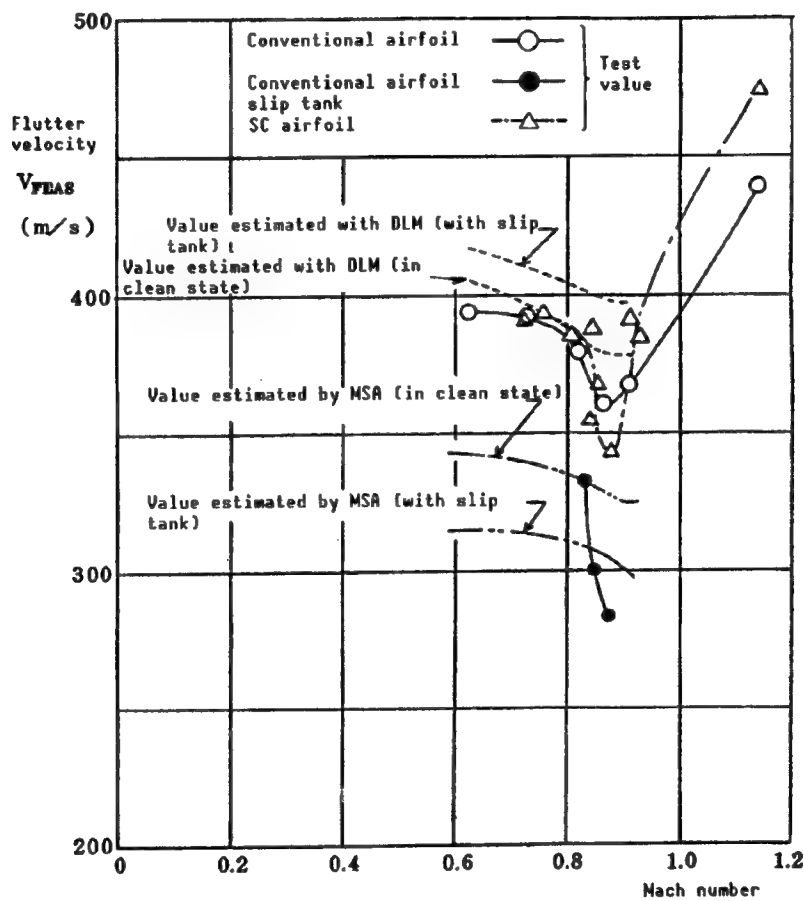


Figure 6. Relationship Between Mach Number and Flutter Velocity

Based on the test using the model shown in Figure 5 [not reproduced], it was confirmed that transonic dip (hereafter called "dip") occurred even in main wings equipped with airfoils having a small aspect ratio and a small wing thickness (about 5 percent C).

It was demonstrated that a dip of about 5 percent existed in main wings equipped with conventional airfoils in the vicinity of  $M = 0.87$ , and that a dip of about 10 percent existed in those having SC airfoils. However, both Mach numbers that show the existence of such dips seem to be almost identical.

Also, as generally mentioned, the dip in the case of the main wings equipped with SC airfoils is larger than that in the case of those having conventional airfoils. It should be noted, however, that some of the differences in the amount of dip are affected by the presence or absence of cambers. This is because, in the above case, the conventional airfoil is symmetrical, while the SC airfoil has a cambered structure as well as SC pressure distribution.

In addition, the amount of dip existing in the main wings of transport-class aircraft is said to be 20-30 percent, while for this model the value was as small as 10-15 percent. We believe that this is because the aspect ratio and wing thickness of the main wing of the model are half those of the main wing of transport-class aircraft.

In general, there is a tendency for the flutter speed to lower when a slip tank is mounted on the lower surface of the main wing as opposed to the case when no slip tank is mounted (hereafter called "clean state"). This tendency was clarified by this test, but the amount of the dip was not clarified. This is because the tendency was confirmed only at three points (mark • shown in Figure 5 [not reproduced]).

In addition, a comparison with the estimated value was made using nonsteady aerodynamic force calculated by the doublet lattice method [DLM]. The estimated flutter value (hereafter called "Value Estimated by Modified Strip Analysis [MSA]") was calculated by PASPA. A comparison between the test value and this estimated flutter value was made by using the DLM estimated flutter value calculated by the NASTRAN and by using the nonsteady aerodynamic force calculated by MSA (Figure 6).

The value estimated by the DLM accords well with the tested value in the clean state except for the vicinity of the dip. By contrast, the value estimated by using MSA is considerably lower than the test value.

There was, however, a large difference between the value estimated by using the DLM and that by using the MSA when a slip tank is mounted on the lower surface of the main wing. That is, in the case where the value was estimated by the DLM, the flutter speed was higher than that in the clean state, but in the case where the value was estimated by the MSA, the flutter speed was lower than that in the clean state. The value estimated by the DLM was higher than that for the clean state. As a result, it was possible to make the following determination.

Assuming that the rigidity is constant, the flutter speed is affected greatly by the mass and moment of inertia of loads, and by the relative position between the elastic axis, loading axis, and center of gravity, etc.

Figures 7 to 9 show the results of parametrical estimates for each case by both DLM and MSA.

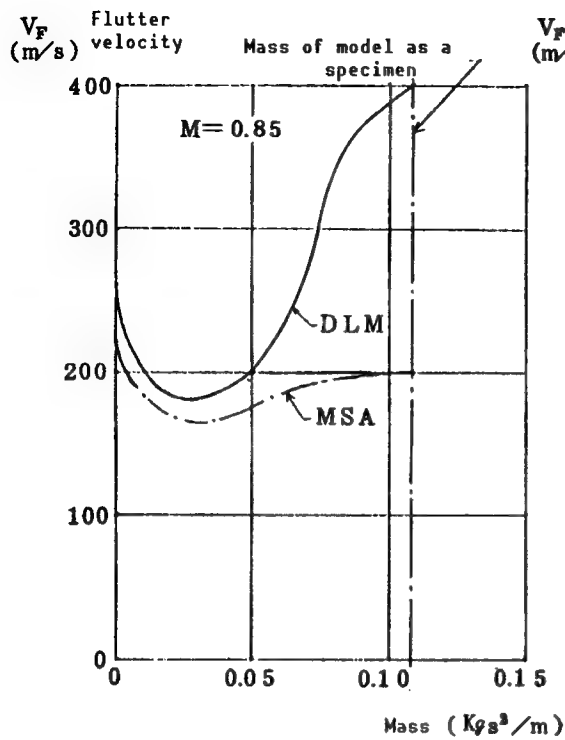


Figure 7. Influence of Mass

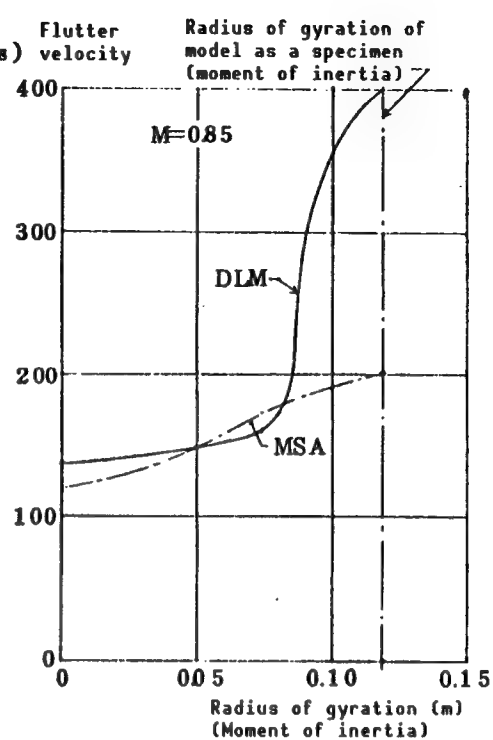


Figure 8. Influence of Moment of Inertia

(1) When the additional mass is increased gradually from 0, both DLM and MSA predict that the flutter speed will decrease, subsequently, the flutter speed will increase at a certain point, and this is where the difference between the values estimated by DLM and MSA becomes large.

(2) When the value of the moment of inertia is 0 at a constant mass, the estimated values for DLM and MSA will be close to each other, but there is a tendency for the DLM estimated value to sharply increase at a certain point.

(3) When the center of gravity of loads is at the back of the elastic axis of the main wing, there is little difference between the estimated values for DLM and MSA, but when it is moved further toward the front of the main wing, there is a tendency for the difference in estimated values to become large.

An examination of items (1), (2), and (3) indicates that the model as a specimen provides data on state that causes the difference between values estimated by using both DLM and MSA becomes unexpectedly large. It is believed that this difference may be the result of the different means by which DLM and MSA calculate nonsteady aerodynamic force, but no clear cause has yet been determined.

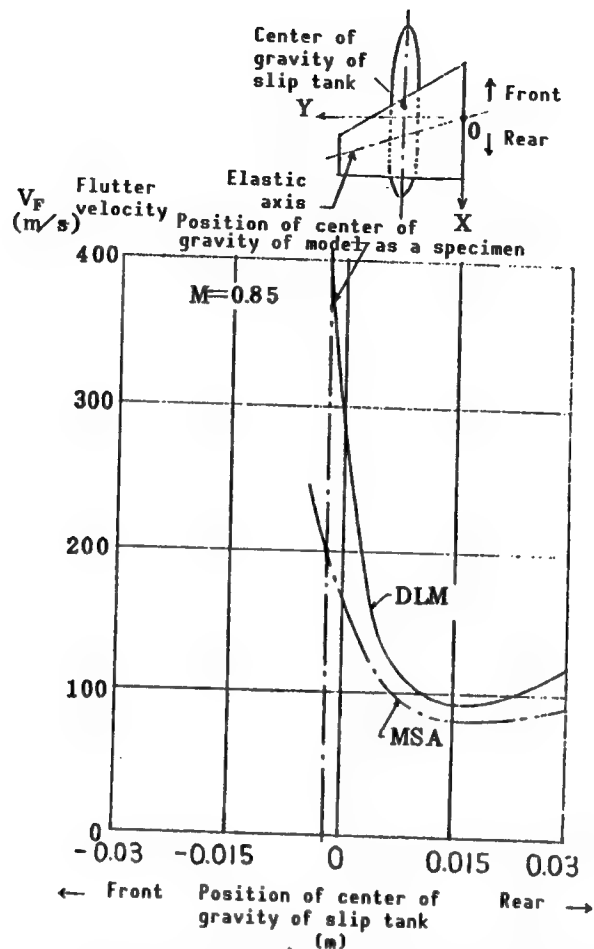


Figure 9. Influence of Position of Center of Gravity

## 6. Discussion

In this wind tunnel test, as shown in item 5.1, the generation of flutter was judged by analyzing vibration spectra and monitoring the state and the point at which the reciprocal number of strain per hertz of vibration raised to the second power sharply approaches 0.

It was confirmed that there was a tendency for this reciprocal number to approach sharply 0 in the case of the clean state. It was also possible visually to identify a sign whereby the model as a specimen causes flutter. However, when a slip tank was mounted, the reciprocal number did not approach 0. Rather, the model as a specimen gradually entered a state of permanent vibration, and there was no tendency toward divergence. Accordingly, it was difficult to recognize the generation of flutter. It is believed that this is because the wind tunnel blockage ratio is about 1 percent for the clean state and about 2 percent when the slip tank was mounted, thus air flow energies in the wind tunnel were not able to cause divergent vibrations.

Next, the model has a simple structure and is economical, but has a fixed rigidity. For more thorough testing, it would be necessary to manufacture several wings with different rigidities. Therefore, the goal of this wind tunnel testing method should be to simulate several different wings completely and aerodynamically. Accordingly, the wind tunnel testing method would be able to obtain a rough congruence between the dip produced by flutter generated from actually designed wings and wings used as the objects of research work.

The results of the wind tunnel test demonstrate that the value estimated by using DLM accords well with the test value, except for the portion of the dip in the clean state, but that is the opposite of the test value when a slip tank is mounted. The same tendency applies to the values estimated by using MSA, but it is necessary to pay attention to the fact that the value estimated by using the DLM is higher than the test value in portions which seem to be dips in the slip tank mounting state. Therefore, it would be permissible to adopt the value estimated by using MSA in the clean state in order to ensure the safety of actual aircraft against transonic flutter.

## 7. Conclusion

We have made a flutter wind tunnel test model (half-mounting model) with an airfoil and a wing platform suitable for high maneuvering aircraft, have conducted a transonic flutter wind tunnel test, and have made a comparison between flutter values estimated by using DLM and MSA, and actual test values. DLM is used to calculate nonsteady aerodynamic forces in the NASTRAN program, while MSA is used to calculate nonsteady aerodynamic forces in the PASPA program. The following conclusions were drawn from the results of the comparison.

(1) The existence of dips was confirmed. As previously noted, it was demonstrated that the magnitude of dips generated from SC airfoils was larger than that from conventional airfoils. However, the difference between conventional and SC airfoils includes the difference between symmetrical airfoils and camber ones.

The Mach number for dips generated by the test wing was in the vicinity of  $M = 0.87$ , and the magnitude of dips in the case of conventional airfoils was about 5 percent, while that in the case of SC airfoils was about 10 percent.

(2) With regard to the comparison between the test value and the estimated value, the value estimated by using DLM accorded well with the test value in the clean state, except in the vicinity of the dip. By contrast, the value obtained by using MSA was considerably lower than the test value.

The value estimated by using DLM when a slip tank was mounted was higher than that in the clean state, and the value estimated by MSA when a slip tank was mounted was lower than that in the clean state. This tendency generally accorded with the actual test value, but appeared to be higher than the test value in the portion that seemed to be a dip.

## Appendix

In order to conduct wind tunnel tests while arbitrarily changing the flutter dynamic pressure against Mach numbers, it is necessary to vary the density of the wind tunnel and to widen the range of the variable density.

Further, when wind tunnel tests are conducted by using a scale model (this is called a "completely similar model") made by completely simulating the dimensions, rigidity, and moment of inertia of the main wing of the assumed actual aircraft, in general, no flutter is generated from the main wing of the scale model. However, in order to obtain actual transonic flutter characteristic curves from this completely similar model, wind tunnel tests are conducted by using the above-mentioned variable-density wind tunnel, or a number of models to be used as specimens are manufactured to cause flutter by lowering the rigidity of the completely similar model, a Mach number which generates flutter is tentatively found, and characteristic curves are determined by converting this Mach number for application with the completely similar model. The latter method was adopted in this test. That is, assuming that the flutter dynamic pressure of the completely similar model is  $q_F$ , that of the low rigidity model is  $q_{Ftest}$ , the estimated flutter dynamic pressure of the completely similar model is  $q_{FC}$ , the estimated flutter dynamic pressure of the low rigidity model is  $q_{FLC}$ , and the Mach number at that time is  $M_F$ , the following equation can be obtained:

$$q_F = \frac{q_{FC}}{q_{FLC}} \cdot q_{Ftest}$$

The flutter dynamic pressure of the completely similar model against the Mach number  $M_F$  obtained from the test can be obtained from this equation.

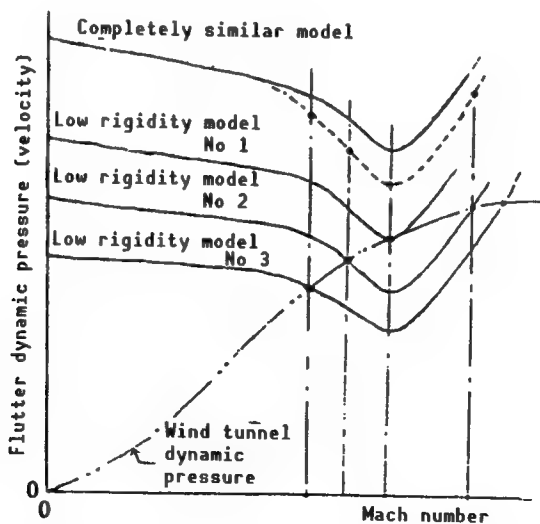


Figure. Relationship Between Rigidity, Wind Tunnel Dynamic Pressure, and Mach Number

The flutter dynamic pressure is regarded as a wind tunnel dynamic pressure, because the wind tunnel dynamic pressure can be obtained directly from the wind tunnel test. This manuscript describes the flutter speed as flutter dynamic pressure, because it seems to be easy for readers to understand the concept of flutter dynamic pressure.

#### References

1. Isogai, K., "Wing Flutter at Transonic Speed and Nonsteady Aerodynamic Force (Part 1)," THE JAPAN SOCIETY FOR AERONAUTICAL AND SPACE SCIENCES JOURNAL, Vol 29 No 324, January 1981, pp 1-13.
2. Ibid., (Part 2), Vol 29 No 326, March 1981, pp 1-10.

## **Research on Lithium-Thionyl Chloride Batteries**

906C3824E Tokyo BOEICHO GIJUTSU KENKYUHONBU GIHO (Japan Defense Agency Technical Research & Development Institute) in Japanese Jul 89 Technical Reports, No 5569 pp 1-12

[Article by Masaaki Maekawa, Kaoru Sohkura, and Tomio Hara, assistant directors general of the Third Research Laboratory of the First Communication Department of TRDI's Second Research Center; Shigenori Yonemochi, assistant director general of the Second Research Laboratory of the First Information Department of TRDI's Second Research Center; and Takahiro Ishibashi, chief director general of the First Communication Department of TRDI's Second Research Center: "Research on Lithium-Thionyl Chloride Batteries (Part 2)"]

### **[Text] Summary**

This paper describes fundamental studies and test results on high-rate dischargeable lithium-thionyl chloride batteries fabricated in 1985~1986.

#### **1. Fundamental Studies**

Temperature dependence on electric conductivity of several electrolyte solutions was studied, so that the optimum electrolyte was selected for the battery. And, furthermore, we established prospects of preventing voltage delay at initial discharge by coated negative lithium electrodes.

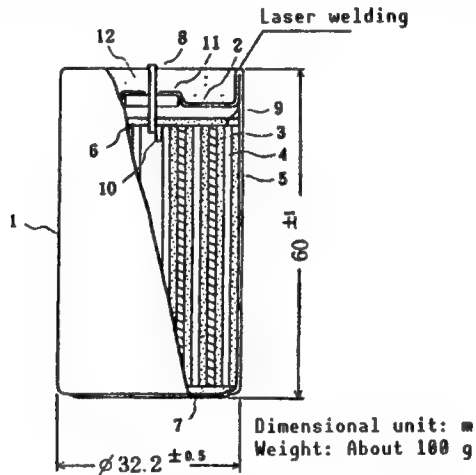
#### **2. Test Results**

Cylindrical batteries and disk-shaped batteries were fabricated. The cylindrical battery focuses increased power capacity and has spiral bobbin-shaped electrodes. The test results show the capacity of 10.3 Ah and 31.5 Wh at high current density of  $10 \text{ mA/cm}^2$ . The disk-shaped battery focused improved resistance against shock and vibration for a projection-type wave jammer. The test results show no problems under vibration of 10~500 Hz (10 G). In addition, we established that the batteries can discharge at a high current density of  $10 \text{ mA/cm}^2$  at a low temperature of  $-40^\circ\text{C}$ . The assembled batteries, four connected disk-shaped batteries in series, were fabricated and tested for confirmation of safety.

## 1. Introduction

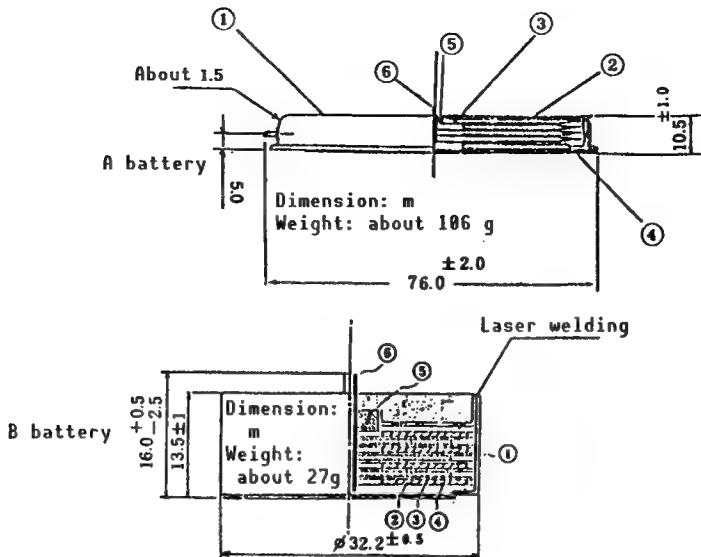
The realization of primary batteries with high capacity and highly efficient electric discharge is necessary to cope with specific power sources that will be used in the future together with the miniaturization of electronic equipment and increases in performances.

Research on lithium-thionyl chloride batteries has been underway since FY 1984. First, the possibility of highly efficient electric discharge was demonstrated<sup>1</sup> by using coin-type batteries. Next, output density was increased, and mechanical strength and safety were established as objects of this research work. With regard to the increase in output density, basic electrical characteristics were studied in FY 1985 by using a cylindrical-type (unit 1) battery with a spiral electrode structure shown as in Figure 1 and Photograph 1 [not reproduced]. With regard to mechanical strength, vibration and impact resistances were confirmed in FY 1986 by using a battery with the disk-type electrode structure shown in Figure 2 and Photograph 2 [not reproduced]. Research on the following topics was carried out during the same fiscal year:



No	Name of parts	Remarks
1	Battery storing can	SUS304
2	Battery cap	Fe-Ni alloy
3	Positive electrode	Carbon rack
4	Negative electrode	Lithium
5	Separator	Nonwoven glass fabric
6	Upper portion insulating sheet	" " "
7	Lower portion insulating sheet	" " "
8	Negative electrode terminal	" " "
9	Positive electrode tab	" " "
10	Negative electrode tab	" " "
11	Ceramic	Alumina
12	Sealer	Epoxy-resin

Figure 1. Cylindrical Lithium-Thionyl Chloride Battery



No	Name of parts	Remarks
1	Battery storing can	SUS304
2	Positive electrode	Carbon
3	Negative electrode	Lithium
4	Separator	Nonwoven glass fabric
5	Insulating ceramic	Alumina
6	Negative electrode terminal	Nickel

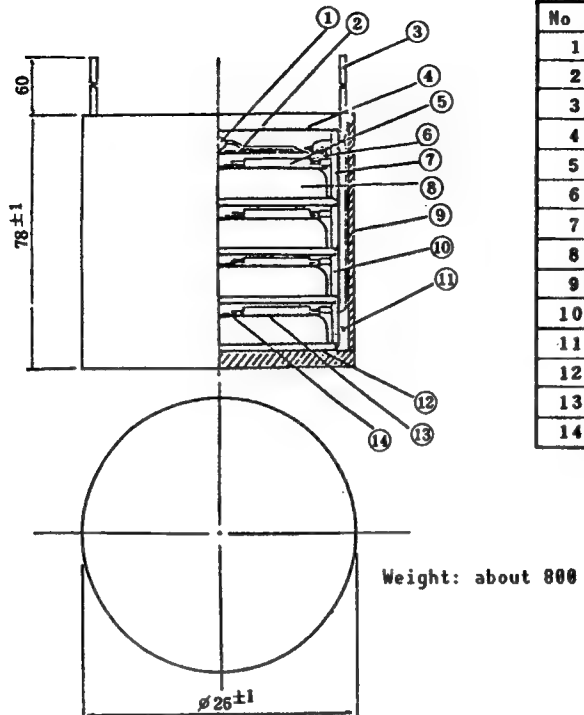
Figure 2. Disk-Type Lithium-Thionyl Chloride Battery

1) a voltage delay phenomenon generated at the initial period of electric discharge, and 2) methods of preventing this phenomenon. A demonstration test of the safety was conducted in FY 1987 by using a 12-V practical battery like that shown in Figure 3 and Photograph 3 [not reproduced]. This battery is an aggregation of unit cell batteries. This report will hereunder describe the above research processes and results.

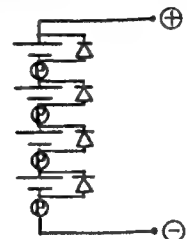
## 2. Experiment and Results

### 2.1 Clarification of Elemental Technologies

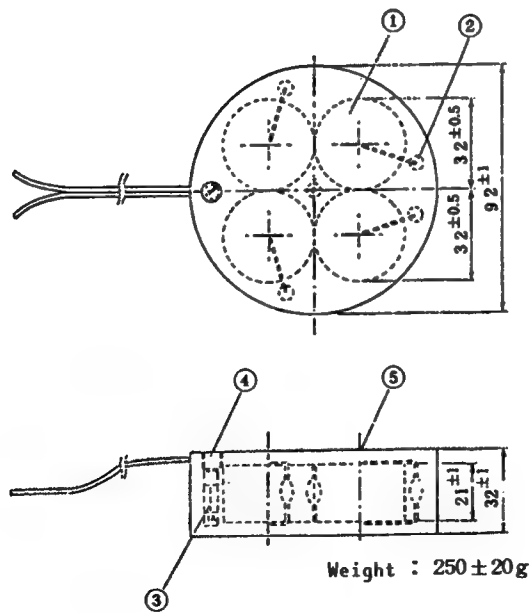
(1) Values for resistance against temperature were measured and electrical conductivity was determined by calculating the concentration of electrolyte (solvent:  $\text{SOCl}_2$  and solute:  $\text{LiAlCl}_4$ ) as a parameter. The results are shown in Figure 4.



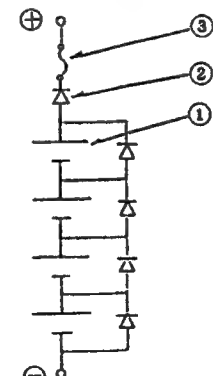
No	Item	Amount	
1	Protection diode	4	
2	Print baseplate	1	FRP
3	Lead wire (red and blue)	2	25L
4	FRP insulating plate A	5	FRP
5	Polyswitch	4	
6		1	Pair brain
7	Battery supporting frame A	1	Vinyl chloride resin
8	Unit battery	4	
9	Case	1	- - -
10	Battery supporting frame B	3	- - -
11	Silicon resin	200g	
12		8cm	- - -
13	FRP insulating plate B	4	FRP
14	Nickel tab	8	Nickel



Outline and dimension of A battery



No	Item	Amount	
1	Electric wire	4	2.5Ah(50mA)
2	Diode	5	UOSB (Hitachi, Ltd.)
3	Fuse	1	0.5A tube fuse
4	Fuse stopper	1	Screw fixing system
5	Electric wire	1	



Outline and dimension of B battery

Figure 3. Aggregated Lithium-Thionyl Chloride Battery

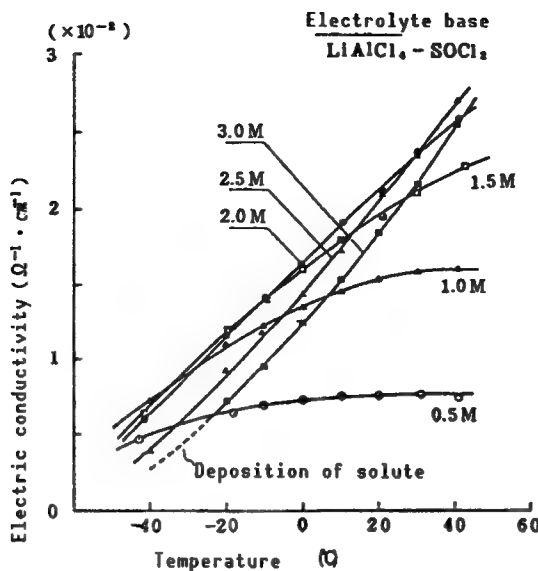


Figure 4. Temperature Dependency of Electric Conductivity

(2) Prevention of generation of voltage delay phenomenon

The voltage delay phenomenon means that a threshold voltage delay or voltage drop is generated during the initial period of electric discharge by an LiCl coat formed on the Li surface of the negative electrode. This phenomenon occurs primarily in the following cases:

- i) The storage period is long.
- ii) The storage temperature is high.
- iii) The discharge current density is large
- iv) The ambient temperature is low.

The following can be cited as methods of preventing this phenomenon:

- a) The Li surface of the negative electrode is coated so it will not form an LiCl coat.
- b) An electrolyte based on  $\text{Li}_2\text{O} + \text{AlCl}_3$  is used.

As a result of studying these two methods, it was recognized that both methods improve the effectiveness of the batteries.

(Coating Method)

Two kinds of batteries were trial manufactured as specimens by using cyanoacrylate polymer [CA] and polyvinyl chloride [PVC].

Figure 5 shows the initial voltage characteristics for the electric discharge of two batteries in which the Li pole of one was not treated while the other was coated with CA. Both batteries were stored at a temperature of 45°C for 3 days and then were discharged electrically at room temperature at a current density of  $10 \text{ mA/cm}^2$ . The voltage of the battery coated with Ca rose in a

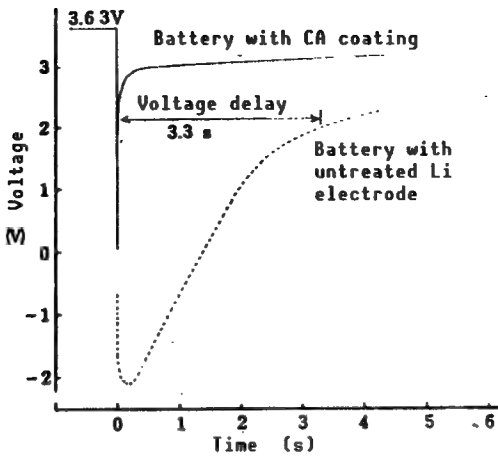


Figure 5. Initial Voltage Characteristics of Electric Discharge

moment of electric discharge, but that in which Li pole was not treated had a voltage delay time of 3.3 seconds until the voltage recovered to 2 V.

#### [Electrolyte Method]

It is necessary to study this method carefully, because there are problems in the discharge voltage and discharge duration.

### 2.2 Experiment Using Test Batteries

#### 2.2.1 Electric Discharge of Cylindrical-Type Battery

A cylindrical-type battery whose electrode has a spiral bobbin structure was adopted to make it possible to increase packaging density. Figure 6 and Table 1 show sampling results for two kinds of batteries having positive electrode carbon plates with a thickness of 0.4 and 0.7 mm. These batteries were continuously and electrically discharged at an ambient temperature of 20°C and at a current density of 10 mA/cm<sup>2</sup>.

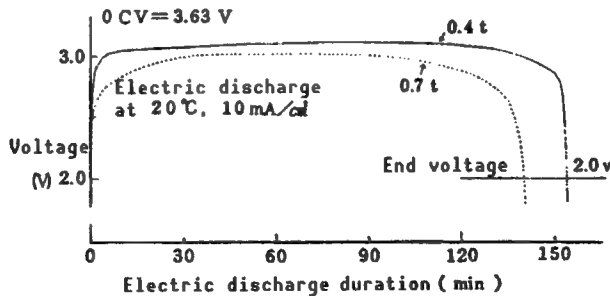


Figure 6. Electric Discharge Characteristics of

Table 2 shows the electrode dimension and area of the two batteries.

Table 1. Electric Discharge Characteristics of Cylindrical Lithium-Thionyl Chloride Battery

Thickness of positive electrode carbon plate (mm)	0.4	0.7
Electric discharge current value (A)	4.0	3.5
Electric discharge duration (hours and minutes)	2 h 34 m	2 h 20 m
Average voltage (V)	3.065	2.915
Capacity	Ah	10.27
	Wh	31.5
Energy density	Wh/kg	312
	Wh/L	631
		484

Table 2. Dimension and Area of Electrode

Thickness of positive electrode carbon plate	Dimension and area of electrode
0.4 mm	500 mm x 40 mm = 200 cm <sup>2</sup>
0.7 mm	430 mm x 40 mm = 172 cm <sup>2</sup>

### 2.2.2 Electric Discharge From Disk-Type Batteries

Two kinds of batteries were test manufactured taking into consideration resistance to vibration and impact. They were equipped with disk-like electrodes. One (A battery) had an effective electrode area of 215 cm<sup>2</sup>, while the other (B battery) had 29 cm<sup>2</sup>. In addition, two kinds of batteries were made to prevent the generation of voltage delay phenomena. The Li pole of one was coated with PVC, while that of the other was coated with CA.

#### (1) Load current characteristics

Figure 7 and Table 3 show the results of setting the ambient temperature of the A battery at 20°C and continuously and electrically discharging this battery at load currents of 0.2, 0.5, 1, 2, and 3 A. In the same manner, Figure 8 and Table 4 show the results of continuously and electrically discharging the B batteries at load currents of 75, 300, and 600 mA.

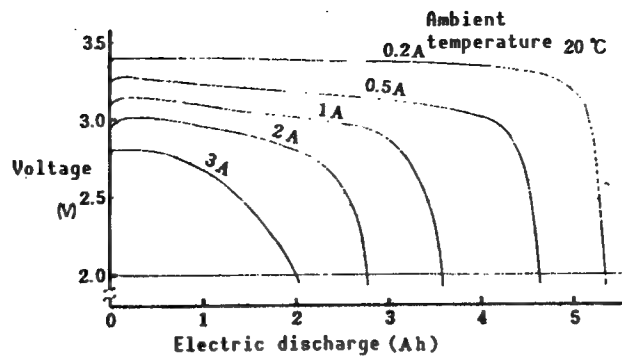


Figure 7. Load Current Characteristics of A Battery

Table 3. Electric Discharge Characteristics of A Battery

Electric discharge current value (A)	Electric discharge duration (h, min)	Average voltage (V)	Capacity	
			Ah	Wh
0.2	26 h 44 min	3.325	5.35	17.79
0.5	9 h 16 min	3.114	4.63	14.42
1	3 h 35 min	2.972	3.58	10.64
2	1 h 23 min	2.843	2.77	7.88
3	40 min	2.575	2.00	5.15

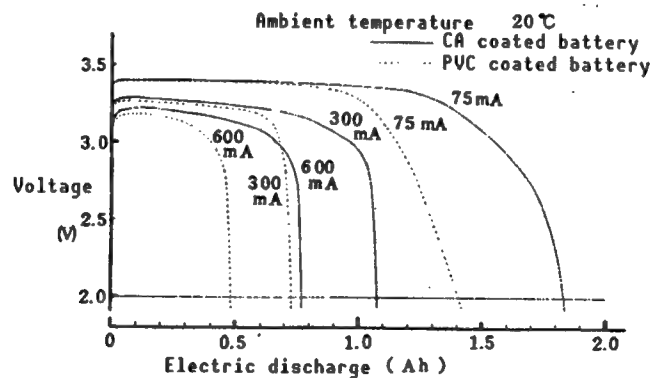


Figure 8. Load Current Characteristics of B Battery

Table 4. Electric Discharge Characteristics of B Battery

Li electrode treating agent	Electric discharge current value (mA)	Electric discharge duration (h, min)	Average voltage (V)	Capacity	
				Ah	Wh
CA	75	24 h 27 min	3.250	1.83	5.95
	300	3 h 35 min	3.178	1.075	3.42
	600	1 h 17 min	3.112	0.77	2.40
PVC	75	18 h 45 min	3.207	1.406	4.51
	300	2 h 26 min	3.222	0.73	2.35
	600	48 min	3.077	0.48	1.48

## (2) Temperature Characteristics

Figures 9 and 10 and Table 5 show the results of setting the ambient temperature of the A battery at  $-40^{\circ}\text{C}$ ,  $-20^{\circ}\text{C}$ ,  $0^{\circ}\text{C}$ ,  $20^{\circ}\text{C}$ ,  $40^{\circ}\text{C}$ , and  $60^{\circ}\text{C}$  and continuously and electrically discharging these batteries at constant currents of 0.5 and 2 A. In the same manner, Figure 11 and Table 6 show the results of testing the B batteries.

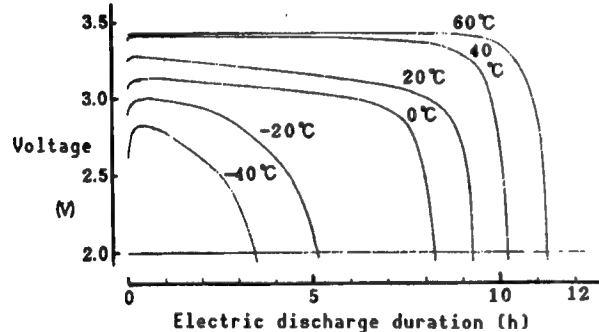


Figure 9. Temperature Characteristics of A Battery (Electric discharge at constant current of 0.5 A)

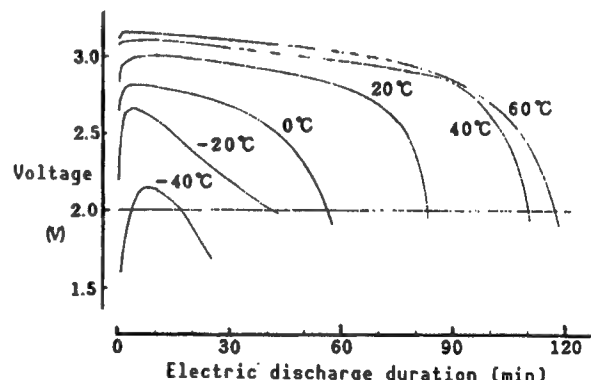


Figure 10. Temperature Characteristics of A Battery (Electric discharge at constant current of 2 A)

Table 5. Temperature Characteristics of A Battery

Battery environmental temperature (°C)		60	40	20	0	-20	-40
Electric discharge at 0.5 A	Electric discharge duration (h, min)	11 h, 15 min	10 h, 12 min	9 h, 16 min	8 h, 15 min	5 h, 8 min	3 h, 25 min
	Average voltage (V)	3.379	3.348	3.114	3.007	2.766	2.598
	Capacity	Ah	5.63	5.10	4.63	4.13	2.57
Electric discharge at 2 A	Electric discharge duration (h, min)	1 h, 57 min	1 h, 50 min	1 hr, 23 min	56 min	41 min	13 min
	Average voltage (V)	2.937	2.926	2.843	2.620	2.359	2.098
	Capacity	Ah	3.90	3.67	2.77	1.87	1.37
	Capacity	Wh	11.5	10.7	7.88	4.90	3.23
	Capacity	Wh					0.90

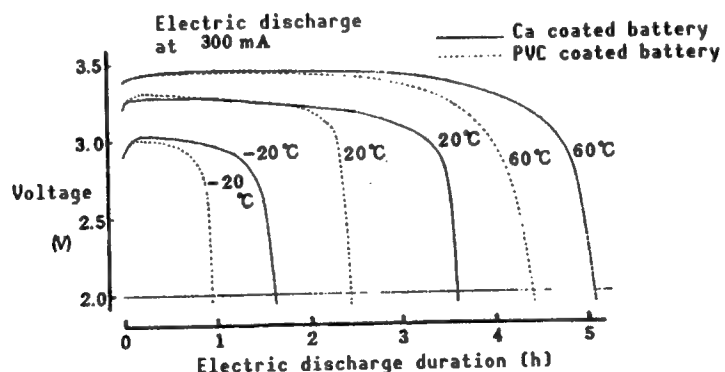


Figure 11. Temperature Characteristics of B Battery  
(Electric discharge at constant current of 300 mA)

Table 6. Temperature Characteristics of B Battery (Electric discharge at 300 mA)

Battery environmental temperature (°C)		60	40	-20
Li electrode Ca coating	Electric discharge duration (h, min)	5 h, 4 min	3 h, 35 min	1 h, 37 min
	Average voltage (V)	3.328	3.178	2.921
	Capacity	Ah 1.52	1.07	0.48
Li electrode PVC coating	Electric discharge duration (h, min)	4 h, 24 min	2 h, 26 min	56 min
	Average voltage (V)	3.300	3.222	2.925
	Capacity	Ah 1.32	0.73	0.28
		Wh 5.06	3.42	1.42
	Electric discharge duration (h, min)	4 h, 24 min	2 h, 26 min	56 min
	Average voltage (V)	3.300	3.222	2.925
	Capacity	Ah 1.32	0.73	0.28
		Wh 4.36	2.35	0.85

### (3) Storage Characteristics

Figures 12 and 13 and Table 7 show the results of storing A batteries at room temperature for 6 months at a temperature of 45°C for 3 months, setting the ambient temperature at 20°C and continuously and electrically discharging the batteries at constant currents of 0.5 and 2 A.

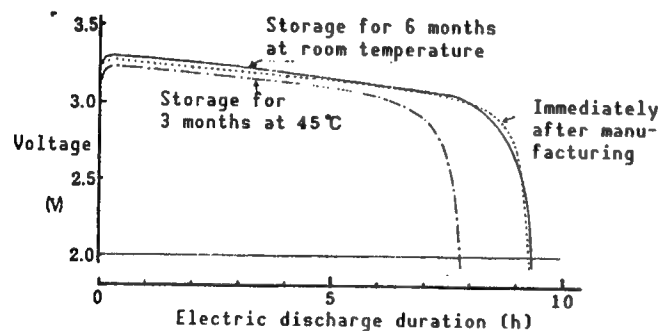


Figure 12. Storage Characteristics of A Battery (Electric discharge at constant current of 0.5 A)

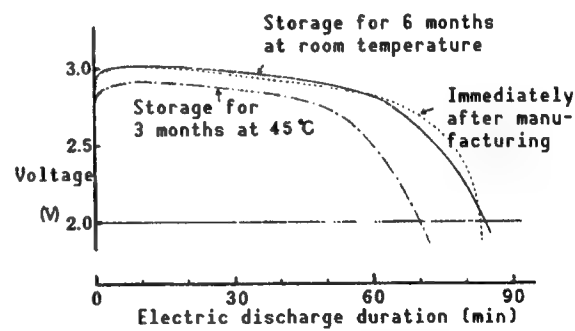


Figure 13. Storage Characteristics of A Battery (Electric discharge at constant current of 2 A)

Table 7. Storage Characteristics of A Battery

Storage condition environmental temperature 20°C		Immediately after manufacturing	6 months at room temperatures	3 months at 45°C
Elec-tric dis-charge at 0.5 A	Electric discharge duration (h, min)	9 h, 16 min	9 h, 20 min	7 h, 47 min
	Average voltage (V)	3.114	3.123	3.080
	Capacity	Ah	4.63	4.67
		Wh	14.4	14.6
Elec-tric dis-charge at 2 A	Electric discharge duration (h, min)	1 h, 23 min	1 h, 24 min	1 h, 10 min
	Average voltage (V)	2.843	2.834	2.743
	Capacity	Ah	2.77	2.80
		Wh	7.88	7.94
				6.39

#### (4) Vibration and Impact Characteristics

Table 9 shows the states (appearance, shape, open-circuit voltage, etc.) of the A battery obtained by impressing this battery under the vibration and impact conditions shown in Table 8. After impression, the battery was electrically discharging at a constant current of 2 A. Figure 14 shows the results of this discharge test.

Table 8.1 Conditions of Vibration

Division	I	II
Frequency	10-55 Hz	55-500 Hz
Acceleration	—	10 G
Total amplitude	2.03 mm	—
Sweep rate	1 Hz/min	15 min/cycle
Direction	X, Y, Z (three axes)	X, Y, Z (three axes)
Time	90 min/axis	30 min/axis

Table 8.2 Conditions of Impact

Acceleration	Time	Waveform	Direction	Number of times
100 G	$6 \times 10^{-3}$ s	Sine half wave	X, Y, Z (three axes)	3 times/axis

Table 9. States Before and After Vibration and Impact Tests

Division	Appearance and shape	Weight	Open circuit voltage	Internal resistance
Before impression	No abnormality	108.8 g	3.65 V	0.32 Ω
After impression	No abnormality	108.8 g	3.65 V	0.59 Ω

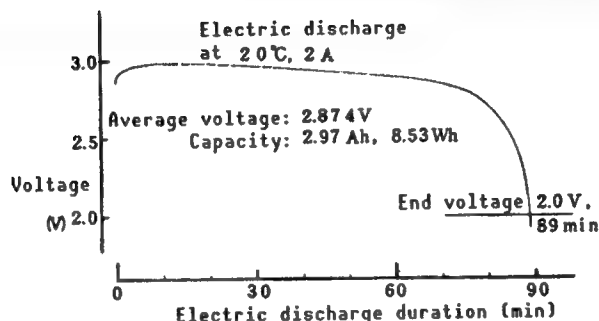


Figure 14. Electric Discharge Characteristics After Vibration and Impact Tests

### 2.2.3 Safety of Aggregated Batteries

Two kinds (A and B) of four disk-type batteries were tentatively connected in series to form a group of batteries. The safety of the batteries in this group was studied by subjecting them to the usual discharge tests together with an over-discharge test and a short-circuit test.

#### (1) Discharge Characteristics

Figure 15 and Table 10 show the constant current discharge characteristics of the group of batteries at an ambient temperature of 20°C and at a current density of about 10 mA/cm<sup>2</sup>.

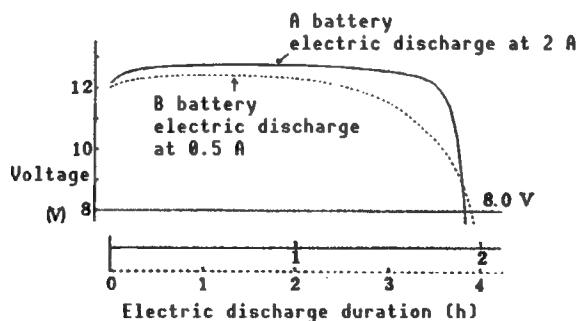


Figure 15. Electric Discharge Characteristics of Aggregated Batteries

Table 10. Electric Discharge Characteristics of Aggregated Batteries

A battery: Electric discharge at 2 A	Electric discharge duration (h, min)		1 h, 55 min
	Average voltage (V)		12.50
	Capacity	Ah	3.83
B battery: Electric discharge at 0.5 A		Wh	47.9
Electric discharge duration (h, min)		3 h, 54 min	
Average voltage (V)		11.77	
B battery: Electric discharge at 0.5 A	Capacity	Ah	1.95
		Wh	23.0

## (2) Over-Discharge Characteristics

Over-discharge refers to a state in which, even if the terminal voltage is less than the specified end voltage, the discharge will continue. A pole change-preventing diode was connected in parallel to each unit battery to prevent any abnormalities, even if this state continues. In addition, if polyswitches are connected in series to a large-capacity A battery, the resistance of these polyswitches will increase in accordance with the sharp temperature rise at the end period of discharge, and the current will be cut off. By this means, it was possible to confirm the safety of the group of batteries. Also, the polyswitch has a conductive plastic element with a temperature coefficient for which resistance is positive. No abnormalities in the appearance or shape of this battery were detected.

Figure 16 shows the over-discharge characteristics of an aggregate group of B batteries.

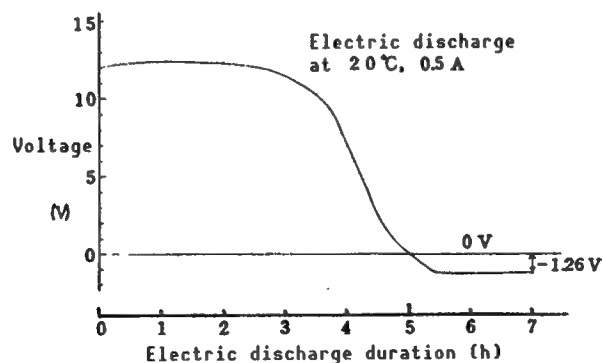


Figure 16. Electric Over-Discharge Characteristics of Aggregated B Batteries

### (3) Short-Circuit Test Characteristics

When an A battery with a large capacity shorts an external circuit, over-current will flow sharply and caloric power will increase. If this state continues, the safety valve of this battery will activate itself, but in the worst case, the battery may explode. Polyswitches were connected in series with the circuit to prevent over-current from being generated in this circuit. The polyswitch is a self-return device that protects the element used to prevent over-current and excessive temperature rise from being generated in the surface of each unit battery. Rapid blowout fuses were connected in series to the B batteries and the safe operation of these batteries was checked.

Figure 17 shows a short-circuit test circuit for the A battery. The knife switch shown in this figure was closed and the battery voltage, current, and surface temperature, together with the surface temperature of the polyswitch were measured with a recorder.

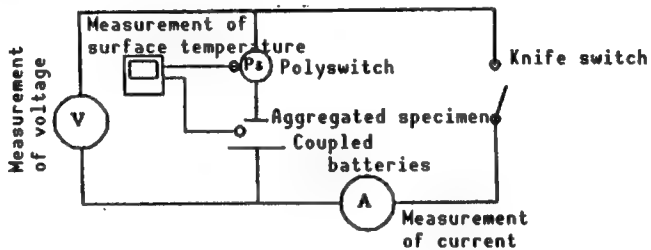


Figure 17. Short-Circuit Test Circuit

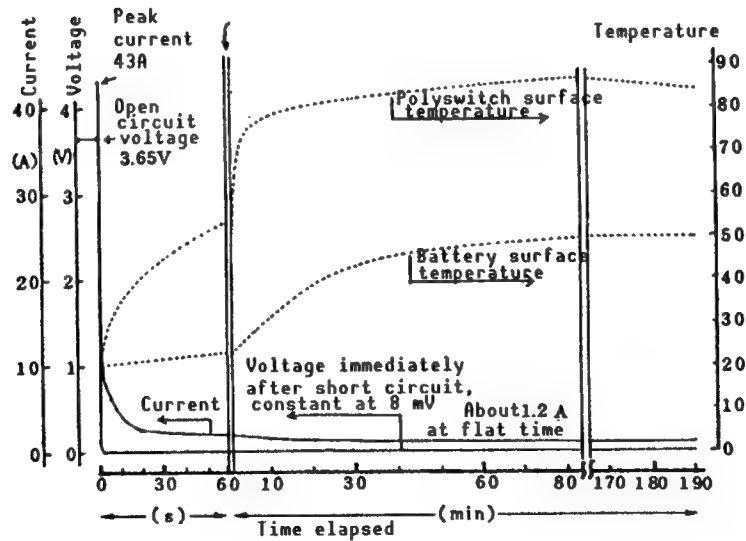


Figure 18. Short-Circuit Test of Aggregated A Batteries

Figure 18 shows the results of a short-circuit test of the A battery. The open-circuit voltage and peak current were 3.65 V and 43 A, respectively, but immediately the voltage and current dropped to 8 mV and about 1.2 A,

respectively. It was confirmed that the safety device worked satisfactorily, because the polyswitch surface temperature and the battery surface temperature were about 85°C and 50°C, respectively.

The safety of the B batteries was confirmed by the fact that the fuses blew almost instantly during short-circuit tests of these batteries.

### 3. Discussion

#### 3.1 Cylindrical Battery

A feature of cylindrical-type batteries with a spiral bobbin electrode structure is that it is possible to widen the electrode area. Therefore, these batteries are most advantageous in terms of performance than any other batteries. However, the surface temperature of some batteries was 60-70°C at the end period of discharge. This is because the radiating surface is smaller than the discharge current value. Accordingly, in order to put such cylindrical batteries to practical use as high efficient discharge batteries, their safety must be ensured, given the dispersion structure of heat generated by an aggregation of batteries and because there is a possibility of thermorunaway being caused by the thionyl chloride, which has a boiling point of 77°C.

Table 11 shows a comparison of the output densities for batteries with various structures.

Table 11. Comparison Among Various Battery Structures in Respect of Output Density

(Current density, 10 mA/cm<sup>2</sup>)

Battery structure			Electric discharge current value	Average voltage	Average output	Output density		
						W/kg	W/L	
Cylindrical battery	Thickness of carbon plate	0.4mm	4 A	3.065 V	12.3 W	122	246	
		0.7mm	3.5 A	2.915 V	10.2 W	99	207	
Coin type battery			60 mA	3.133 V	188 mW	14	31	
Disk type battery	A battery		2 A	2.843 V	5.686 W	54	123	
	B battery	Coating	CA	300 mA	3.178 V	953.4mW	35	78
			PVC	300 mA	3.222 V	966.6mW	36	81

### 3.2 Disk Type Battery

#### 3.2.1 A Battery

##### (1) Load Current Characteristics

The results depicted in Figure 7 and Figure 3, show that the flatness of the discharge voltage deteriorated at a current of 3 A (current density: 15 mA/cm<sup>2</sup>) as compared with that at ZA discharge. The Wh capacity was 65 percent. Figure 19 also shows the relationship between discharge current and battery capacity.

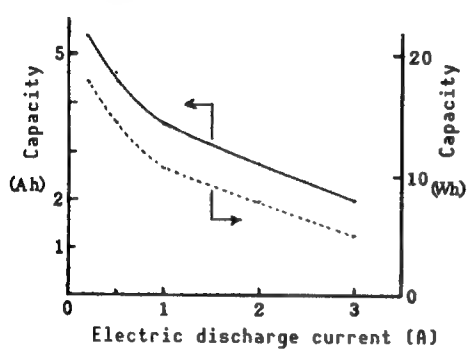


Figure 19. Relationship Between Capacity and Electric Discharge Current

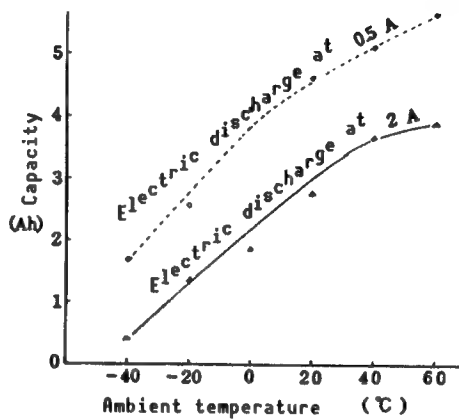


Figure 20. Relationship Between Capacity and Ambient Temperature

##### (2) Temperature Characteristics

The results depicted in Figures 9 and 10 and Table 5 indicate that electric discharge at a current of 0.5 A clearly affected the electric discharge duration at temperatures of -20°C or less, but electric discharge was possible at temperatures as low as -40°C.

The voltage delay time was more than 3 minutes at an electric discharge of 2 A and at a temperature of -40°C. It was possible to obtain electric discharge under these conditions, but in order to achieve a highly efficient electric discharge at cryogenic temperatures, it will be necessary to explore ways to improve electrolytes, coating agents for lithium pole surfaces, etc.

Figure 20 also shows the relationship between ambient temperature and battery capacity (Ah).

##### (3) Storage Characteristics

The results depicted in Figures 12 and 13 and Table 7 indicate that battery capacity was not affected by having been stored for 6 months at room temperature. But battery capacity after storage for 3 months at a temperature of 45°C was reduced by about 20 percent.

#### (4) Vibration and Impact Characteristics

No abnormalities were detected in the results obtained from tests conducted under the vibration and impact conditions shown in Tables 8.1 and 8.2. Further, as can be seen from Table 9, the results obtained from subsequent electric discharge at 2 A did not show any effects from vibration and impact within the normal dispersion of battery performance.

#### 3.2.2 B Batteries

Figures 8 and 11 and Tables 4 and 6 show the load current characteristics and temperature characteristics of two kinds of batteries whose negative electrode Li pole surfaces were coated with PVC and CA. The results indicate that the battery whose negative electrode Li pole surface was coated with CA generally proved superior to that coated with PVC in terms of performance.

#### 3.3 Aggregate Group of Batteries

Safety was checked by conducting over-current and short-circuit tests. As a result, it was confirmed that there was neither any danger of explosion nor any abnormalities in the batteries, thanks to the protection elements incorporated in an aggregate group of batteries.

#### 4. Conclusion

Research on lithium-thionyl chloride batteries as primary batteries for highly efficient electric discharge has been conducted since FY 1984. During this period, these kinds of batteries for electric discharge with a low degree of efficiency have been on the market as power sources for the backup of integrated circuit memories, etc., and technologies for the safety of these batteries have been established. In the future, however, such batteries must be further studied and improved to overcome the voltage delay phenomena generated during the initial stage of electric discharge at cryogenic temperatures and to solve the problem of how to preserve highly efficient at high temperatures after the batteries have been stored for extended periods.

#### References

1. Maekawa, M., et al., "Research on Lithium-Thionyl Chloride Batteries (Part 1)," TRDI's TECHNICAL REPORT (in-house) May 1986, p 631.

## Characteristics of New Lens Antenna

906C3824F Tokyo BOEICHO GLJUTSU KENKYUHONBU GIHO (Japan Defense Agency Technical Research & Development Institute) in Japanese Jul 89 Technical Reports, No 5573 pp 1-6

[Article by Osamu Hashimoto, assistant director general of the Fifth Research Laboratory of the Second Radio Wave Department of TRDI's Second Research Center; and Masanori Shinriki and Fujio Shimano, assistant directors general of the Second Research Laboratory of the Second Radio Wave Department of TRDI's Second Research Center: "An Experimental Study of a Dielectric Sphere Antenna"]

### [Text] Summary

We manufactured a spherical lens antenna using a circular planar spiral antenna covering 8-18 GHz range and measured its characteristics.

As the result of our measurement, the antenna gain and beam width were determined to be about 14~24 dBi and 5~12 degrees in a range from 8~18 GHz. The angular error of arrival was 0.3~1.2°rms, based on model analysis using the measured antenna pattern.

The results of our measurement and model analysis are expected to be applied to the design of a lens antenna using electronic support measures.

### 1. Introduction

This report describes the contents of what was primarily an experimental study of a lens antenna equipped with a receiving dielectric sphere (hereafter called the "lens"). This antenna has been used in two-dimensional angle measuring work as part of the "Research on ESM" program conducted by TRDI's Second Research Center in FY 1988.

There is an extensive body of research on using lens antennas as optical scanning antennas. A lens antenna is designed so that a focal point is established on the sphere or its external portion by using a spherical refracting substance. Therefore, wave fronts incident from arbitrary directions converge at this focal point.<sup>1</sup>

Such antennas possess the following features:

- (1) A number of equivalent phases can be formed in a direction symmetrical to the lens sphere by arranging a number of element antennas on or along the lens sphere; these can be used as a number of beam antennas.
- (2) When a number of element antennas are arranged on the surface of the sphere or along its external portion, the converging area will virtually become two-dimensional hemisphere as long as incoming waves are not blocked by element antennas arranged on the opposite side of the sphere.
- (3) The frequency band is wide; this is because, in general, it is possible to use a dielectric sphere where the change in the dielectric constant is less than that of the frequency.

When these features are incorporated into this antenna, which has a simple structure, the antenna appears to be promising as a wide band receiving antenna for two-dimensional angle measuring work.<sup>2</sup>

Previously, the author has theoretically studied the wide band properties and angle measuring properties of the antenna.<sup>3</sup> In this research project, a lens antenna was made by installing a spiral antenna (8-18 GHz) as a wide band element antenna on a lens with a diameter of 177 mm. The wide band properties and angle measuring properties of this lens antenna were studied experimentally, and the angle measuring accuracy was simulated by using a result obtained from this study.

As a result, it was confirmed that this lens antenna possessed a wide band property with a gain of 14-24 dBi in the X band and Ku band (8-18 GHz). It was also confirmed experimentally that the half beam width of the antenna pattern was as sharp as 5 to about 12 degrees and the first side lobe was about 17 dB as compared with the maximum gain of the main lobe. In addition, it was determined that it is possible to carry out angle measuring work with a high degree of accuracy, because when the angle measuring accuracy was simulated by using the above result, the angle measuring error was 0.3-1.2°rms. We will hereunder describe the details of our research project.

## 2. Antenna

Photographs 1 and 2 [not reproduced] show the appearance of the lens antenna made for this research project and that of the spiral antenna used therein. As shown in these photographs, the lens used in our research project had a diameter of 177 mm. Its refractive index is distributed almost in accordance with Luneberg's solution, shown as a broken line in Figure 1, by setting a radius standardized from the center of the sphere on the transverse axis shown in the figure and setting the refractive index on the ordinate shown in the figure, and by approximately constituting the lens with seven layers as an indication of the distribution of the refractive index.<sup>4</sup> Also, as can be seen from this distribution of the refractive index, the focal point is constructed

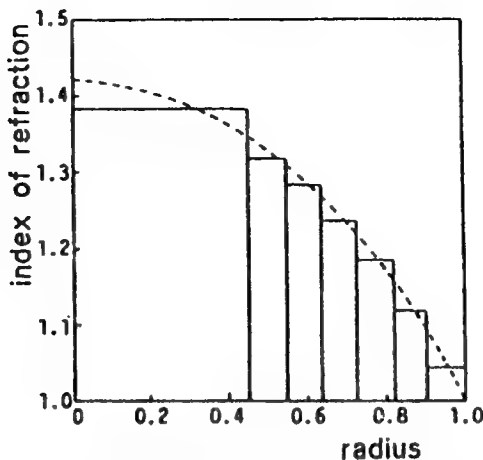


Figure 1. Distribution of Refractive Index of Lens

so that it is positioned almost on the surface of the sphere. The materials were made by mixing Styrofoam with very thin aluminum wires to control the refractive index and to minimize loss.

The antenna was constituted by installing a wide band spiral antenna with a diameter of 20 mm as an element antenna (shown in Photograph 2 [not reproduced]) on this lens so that it is possible continuously to move this spiral antenna from the surface of the sphere in the direction of the radius. Appendix A-1 shows the results of measuring the gain of the element antenna used in the research project. These results indicate that the band of the element antenna almost covers a range of 8-18 GHz.

Also, a lens installing table and an element antenna installing table were made by using Styrofoam, and thus the influence of electromagnetic fields on these tables was minimized.

### 3. Measuring Method

Figure 2 shows a system for measuring gain and antenna patterns. When they were actually measured using this system, as shown in this figure, vertically and horizontally polarized waves were irradiated from a transmitting antenna in an electric dark room and these waves were received through a receiver by means of the standard antenna and the main antenna installed on a rotation table. The results were indicated with a pattern recorder and the absolute gain as found by comparing this receiving level with the known gain of the standard horn. Also, the element antenna was used to receive circularly polarized waves. There is a possibility that a polarization dependence could exist in the element antenna itself. The clamp face of this element antenna was fixed at all times and, as mentioned above, the gain for each respective case was measured and compared with every other. This was done by changing the polarized waves of the transmitting antenna in order to check this particular characteristic.

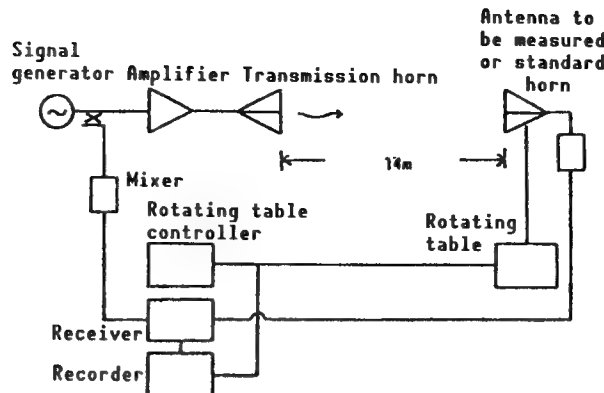


Figure 2. Block Diagram of Measuring System

#### 4. Measurement Results and Discussion

The results of measuring the gain and antenna patterns of the antenna made for this research project are shown below. Also, the following measurement results were obtained by closely attaching the element antenna to the surface of the lens.

##### 4.1 Antenna Patterns

Figure 3(a) to (c) is an example of the results of measuring the antenna patterns of the horizontally polarized waves. These patterns were measured by setting the elevation angle to  $0^\circ$  and by changing the azimuth angle. The transverse and the ordinate denote the azimuth angle and the gain (dBi), respectively, in (a) to (c).

As a result, at 8-18 GHz, the half beam width ranged from  $5\text{--}12^\circ$ . Sharp beams extending over a wide band, as compared with the maximum gain of the main lobe were obtained; that of the first side lobe was restricted to about 17 dB, and wide band properties were confirmed.

As mentioned above, a sharp beam width was obtained at each frequency, but in order to obtain sharper beam widths, it seems to be necessary to theoretically determine the distribution of phases and the amplitude of antenna patterns of the element antenna in reverse form the optimum distribution of electromagnetic fields of the aperture of the lens antenna and to use element antennas possessing such characteristics.

##### 4.2 Gain

Figure 4 shows the results of measuring the gains of horizontally and vertically polarized waves. The transverse and the ordinate denote the frequency (GHz) and the gain (dBi), respectively, in this figure.

As a result, it was ascertained that a gain of 14-24 dBi could be obtained at frequencies of 8-18 GHz. Also, as previously mentioned, it can be expected that if the gain of the element antenna and the distribution phases are

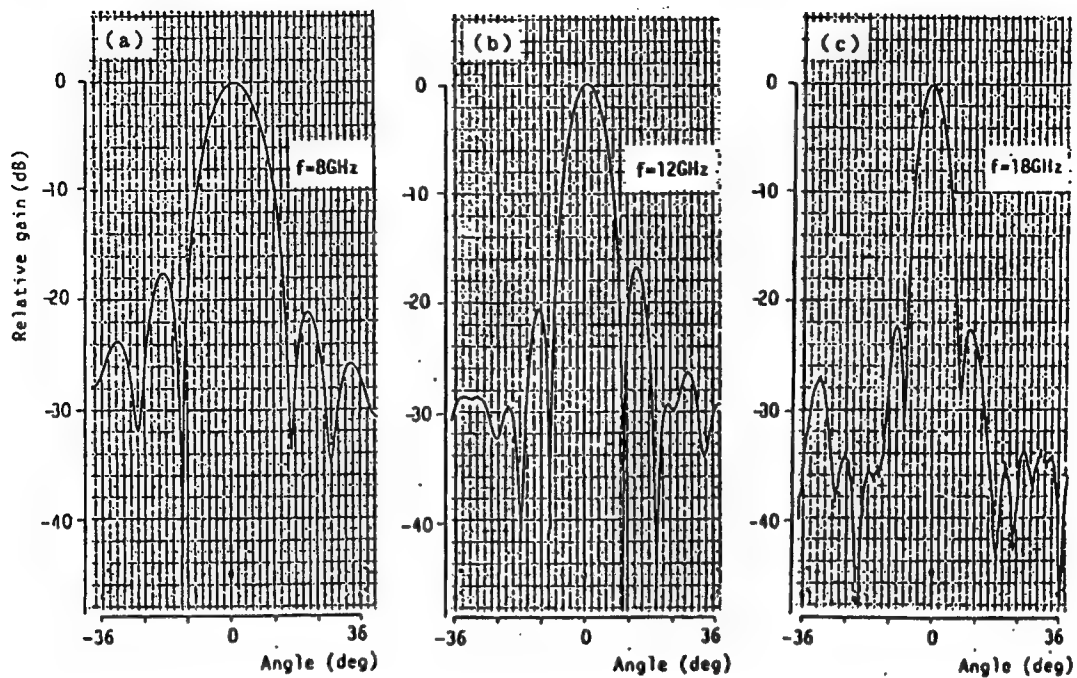


Figure 3. Example of Results of Measuring Antenna Patterns  
(Horizontally polarized waves)

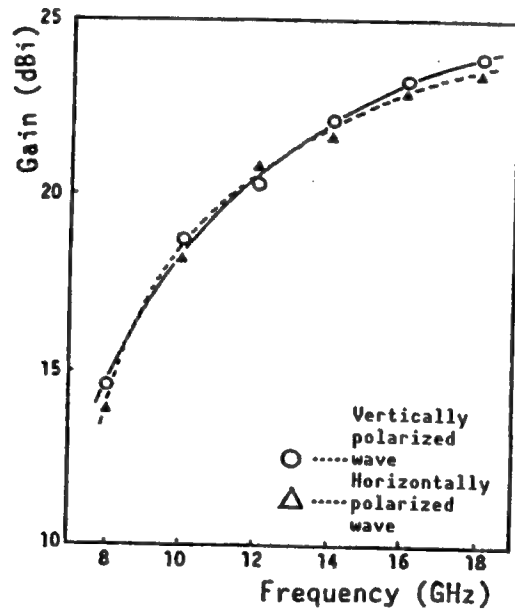


Figure 4. Result of Measuring Gain

optimized by adapting them to the lens by the method described in reference 3, the gain of 14-24 dBi will be further enhanced.

Also, the gain of both horizontally and vertically polarized waves was measured to study the dependence of these waves on gain. As shown in the

figure, a comparison of the results obtained from this measurement indicates that the difference is about 0.5 dB at most and that there is little dependence of the waves on the gain.

### 5. Simulation of Angle Measuring Accuracy

The angle measuring accuracy of this lens antenna was studied as an example of an angle measuring method based on an assumption concerning an amplitude comparison system employing a direct wave detecting system that will be mentioned later on.

In general, when the angle measuring accuracy of a system is evaluated, it is necessary to study receiving systems and various methods of correcting angle measuring errors as well as antenna systems. In this case, the following can be cited as principal error factors that affect angle measuring accuracy:

- (a) Change of characteristics, accompanying temperature change, etc., of the various components that constitute the receiver.
- (b) Fluctuation of gain between a pair of antennas.
- (c) Change of antenna patterns accompanying frequency change.
- (d) Change of antenna patterns accompanying change of polarized waves.

Taking into account these error factors, the following hypotheses were studied as examples of simulations related to angle measuring accuracy when the angle measurements are carried out using this antenna.

- (i) It shall be possible to memorize error correction factors accompanying items (b) and (c) above, which are error factors of the antenna system, for every frequency in advance and to correct these errors during the measurement of angles.
- (ii) As previously mentioned, the angle measuring system shall be an amplitude comparison system employing a direct wave detecting receiver (a block diagram of this system is shown in Appendix A-2).
- (iii) Element antennas shall be arranged on the respective antennas so that these antennas cross each other at a power gain mesial point decreased by three decibels.

As hypothesized in item (i), when considering that errors caused by the antenna system are corrected during the measurement of angles, the error factor to be considered can be limited only to item (a) above. Then, assuming that the rms value of each component error of these receivers is  $\Delta a_i$ , rms value,  $\Delta A$  of the error of all the receivers is given in the following equation:

$$\Delta A = \left\{ \sum_i \Delta a_i^2 \right\}^{1/2} \quad (1)$$

Next, calculating the difference in gain between a pair of antennas, drawing an S curve on the basis of the result of this calculation, and finding the inclination of  $\alpha$  of this curve, the angle measuring error  $\Delta\theta$  is found by using  $\Delta A$  obtained from equation (1) and is expressed as the following equation:

$$\Delta\theta = \Delta A/\alpha \quad (2)$$

First the S curve was determined by measuring the antenna patterns shown in Figure 3 in view of the above theories in order to simulate the angle measuring error. Figure 5 shows an example of the S curve. Finding the inclination  $\alpha$  neighboring  $0^\circ$  from these figures gives Table 1.

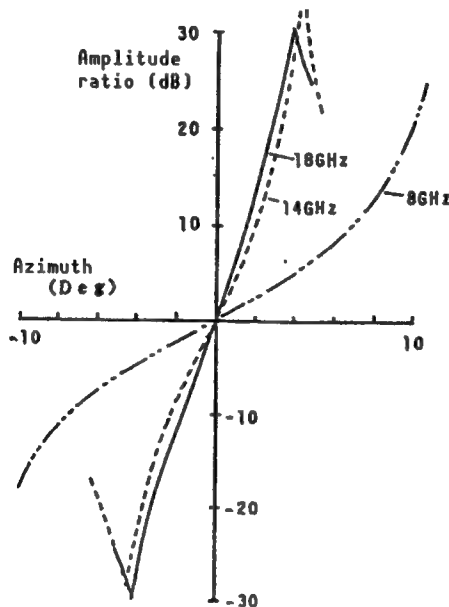


Figure 5. Example of S Curve

Table 1. Inclination of S Curve Determined by Measured Antenna Patterns

Frequency (GHz)	8	14	18
Inclination of S curve (dB/deg)	1.2	4.0	5.8

Also, errors generated by the general wave detector, logarithmic amplifier, etc., are as shown in Table 2 on the basis of references 5, 6, etc.

When the angle measuring error,  $\Delta\theta$ , is calculated by using equations (1) and (2) taking into consideration the above results, the results shown in Table 3 will be obtained.

Table 2. Dispersion of Characteristics of Single Substance Receiver and Between Receivers

Error factor		Standard deviation (dB)
Wave detector	Tracking Linearity	0.7 0.7
Logarithmic amplifier	Tracking Linearity	0.7 0.7
Cables	Tracking	0.35
Total		1.44

Table 3. Result of Calculating Angle Measurement Errors

Frequency (GHz)	8	14	18
Angle measuring error ( $^{\circ}$ rms)	1.2	0.4	0.3

As previously mentioned, the above hypotheses were studied as examples of simulations related to angle measuring accuracy. It is believed that even if one receiving system is changed to another, an angle measuring accuracy close to the values obtained from the simulation can be obtained.

## 6. Conclusion

In this research project, we created a receiving lens antenna that was used to measure two-dimensional angles. This antenna was studied by conducting experiments and simulations to determine the wide band properties and angle measurement properties of this antenna.

As a result of this study, it was confirmed that this antenna had wide band properties with a gain of 14-24 dBi in the X and Ku bands (8-18 GHz). It was further confirmed experimentally that the half beam width of the antenna beams was as sharp as 5 to about  $12^{\circ}$  and that the maximum gain of the first side lobe was about 17 dB lower than that of the main lobe. As a result of conducting experiments and simulations on angle measuring accuracy on the basis of this result, it was ascertained that it is possible to measure angles with a high degree of accuracy (the angle measurement error is  $0.3\text{--}1.2^{\circ}$  rms).

These results would appear to be useful for the manufacture of practical receiving lens antenna to be used to measure two-dimensional angles.

### Appendix A.1 Gain of Element Antenna

Figure A.1 shows the results of measuring gain against the horizontally polarized waves of element antennas used in this research work.

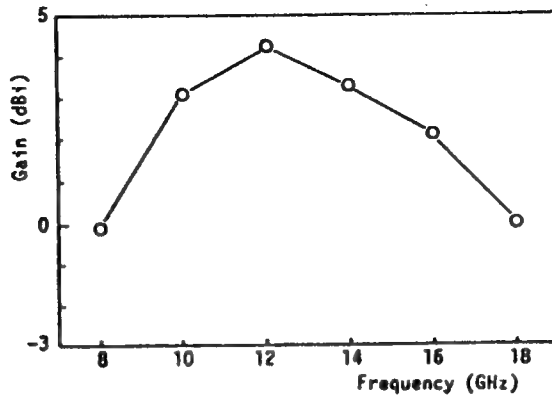


Figure A.1 Results of Measuring Gain of Element Antennas (Horizontally polarized waves)

### Appendix A.2 Receiving System

Figure A.2 shows a block diagram of a direct wave detecting and receiving system hypothesized as a receiving system.

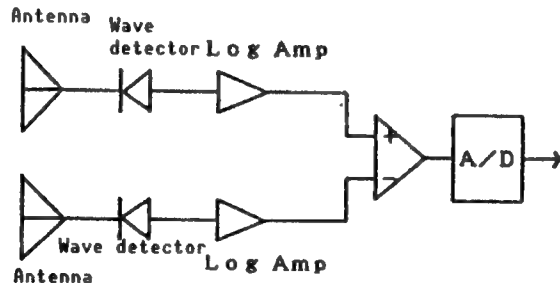


Figure A.2 Block Diagram of Direct Wave Detection and Receiving System

### References

1. Luneberg, R.K., "Mathematical Theory of Optics," Brown University Press, 1944.
2. Tomos, L.A., "The Design of Radially Symmetric Lenses," IEEE TRANS ON AP, Vol AP-18 No 4, July 1970.
3. Hashimoto, "Theoretical Study on Dielectric Sphere Antenna," TRDI TECHNICAL REPORT, No 5467, 1988.

4. Morgan, S.P., "General Solution of the Luneberg Lens," J.A.P., Vol 29 No 9, September 1958.
5. "RHG Electronics Laboratory, Inc., Catalog," 1986, p 29.
6. "Yokogawa-Hewlett-Packard, Ltd., Comprehensive Catalog," 1989, p 680.

## Two-Pulse Technique for New Rocket Motor

906C3824G Tokyo BOEICHO GIJUTSU KENKYUHONBU GIHO (Japan Defense Agency Technical Research & Development Institute) in Japanese Jul 89 Technical Reports, No 5588 pp 1-11

[Article by Kouichi Fukuda and Chikahiro Iwasaki, assistant directors general of the Third Research Laboratory of the Second Prime Mover Department of TDRI's Third Research Center; Tsuneo Miyamoto, captain of the Ground Self-Defense Force of the Second Research Laboratory of the Second Prime Mover Department of TDRI's Third Research Center; and Naminosuke Kubota, assistant director general of the Second Research Laboratory of the Second Prime Mover Department of TRDI's Third Research Center: "Research on Thrust-Control Rocket Motor (I)--Effectiveness of Two-Stage Thrust System and Characteristics of Porous Bulkhead Mechanism"]

### [Text] Summary

Combustion tests were conducted in order to develop an optimized two-stage rocket motor. The pulse motor consisted of two propellant grains, two igniters, and a convergent-divergent nozzle. Both chambers were separated with a disk which was partially opened when the sustainer chamber was operated. Test results indicated that a sustainer pulse was generated at a designated time after a booster pulse operation. The two-pulse technique developed in this study was found to be very useful for practical application.

### 1. Introduction

The interception capabilities of missiles can be expanded by improving the performance of their solid rocket motors. Up to now, efforts to enhance solid rocket motor performance have focused on increasing the specific impulse of propellants and lightening motor cases. However, we have reached the point where it is difficult to increase performance significantly by using only these technologies. Meanwhile, lift-fire technologies for antiaircraft missiles have responded enthusiastically to the challenges posed by the rapid rise in maneuverability, low altitude cruising capability, etc., of aircraft. In order to meet such requirements, it is necessary to raise the overall performance of rocket motors. Accordingly, the thrust-control rocket motor, which improves performance by controlling thrust, can be regarded as a new system to be used in conjunction with other high-performance technologies.<sup>1</sup>

This system is designed so that air resistance proportional to second power of velocity can be reduced by restraining the initial velocity of the missile; lift-fire and terminal velocity can be increased and maneuverability can be ensured<sup>1</sup> by controlling the operation of the rocket motors. In this research work, a small thrust-control rocket motor was trial manufactured, and a destructive bulkhead system, which is a main technology, was established by conducting combustion tests and analyses.

## 2. Outline and Structure of Thrust-Control Rocket Motor

### 2.1 Outline

Japanese defensive missiles are subjected to atmospheric drag at all times during their flight, because they operate in the atmosphere.

The rocket motors used in the present generation of surface-to-air missiles [SAMs] and air-to-air missiles [AAMs] are designed to use the residual velocity when these missiles are used to intercept the enemy by enhancing the initial velocity. However, the use of this method creates severe air resistance proportional to the second power of velocity, and results in large energy losses, because of the relationship between air resistance (D) and flight velocity (V), as shown in the following equation:

$$D = \frac{1}{2} \rho C_D A V^2 \quad (1)$$

Where,

$C_D$  : Coefficient of drag  
 $A$  : Project area of front of missile  
 $\rho$  : Air density

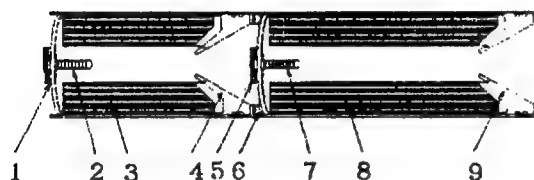
By contrast, when the initial velocity is lowered, it becomes difficult to ensure that sufficient velocity remains to achieve interception. It is believed that thrust can be adequately controlled by using a rocket in which it is possible to control the thrust continuously.<sup>1</sup> Thanks to this control, it will become possible to make missiles fly by restraining their initial velocities and, by lowering the loss of energy during their initial flights, to enable them to fly at their residual velocities during their intermediate flight and to ensure interception velocities by raising the thrust and reaccelerating them during interception. This means that it will become possible to increase lift-fire and terminal velocity, to ensure<sup>1</sup> a high degree of maneuverability, and to expand the missile's interception range.

The liquid-fuel rocket engine can be cited as a rocket in which it is possible to control thrust continuously. This rocket employs a liquid fuel as a propellant and it is possible to control the thrust by controlling the amount of propellant burned in the rocket. In addition, the maximum specific impulse (Isp) is 410 seconds,<sup>2</sup> which is higher than that (about 260 seconds) of solid rocket motors. Prompt firing properties, handling properties, and ease of storage are indispensable elements for tactical missiles. Liquid-fueled

rockets present problems in this regard, because the rocket has a complex structure<sup>2</sup> and it is difficult to handle the liquid fuel. By contrast, solid-fuel rockets excel in this respect, and are used in most of the missiles currently in the inventories of the advanced Western countries. At present, solid-fuel missiles are gradually replacing liquid-fueled ones.

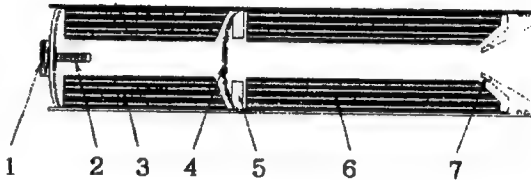
The disadvantage of the solid-fuel missile is that it is difficult to variably control the thrust, because it is impossible to shut off the solid rocket motor during the combustion of the solid propellant or to control the combustion rate of the solid propellant.<sup>3</sup> However, use of the following systems may make it possible to achieve thrust-control rocket motors suitable for defensive tactics, because these systems control thrust by dividing the propellant.

When solid rocket motors are used in missiles, it should be possible to control the thrust by dividing the propellant into some number of parts, controlling the respective ignition times, intermittently controlling the operation and optimizing the timing of the operation. The multistage (two-stage) rocket shown in Figure 1(a) and the multistage (two-stage) thrust rocket shown in Figure 1(b) can be regarded as examples of such systems. Independent rocket motors are connected in series in the multistage rocket, and the inside of the rocket motor is divided into several combustion chambers in the multistage thrust rocket.



- 1 Second stage S&A device
- 2 Second stage igniter
- 3 Second stage propellant
- 4 Second stage nozzle
- 5 Separator
- 6 First stage S&A device
- 7 First stage igniter
- 8 First stage propellant
- 9 First stage nozzle

Figure 1(a). Two-Stage Rocket



- 1 Second stage S&A device
- 2 Second stage igniter
- 3 Second stage propellant
- 4 Bulkhead
- 5 First stage igniter
- 6 First stage propellant
- 7 Nozzle

Figure 1(b). Two-Stage Thrust Rocket

The use of the former system will improve propulsion efficiency, because unnecessary mass is jettisoned by the orderly separation of spent rockets from the missile.<sup>4</sup> Further, it is possible to enhance propulsion efficiency by optimizing the nozzle shape corresponding to the pressure of each combustion chamber, because a special-purpose nozzle is installed on each rocket motor. However, this system is inappropriate for tactical missiles, for the following two reasons: 1) the possibility that the rockets separated from the missile will fall to the ground, and 2) a number of nozzles with large capacities are

installed in the rocket motors, while the amount of propellant is sharply limited because the outside dimensions of these missiles are severely restricted. Therefore, this system is adopted for space rockets whose launch sites are determined in advance and whose capacities can be ensured.

The latter system has no separating section and the structure of this system is simplified. The system is designed so that a number of combustion chambers use a common nozzle, and the combustion gas generated in the combustion chambers at the rear stage passes through the inside of the spent combustion chambers. It is also possible to prevent a decrease in the rate of propellant charged for the capacity of the rockets. A large amount of combustion gas is generated at high temperatures in the combustion chamber operated previously. When the intervals between the respective combustion chambers are considered, it is necessary to isolate them from each other so that the heat, pressure, and flames caused by the combustion gas passing through them do not ignite unburned propellant stored in unoperated combustion chambers. In addition, when the combustion chambers at the rear stage are operated, the system must be structured so that the combustion chambers at the nozzle side will no longer be isolated. Accordingly, it is necessary to solve a number of technical problems related to the isolation structure of the bulkhead, etc., which will satisfy these conditions. However, when this system is compared to the former system, the latter system is more suitable as a rocket motor for tactical missiles than the former.

For these reasons, thrust control is considered in this research work in terms of a system in which the inside of a solid rocket motor is divided into several combustion chambers.

## 2.2 Comparison With Current Rocket Motors

Figure 2 shows a comparison between typical rocket motors used in operational missiles and thrust-control rocket motors with regard to structures and thrust patterns.

Figure 2(a) shows the structure and thrust curve of the rocket motor used in operational missiles. The rocket motor consists of a nozzle and a double rear-shaped propellant formed by overlapping two kinds of propellants. The relation between thrust and time is that a large thrust is obtained from the combustion of the booster propellant on the inside while a lesser thrust is generated from the combustion of sustainer propellant on the outside.

Figure 2(b) shows the case of a thrust-control rocket motor. This rocket motor, which has a two-stage thrust structure, consists of a nozzle and two combustion chambers. Different propellants can be loaded in the respective combustion chambers. The two combustion chambers and the propellant are separated from each other with a bulkhead that shuts out the heat, flames, and pressure of the combustion gas. The rocket motor operating system is designed so that after the first stage propellant is burned and the arbitrarily set time passes, the second stage propellant will ignite and, simultaneously, second stage thrust will be generated by breaking the pressure bulkhead.

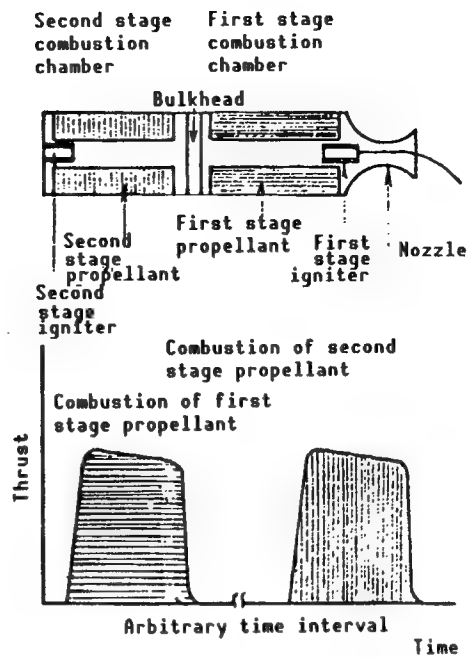
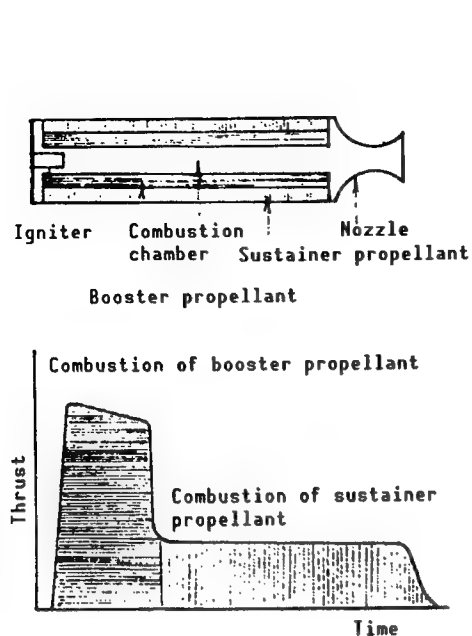


Figure 2(a). Thrust Curve and Structure of Operational Rocket Motor

Figure 2(b). Thrust Curve and Structure of Thrust Control Rocket Motor

Therefore, the thrust generated from this rocket motor is characterized by the fact that this thrust has two kinds of thrust depending on time, and the time interval between the first and second stages can be determined arbitrarily.

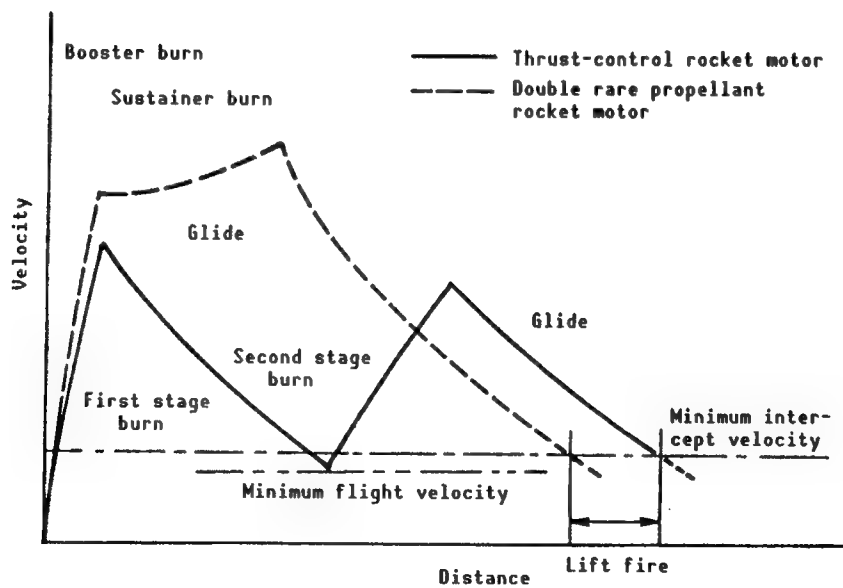


Figure 3. Flight Performance Using Thrust-Control Rocket Motor

Figure 3 shows the relationship between flight velocity and distance for SAMs when operational rocket motors and thrust-control rocket motors are used in SAMs, respectively. When the operational rocket motor is used in a SAM, the flight velocity will reach its peak at the time when the propellants of both the booster and sustainer are burned completely, and, subsequently, the SAM will glide freely until it hits the target. The high maximum velocity means that, as shown in equation (1), a large amount of kinetic energy is lost because the air resistance imposed on the rocket motor operating system is proportional to the square of the velocity. By contrast, when a SAM is launched, a thrust-control rocket motor will burn only the first stage propellant, and thereby restrain its initial maximum velocity. Subsequently, this rocket motor will interrupt its operation by itself and the SAM will glide freely. In addition, when the velocity of the SAM reaches minimum flight velocity, the rocket motor will ignite the second stage propellant and will again enhance flight velocity. After combustion of the second stage propellant is completed, the SAM will glide freely until it hits the target. As mentioned above, air resistance can be reduced by restraining the maximum velocity, and lift fire, as shown in Figure 3, can be effected qualitatively by minimizing energy loss. Also, when a SAM approaches its target, and when its residual velocity is comparatively high, the ignition of the second stage rocket motor can be initiated arbitrarily, and it will thus be possible to increase the intercept velocity of the SAM by reaccelerating it at an early period and to ensure its maneuverability.

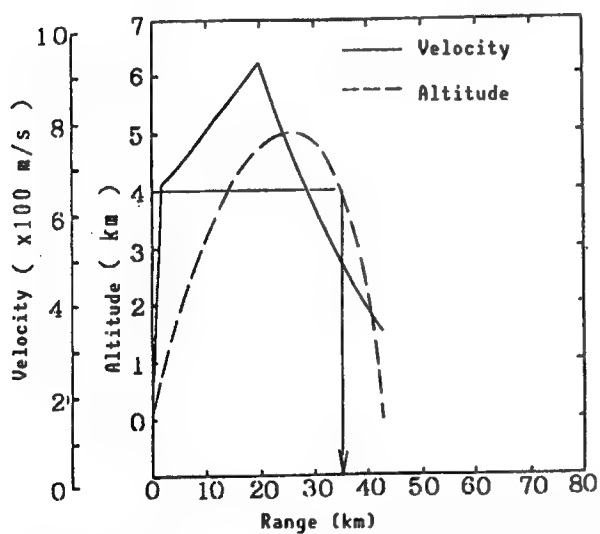


Figure 4(a). Flight Curve of Double Rare Propellant Rocket Motor

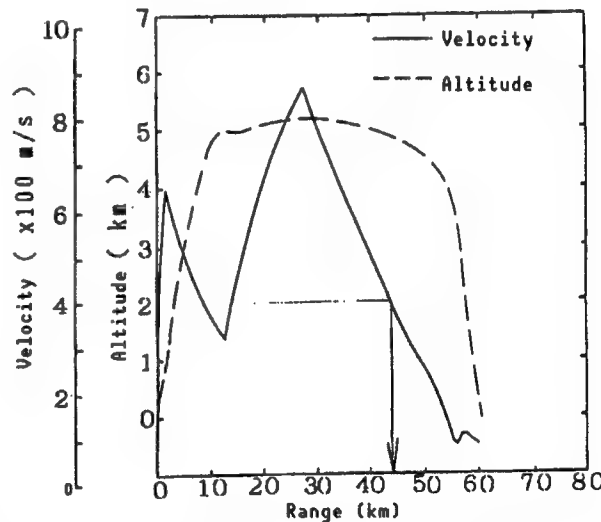
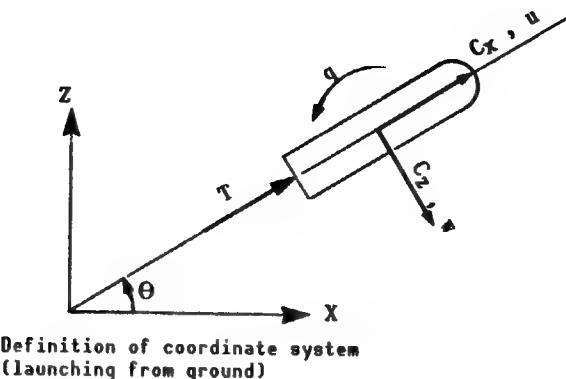


Figure 4(b). Flight Curve of Two-Stage Thrust-Control Rocket Motor

Figure 4 shows the results obtained from theoretical calculations of the relationship between the ballistic flying range and altitude of a SAM. (Figure 4(c) schematically depicts the results obtained from simulation calculations.) When a rocket motor (conventional dual thrust motor) employing a double rare propellant is used in a missile on the assumption that the interception parameters are at an altitude of 4,000 or more and the velocity



$$\dot{u} = -qw + \frac{Q \cdot S}{m} C_x - g \cdot \sin \theta + \frac{T}{m}$$

$$\dot{v} = qu + \frac{Q \cdot S}{m} C_z + g \cdot \cos \theta$$

$$\dot{\theta} = q$$

$$\dot{x} = u \cos \theta + v \sin \theta$$

$$\dot{z} = u \sin \theta - v \cos \theta$$

Where,

u, w: Velocity (body axis)

q: Pitch rate (horizontal flying transfer 90°/s)

$C_x, C_z$ : Aerodynamic coefficient (application of aerodynamic characteristics of usual SAM, for example,  $C_{x0} = 0.6$  at  $M = 2$ )

Q: Dynamic pressure

S: Standard area ( $0.071 \text{ m}^2$ )

m: Mass (initial period, 525 kg/g; propellant, 225 kg/g)

T: Thrust ( $5,000 \text{ kgf} \times 6 \text{ s} \sim \text{interruption } 15 \text{ s} \sim 5,000 \text{ kgf} \times 5 \text{ s}$ )

θ: Airframe attitude angle

X, Z: Inertial coordinate system

g: Gravitational acceleration

Figure 4(c). Basic Equation of Flight Simulation  
and Example of Input Data

is 400 or more per second, as shown in Figure 4(a), the maximum range will be about 35 km. When a thrust-control rocket motor is used instead of a dual thrust motor in this missile, and when the gliding flight of the missile is calculated, as shown in Figure 4(b), the maximum range will be about 43 km. In this case, the dimensions and amount of propellant for this thrust-control rocket motor must be equivalent to those of the former rocket motor. This

fact indicates that it is possible to increase the lift fire by about 25 percent.

As mentioned above, it is possible to raise the overall performance, including lift fire and intercept capability, of missiles by using thrust-control rocket motors in these missiles.

### 2.3 Structure and Operating System

Figure 5 shows the structure of a two-stage thrust-control rocket motor that consists primarily of two combustion chambers for thrust control, a bulkhead to serve as a boundary between the two combustion chambers, a nozzle, and a rocket operating igniter. It is possible to load different propellants in the respective combustion chambers.

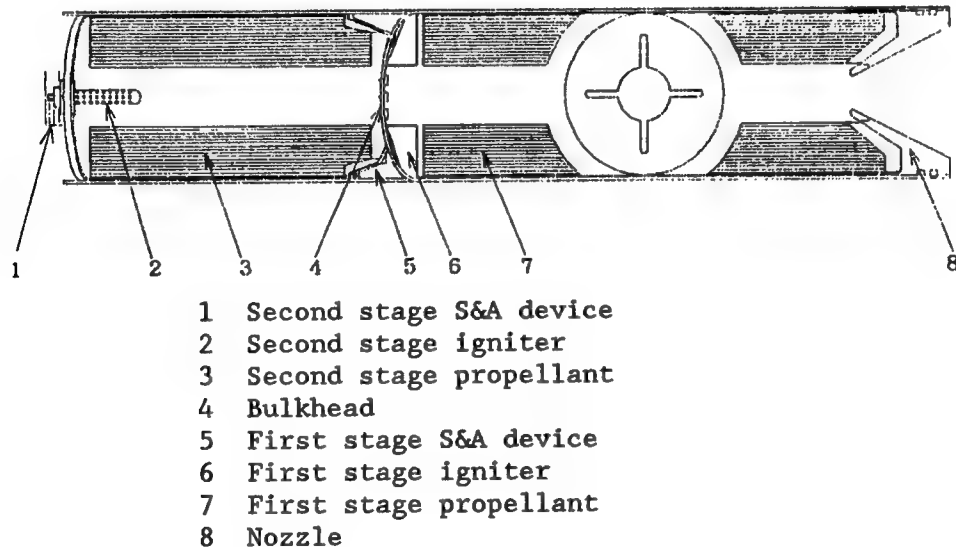


Figure 5. Structural Drawing of Two-Stage Thrust-Control Rocket Motor

The bulkhead must be structured so that heat, pressure, and flames are isolated from each other and so that the second stage propellant is not ignored by the high-temperature gas generated in the first stage combustion chambers during the operation of this combustion chamber. It must also be structured so that it can be broken readily by second stage combustion and so that the nozzle will not become clogged with the fragments created when it breaks.

It is necessary to consider lightening the safety and arming [S&A] mechanism, which consists of an igniter and a safety device, and the position for installing this mechanism, because the igniter and the safety device have independent combustion chambers join the S&A mechanism. In particular, the igniter for the first stage combustion chamber may be regarded as a burning-type igniter after the work is finished so that it will not cause any serious trouble, such as clogging of the nozzle, etc., during the operation of the second stage combustion chamber.

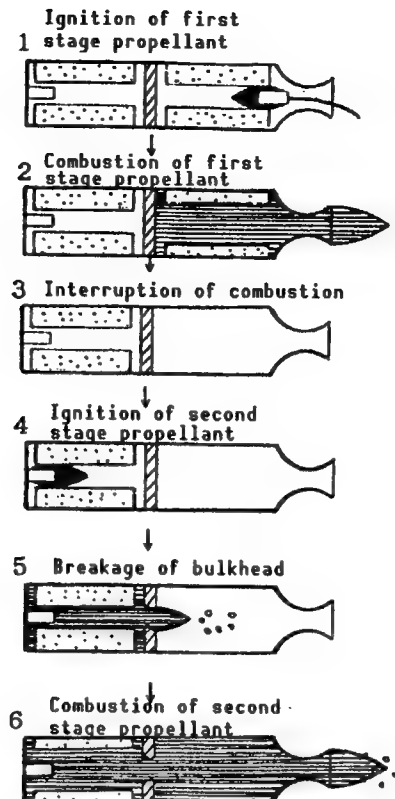


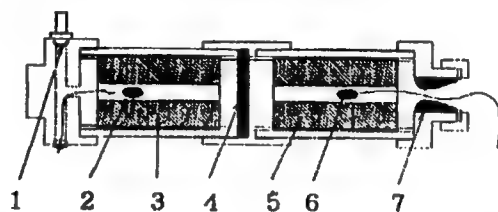
Figure 6. Operating System of Thrust-Control Rocket Motor

As shown in Figure 6, the second stage operating system of the thrust-control rocket motor conforms to the following procedure:

- (1) The first stage propellant igniter fires.
- (2) Initial thrust is generated by burning the first stage propellant. At this time, the bulkhead shuts out combustion gas and heat from the other chamber.
- (3) Next, operation of the rocket motor is stopped for an arbitrary time lasting from a few seconds to 10 seconds or more.
- (4) The second stage propellant igniter is operated in accordance with instructions given from the ground or from the missile itself.
- (5) The second stage propellant is burned. The bulkhead is broken by the combustion chamber pressure generated at this time.
- (6) Secondary thrust is generated.

### 3. Method of Experiment and Device

The thrust-control rocket motor involves three technical problems: a bulkhead breaking system, pressure resistance, and heat resistance of the bulkhead, and lightening the bulkhead. The bulkhead structure and function, which are the most important technologies, were studied in this research work. A porous system, a 90° opening and rotating door system, a slide opening system, a heat insulating material peeling system, etc., were studied in a pre-experiment. We have come to the conclusion that current design methods and materials are insufficient, except for the porous system, in terms of reliability of operation, simplicity and weight. As a result, we have determined to adopt the porous system. We have made a bulkhead testpiece suitable in size for an experimental scale, have incorporated this bulkhead testpiece in a wall thickness-type small-sized rocket motor with a diameter of 80 mm, and have conducted an experiment on the combustion of this rocket motor. Figure 7 shows a structural drawing of the rocket motor used in this experiment.



- 1 Pickup for measurement of second stage pressure
- 2 Second stage igniter
- 3 Second stage propellant
- 4 Bulkhead
- 5 First stage propellant
- 6 First stage igniter
- 7 pressure leading hole for measurement of the first stage pressure
- 8 Nozzle

Figure 7. Experimental Device

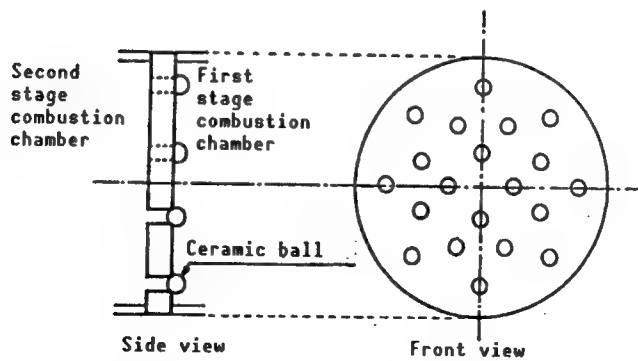


Figure 8. Structural Drawing of Experimental Bulkhead

Figure 8 shows a structural drawing of the bulkhead used in the experiment. This bulkhead is a stainless disk with a diameter of 80 mm. Twenty holes with a diameter of 4.5 mm are made in the bulkhead; the total area of the holes is 2.8 times that of the nozzle straw area. Therefore the speed when these holes in the bulkhead are open and the combustion gas passes through them will be low-subsonic, about Mach 0.2, and will not result in any pressure loss that would lower the performance of the rocket motor. Ceramic balls with a diameter of 6 mm were fastened to the first stage combustion chamber side of these holes in order to prevent the heat and combustion gas generated during first stage combustion from penetrating the second chamber. This diameter is about half that of the nozzle. These ceramic balls are designed so that when the second stage propellant is ignited, the gas pressure will separate them from the bulkhead and they will be discharged to the outside of the nozzle through the first stage combustion chamber, which is already empty.

Figure 9 [not reproduced] is a photograph of the bulkhead used in this experiment. It was taken from the side of the first stage combustion chamber. The white sections are the ceramic balls affixed to the first stage combustion chamber side. A mixture of epoxy resin and titanium oxide was applied as a heat resistant material around the ceramic balls in order to raise the heat resistance of the bulkhead.

Table 1 and Figure 10 show the composition and shape of the propellant used in the experiment, respectively. The internal both-end-face combustion system was adopted as the propellant combustion system to keep combustion chamber pressure as constant as possible. The theoretical flame temperature was 2,900 K.

Table 1. Composition of Sample Propellant

Kind of propellant		R-1
Component	Particle diameter ( $\mu\text{m}$ )	(Percent)
AP	200	43
	20	43
HTPB	—	14

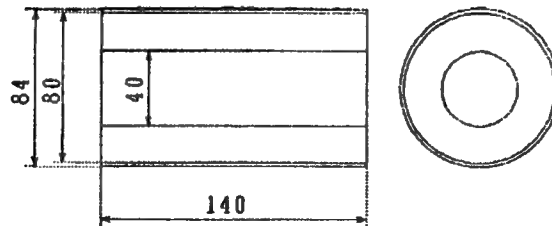


Figure 10. Shape of Sample Propellant

Carbon graphite was used as the nozzle material. The nozzle throat diameter ( $D_t$ ) was 13.58 mm and the opening ratio ( $\epsilon$ ) was 2.0.

An igniter installed in a hole in the propellant was used to activate the rocket motor. An ignition code for the first stage combustion chamber and another for the second stage combustion chamber were passed from the nozzle and the forward cap, respectively. The HTPB/AP composite propellant was cut into 5 mm cubes and these small cubes were mixed with 6 g of black powder. This mixture was used as a powder for the igniter.

The measurement variable was determined to be the pressure in each combustion chamber. The first stage and the second stage combustion chamber pressures were measured with a strain gauge pressure pickup via a pressure leading hole in the nozzle cap and a forward cap, respectively.

#### 4. Results and Discussion

Figure 11 shows the relationship between combustion time and combustion chamber pressure obtained from the experiment.

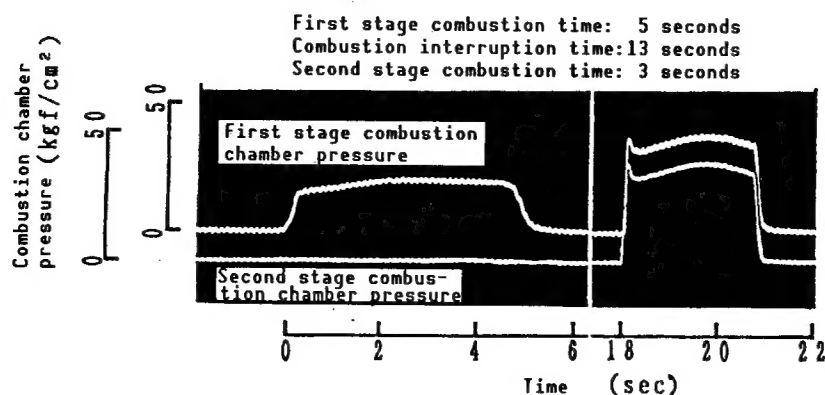


Figure 11. Relationship Between Combustion Pressure and Time

First, the first stage igniter was activated to burn the first stage propellant. This propellant was burned for 5 seconds at  $20 \text{ kgf/cm}^2$  without any ignition delay.

It can be determined that the ceramic balls adhered to the bulkhead effectively, i.e., they completely shut off the first stage combustion gas and heat. This can be verified by the fact that the pressure in the second stage combustion chamber did not increase during the 5-second burn.

After the second stage combustion was completed, and after 13 seconds passed, the second stage igniter was activated. As soon as the second stage propellant was ignited, the ceramic balls were separated from the bulkhead by the combustion gas pressure and were discharged from the nozzle via the flow of combustion gas. There was a possibility of combustion chamber pressure being generated from the discharge of the ceramic balls, but no rise or peak of harmful pressure like the combustion chamber pressure was detected.

The second stage propellant was burned for 3 seconds at  $40 \text{ kgf/cm}^2$  without any ignition delay. There was no difference between the pressure of the first

stage combustion chamber and that of the second. Therefore, it can be concluded that the combustion gas flowed from the second stage combustion chamber to the first without any pressure loss caused by the bulkhead. This experiment indicates that there was no interference (influence by heat transfer, etc.) of the first stage combustion chamber pressure to the second during the interruption of combustion for at least 13 seconds, and that the combustion interruption time can be selected arbitrarily for an interval of 13 seconds or less.

After the operation of the rocket motor was completed, it was disassembled for operation. Figure 12 [not reproduced] shows the condition of the bulkhead. All the ceramic balls were separated from the bulkhead, the degree of burn damage to the bulkhead was very low, and the holes on the second stage combustion chamber side were burned and slightly damaged. There were no ceramic balls in the combustion chamber; all the ceramic balls were discharged through the nozzle to the outside. Also, neither breakage nor damage was seen on the nozzle. Therefore, it can be concluded that all the ceramic balls passed smoothly through the nozzle.

Based on the above, it can be said that the rocket motor used in this experiment achieved thrust control without lowering combustion performance.

## 5. Conclusion

- (1) The bulkhead breaking system used in this research study had no influence on the combustion pressure and temperature in the second stage combustion chamber during first stage combustion. There was no damage to the nozzle, etc., due to fragments from the bulkhead, nor was there any decrease in the performance of the rocket motor.
- (2) No pressure loss was seen at the bulkhead through which the combustion gas of the second stage propellant passed.
- (3) Stable combustion was achieved by a thrust-control rocket motor using a bulkhead based on this bulkhead breaking system. Also, we were able to control the operation of this rocket motor for a specified time interval (about 10 seconds, virtually the assumed time).

## 6. Future Research Subjects

In the future, it will be necessary to carry out research in the following areas by using an actual missile: 1) lightening the bulkhead; 2) testing and evaluating heat resistance; and 3) the ignition system for each stage.

### References

1. Carrir, J.L.C., et al., "The Dual-Interrupted-Thrust Pulse Motor," AIAA-86-1576, 1986.
2. Kubota, N., "Rocket Engine Engineering (5)," INTERNAL COMBUSTION ENGINE, Vol 21 No 271, November 1982.
3. Endoh, K., et al., "Rocket Engineering," NIKKAN KOGYO SHIMBUN, 1960, p 135.
4. Sanuki, M., "Rocket Engineering," Corona Publishing Co., 1970, p 161.

- END -

10  
22161

45

NTIS  
ATTN: PROCESS 103  
5285 PORT ROYAL RD  
SPRINGFIELD, VA

22161

This is a U.S. Government publication. Its contents in no way represent the policies, views, or attitudes of the U.S. Government. Users of this publication may cite FBIS or JPRS provided they do so in a manner clearly identifying them as the secondary source.

Foreign Broadcast Information Service (FBIS) and Joint Publications Research Service (JPRS) publications contain political, economic, military, and sociological news, commentary, and other information, as well as scientific and technical data and reports. All information has been obtained from foreign radio and television broadcasts, news agency transmissions, newspapers, books, and periodicals. Items generally are processed from the first or best available source; it should not be inferred that they have been disseminated only in the medium, in the language, or to the area indicated. Items from foreign language sources are translated; those from English-language sources are transcribed, with personal and place names rendered in accordance with FBIS transliteration style.

Headlines, editorial reports, and material enclosed in brackets [] are supplied by FBIS/JPRS. Processing indicators such as [Text] or [Excerpts] in the first line of each item indicate how the information was processed from the original. Unfamiliar names rendered phonetically are enclosed in parentheses. Words or names preceded by a question mark and enclosed in parentheses were not clear from the original source but have been supplied as appropriate to the context. Other unattributed parenthetical notes within the body of an item originate with the source. Times within items are as given by the source. Passages in boldface or italics are as published.

#### SUBSCRIPTION/PROCUREMENT INFORMATION

The FBIS DAILY REPORT contains current news and information and is published Monday through Friday in eight volumes: China, East Europe, Soviet Union, East Asia, Near East & South Asia, Sub-Saharan Africa, Latin America, and West Europe. Supplements to the DAILY REPORTs may also be available periodically and will be distributed to regular DAILY REPORT subscribers. JPRS publications, which include approximately 50 regional, worldwide, and topical reports, generally contain less time-sensitive information and are published periodically.

Current DAILY REPORTs and JPRS publications are listed in *Government Reports Announcements* issued semimonthly by the National Technical Information Service (NTIS), 5285 Port Royal Road, Springfield, Virginia 22161 and the *Monthly Catalog of U.S. Government Publications* issued by the Superintendent of Documents, U.S. Government Printing Office, Washington, D.C. 20402.

The public may subscribe to either hardcover or microfiche versions of the DAILY REPORTs and JPRS publications through NTIS at the above address or by calling (703) 487-4630. Subscription rates will be

provided by NTIS upon request. Subscriptions are available outside the United States from NTIS or appointed foreign dealers. New subscribers should expect a 30-day delay in receipt of the first issue.

U.S. Government offices may obtain subscriptions to the DAILY REPORTs or JPRS publications (hardcover or microfiche) at no charge through their sponsoring organizations. For additional information or assistance, call FBIS, (202) 338-6735, or write to P.O. Box 2604, Washington, D.C. 20013. Department of Defense consumers are required to submit requests through appropriate command validation channels to DIA, RTS-2C, Washington, D.C. 20301. (Telephone: (202) 373-3771, Autovon: 243-3771.)

Back issues or single copies of the DAILY REPORTs and JPRS publications are not available. Both the DAILY REPORTs and the JPRS publications are on file for public reference at the Library of Congress and at many Federal Depository Libraries. Reference copies may also be seen at many public and university libraries throughout the United States.